University of Alberta

Numerical Investigation of the Thermal Interaction between a Shape Memory Alloy and Low Reynolds Number Viscous Flow

by

Christopher Thomas Reaume

©

A thesis submitted to the Faculty of Graduate Studies and Research in partial fulfillment of the requirements for the degree of Master of Science.

Department of Mechanical Engineering

Edmonton, Alberta
Spring 2000

National Library of Canada
Acquisitions and Bibliographic Services
395 Wellington Street
Ottawa ON K1A 0N4
Canada

Bibliothèque nationale du Canada
Acquisitions et services bibliographiques
395, rue Wellington
Ottawa ON K1A 0N4
Canada

Your file Votre référence

Our file Notre référence

The author has granted a non-exclusive licence allowing the National Library of Canada to reproduce, loan, distribute or sell copies of this thesis in microform, paper or electronic formats.

L'auteur a accordé une licence non exclusive permettant à la Bibliothèque nationale du Canada de reproduire, prêter, distribuer ou vendre des copies de cette thèse sous la forme de microfiche/film, de reproduction sur papier ou sur format électronique.

The author retains ownership of the copyright in this thesis. Neither the thesis nor substantial extracts from it may be printed or otherwise reproduced without the author's permission.

L'auteur conserve la propriété du droit d'auteur qui protège cette thèse. Ni la thèse ni des extraits substantiels de celle-ci ne doivent être imprimés ou autrement reproduits sans son autorisation.

0-612-60170-6

Canada

University of Alberta

Library Release Form

Name of Author: Christopher Thomas Reaume

Title of Thesis: Numerical Investigation of the Thermal Interaction between a Shape Memory Alloy and Low Reynolds Number Viscous Flow

Degree: Master of Science

Year this Degree Granted: 2000

Permission is hereby granted to the University of Alberta to reproduce single copies of this thesis and to lend or sell such copies for private, scholarly, or scientific research purposes only.

The author reserves all other publication and other rights in association with the copyright in the thesis, and except as hereinbefore provided, neither the thesis nor any substantial portion therof may be printed or otherwise reproduced in any material form whatever without the author's prior written permission.

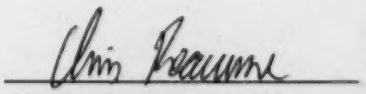

Christopher Thomas Reaume
#1 10725 85 Avenue,
Edmonton,AB
Canada, T6E 2K9

University of Alberta

Faculty of Graduate Studies and Research

The undersigned certify that they have read, and recommend to the Faculty of Graduate Studies and Research for acceptance, a thesis entitled Numerical Investigation of the Thermal Interaction between a Shape Memory Alloy and Low Reynolds Number Viscous Flow submitted by Christopher Thomas Reaume in partial fulfillment of the requirements for the degree of Master of Science.

J. W. Yokota

Dr. Yokota (Supervisor)

Dr. Mees

A. Bhattacharyya

Dr. Bhattacharyya

Date Dec. 6, 1999

Abstract

A numerical scheme for the two dimensional modelling of the thermal interaction between a smart material and low Reynolds number cross flow has been developed. The phase change of the smart material is modeled by the temperature dependence of the thermal conductivity and heat capacity of the solid. The change in these properties with temperature is shown to have a substantial effect on the temperature history of the solid.

The thermal boundary between the fluid and solid is represented with a heat flux conserving boundary condition. This boundary condition represents the temperature dependent physics of the heat transfer at the surface.

Results from the two dimensional scheme were compared to a one dimensional analysis of the average smart material temperature. This comparison indicated that the one dimensional analysis is a poor indicator of the two dimensional results. This is due to the assumption in the one dimensional analysis of constant heat flux with time.

To my parents, for always being there.

ACKNOWLEDGEMENTS

First and foremost sincere thanks are extended to my supervisor, Dr.Jeff Yokota. This work would not have been possible without his guidance and mentorship.

Thanks are also extended to Dr.Bhattacharyya for lending his expertise in the area of shape memory alloys.

Special thanks to everybody in the CFDAM lab. In addition, thanks to everyone from the lunch crew, anybody whoever tossed the frisbee around, went to the Plant for a few or just generally made the time more enjoyable.

I am also grateful to the Natural Sciences and Engineering Research Council of Canada for financial support of this research.

Contents

1 Introduction **1**
- 1.1 Shape Memory Alloys 1
- 1.2 Present State of Field 3
- 1.3 Convective Heat Transfer 4

2 Problem Description **7**
- 2.1 Selected Application 7
- 2.2 Simon Nitinol Filter® 8
- 2.3 Insertion of Inferior Vena Cava Filter 9
- 2.4 Computational Domain 10

3 Governing Equations **15**
- 3.1 General Form of Equations 15
- 3.2 Modification of Equations 16
  - 3.2.1 Boussinesq Approximation 16
  - 3.2.2 Application of Assumptions to Governing Equations . . 18
  - 3.2.3 Governing Equations in Fluid Region 21
- 3.3 Modeling of Shape Memory Alloy Properties 25
  - 3.3.1 Property Model 25
  - 3.3.2 Mathematical Representation of Phase 28
  - 3.3.3 Functional Fit to Phase Equation 31
  - 3.3.4 Numerical Modeling of Thermal Conductivity 35
  - 3.3.5 Latent Energy of Transformation 38
  - 3.3.6 Governing Equations in Solid Region 41
- 3.4 Flow Decomposition 41
- 3.5 Coordinate Transformation 42
- 3.6 Dimensional Analysis 45

4 Numerical Formulation **49**
4.1 Solution Sequence 49
4.2 Convergence of Viscous Stream Function 52
4.2.1 Approximate LU Factorization 52
4.2.2 Multigrid Convergence Acceleration 54
4.3 Model Equation 56
4.4 Time Integration of Equations in Fluid Region 57
4.5 Spatial Integration Scheme 58
4.6 Interpolation of Convection Term 60
4.7 Time Integration of Energy Equation in Solid 62
4.8 Newton Iteration Solution of Energy Equation 64
4.9 Numerical Stability 66
4.9.1 Single Step Semi-Implicit Time Advancing 67
4.9.2 Multistage Convergence Iteration 70
4.10 Boundary Conditions 73
4.10.1 Fluid Field Boundary Conditions 73
4.10.2 Thermal Interaction Boundary Condition 76

5 Results **80**
5.1 Values of Dimensionless Groups 80
5.1.1 Freestream Fluid Velocity 81
5.2 Numerical Domain 82
5.3 Development of Flow Field Periodic Solution 86
5.4 Constant Material Properties in Solid Region 93
5.4.1 Results from Two Dimensional Simulation 93
5.4.2 Comparison to One Dimensional Analysis 96
5.5 Comparison between Smart Material and Constant Property Material 100
5.5.1 Results from Two Dimensional Simulation 100
5.5.2 Comparison to One Dimensional Analysis 106
5.6 Comparison of Smart Materials with Different Material Properties 110

6 Conclusions **126**

List of Figures

2.1	Simon Nitinol Inferior Vena Cava Filter	8
2.2	Inferior Vena Cava Viewed Along Axis	12
2.3	Mapping of Curved Plane onto Flat Space	13
2.4	Domain of Problem	13
3.1	Displacive Phase Transformation between Austenite and Martensite	26
3.2	Comparison of Approximate Function to Numerical Integration	34
3.3	Thermal Conductivity for Both Material Phases	37
3.4	Specific Internal Energy for Both Material Phases	40
3.5	Transformation from (x, y) to (ξ, η) Coordinate System	43
4.1	Schematic of Six Level 'W' Cycle used in Multigrid Scheme	56
4.2	Error Amplification Factor for Multistage Solution of Conduction Equation	72
4.3	Diagram of Fluid and Smart Material Boundary	76
4.4	Boundary Cell	77
5.1	Supplied Grid in Fluid Portion of the Domain	84
5.2	Developed Grid in Solid Portion of the Domain	85
5.3(a)	Vorticity Contours in Fluid Region, t = 0.004	87
5.3(b)	Vorticity Contours in Fluid Region, t = 0.008	88
5.3(c)	Vorticity Contours in Fluid Region, t = 0.012	89
5.3(d)	Vorticity Contours in Fluid Region, t = 0.016	90
5.3(e)	Vorticity Contours in Fluid Region, t = 0.020	91
5.4	Average Vorticity History for Isothermal Simulation	92
5.5	Average Temperature History for Material with Constant Properties	94

5.6 Average Surface Heat Transfer Coefficient History for Constant Property Material 95
5.7 Comparison Between 1D and 2D Temperature Histories . . 98
5.8 Time History of Biot Number for Constant Property Material 99
5.9 Average Temperature History for Smart Material and Constant Property Material 102
5.10 Average Internal Energy History for Smart Material and Constant Property Material 103
5.11 Average Surface Heat Transfer Coefficient for Smart Material 104
5.12 Cycle Averaged Surface Heat Transfer Coefficients 105
5.13 Comparison Between 1D and 2D Temperature History, Smart Material 107
5.14 Comparison Between 1D and 2D Phase History 108
5.15 Time History of Biot Number for Smart Material 109
5.16 Phase History for Smart Materials with Different Transition Temperatures 113
5.17 Phase History for Smart Materials with Different Latent Transformation Energy Amounts 114
5.18 Temperature History for Smart Materials with Different Latent Transformation Energy Amounts 115
5.19(a) Phase Contours in Smart Material 'A' for one Period of Vortex Shedding, t = 0.800 116
5.19(b) Phase Contours in Smart Material 'A' for one Period of Vortex Shedding, t = 0.804 117
5.19(c) Phase Contours in Smart Material 'A' for one Period of Vortex Shedding, t = 0.808 118
5.19(d) Phase Contours in Smart Material 'A' for one Period of Vortex Shedding, t = 0.812 119
5.19(e) Phase Contours in Smart Material 'A' for one Period of Vortex Shedding, t = 0.816 120
5.20(a) Phase Contours in Smart Material 'B' for one Period of Vortex Shedding, t = 0.020 121
5.20(b) Phase Contours in Smart Material 'B' for one Period of Vortex Shedding, t = 0.024 122
5.20(c) Phase Contours in Smart Material 'B' for one Period of Vortex Shedding, t = 0.028 123
5.20(d) Phase Contours in Smart Material 'B' for one Period of Vortex Shedding, t = 0.032 124

5.20(e) Phase Contours in Smart Material 'B' for one Period of Vortex Shedding, t = 0.036 125

List of Tables

5.1 Fluid Material Properties 80
5.2 Solid Material Properties 81
5.3 Dimensionless Groups 82

NOMENCLATURE

LATIN SYMBOLS

A_f^o	Austenite transformation finish temperature
A_s^o	Austenite transformation start temperature
c	Speed
c_p	Specific heat capacity
e	Specific internal energy
$\overline{F}$	Specific body force
$G(T)$	Phase function for SMA
g	Gravitational acceleration
Gr	Grashof number
H	Specific latent heat of transformation
k	Thermal conductivity
L	Length of major axis of ellipse
L	Lower diagonal implicit operator
M_f^o	Martensite transformation finish temperature
M_s^o	Martensite transformation start temperature

N ..... Time level

$\overline{n}$ ..... Unit vector normal to surface W

$P(T)$ ..... Phase function for SMA

p ..... Pressure

Pe ..... Peclet number

Pr ..... Prantl number

$\overline{q}$ ..... Heat flux

$\overline{R}$ ..... Surface force

r ..... Relaxation parameter

Re ..... Reynolds number

S ..... Normal distribution standard deviation

T ..... Temperature

U_∞ ..... Freestream velocity

U ..... Lower diagonal implicit operator

$\overline{v}$ ..... Velocity vector (2D)

W ..... Control volume surface

w ..... Sample variable

(x, y) ..... Eulerian coordinates

GREEK SYMBOLS

α_i ..... Runge Kutta stage coefficient

β ..... Volumetric thermal expansion coefficient

Δt ..... Time step

δ ..... Difference operator; δ^+ forward, δ^- backward, δ central

δ_K ..... Kronecker delta matrix

ϵ ..... Error in the solution

θ_x ..... Phase angle of Fourier decomposed error

λ ..... Implicit parameter

μ ..... Viscosity

ξ ..... Martensite volume fraction

ρ ..... Density

τ ..... Viscous stress tensor

ϕ ..... Irrotational potential

Ψ ..... Stability parameter of diffusion term

ψ ..... Viscous correction stream function

Ω ..... Control volume

ω ..... vorticity

(ξ, η) ..... Computational coordinates

CHAPTER 1

INTRODUCTION

1.1 Shape Memory Alloys

Shape memory alloys (SMA's), or smart materials as they are also known, were first discovered in the 1960's [7], [27], [38]. The earliest shape memory alloys were comprised of nickel and titanium. Alloys using other materials [18], [40] were later discovered, but nickel - titanium continues to be the most useful for designers. This is due to the fact that nickel titanium alloys provide the most desirable combination of material properties [20]. An additional benefit is the biocompatibility of this alloy [32].

The usefulness of shape memory alloys is their ability to 'remember' a shape. Shape memory alloys can exist in two different crystal phases in the solid state. A specimen of shape memory alloy can have a different physical shape for each phase. The shape of the material in both of the phases can be controlled by designers. The material can be made to return to a 'remembered' shape by either a change in temperature or stress. The ability of a smart material specimen to change form between two trained

shapes, activated by temperature, is known as the two way shape memory effect [26].

The shape change of a shape memory alloy is facilitated by an ability to sustain recoverable strains of up to 8% [18]. Different alloys have different maximum recoverable strains. The larger the recoverable strain, the more useful the shape memory alloy is to designers.

Smart materials have been applied to a wide range of applications in research. This is because of the usefulness of a material which changes shape in response to an external temperature change or applied stress. One application of smart materials is as actuators [2]. Commercially, shape memory alloys have the greatest potential for application as actuators [11]. An additional application is in aerospace engineering, where smart materials can be used to actively change the shape of the lifting surface of an aerodynamic body [3]. Biomedical applications are also being developed [46].

As mentioned previously the maximum recoverable strain of a shape memory alloy depends on the composition of the alloy. The temperature at which a specimen will change shape is also dependent upon the alloy composition [31]. Both the constituent materials and their relative quantities affect these properties. An additional factor which affects the recoverable strain is the process used to produce the specimen being considered [18]. Therefore it is necessary to do testing on an alloy specimen to determine its individual material properties and phase change capabilities . These properties are normally supplied by the manufacturer of the sample [1]. For this reason, experimental testing is the commonly used technique for analysis and design with shape memory alloys, the SMART lab of Texas A&M being an example [45].

1.2 Present State of Field

Research in the field of smart materials focuses on either the area of constitutive modelling or applications. Possible applications for shape memory alloys were mentioned above. A summary with short descriptions of possible applications can be found in Birman [5]. Research into applications is primarily concerned with developing control systems for SMA actuators, the work of Banks *et al* [2] being one example. Constitutive modelling is the attempt to develop analytical models to describe the behavior of shape memory alloys, such as the work of Boyd and Lagoudas [6].

Development of a new constitutive model is beyond the scope of this work. The constitutive model proposed by Bhattacharyya and Lagoudas [4] will be used to describe the behavior of the shape memory alloy. In addition, evaluating this model and comparing it against other available models is also beyond the scope of the current work. A review of constitutive models for shape memory alloys can be found in Birman [5].

As stated previously, determining the properties of a sample of shape memory alloy requires testing of the specific sample. Material properties of shape memory alloy are sensitive to the relative quantities of the constituent elements. Material properties for specimens are provided by the manufacturer of the specimen. For these reasons design of devices with shape memory alloys is experimentally based for the most part.

The large scale applicability of smart materials may be limited by difficulty in consistently producing samples with predictable material properties. This is a further consequence of the sensitivity of shape memory alloy properties to the constituent elements.

1.3 Convective Heat Transfer

The shape change of a shape memory alloy is driven by a temperature change or the application of an external stress. A commonly used technique is to increase the temperature by resistive heating with an applied voltage; the temperature is then lowered by convective heat loss to the surrounding environment [29]. The heating stage is when the useful shape change occurs and work is done by the shape memory alloy device. The cooling phase is the return of the specimen to the original shape. The energy loss needed to decrease the temperature of the alloy is shed in the form of heat to the environment, which is normally a fluid (air or water). Therefore the thermal interaction at the interface between the shape memory alloy and the surrounding fluid is a crucial phenomenon.

From the literature, prior research in thermal interaction between a solid immersed in a fluid has focused on either the temperature of the surrounding fluid [10], [30], or the temperature of the solid [14], but not both at the same time. The thermal influence of whichever portion of the domain not being considering (fluid or solid) is modelled by a boundary condition. The two commonly used boundary conditions are constant temperature at the surface or constant heat flux across the surface [28], [39]. This requires an assumption to be made for either the temperature of the interface or the heat flux across the interface.

To accurately capture the phase of the material as it undergoes the phase change it is necessary to know the temperature of the specimen. Therefore the temperature distribution of the shape memory alloy specimen must be known. To accurately model the local convective heat losses of the shape

memory alloy it is necessary to know the temperature distribution of the surrounding fluid. Therefore the temperature distribution of the shape memory alloy and the surrounding fluid must be determined.

For the present work the temperature of the solid is of primary importance. However, using a boundary condition to model the thermal effects of the fluid on the solid is not acceptable. An accurate representation of the local convective heat losses from the shape memory alloy is required to study the phase change over the specimen. A discrete element analysis will be used to study the phase at discrete points over the specimen. A boundary condition developed from an average over the entire surface of a specimen would reduce the accuracy of the discrete element analysis. Boundary conditions which are not averaged over the entire surface have been experimentally determined for some geometries [12]. However these are usually for steady state problems.

The solution is expected to evolve in time as the shape memory alloy changes phase. As the simulation develops in time the average temperature of the smart material will change but the freestream temperature of the surrounding fluid will remain constant. The change in the temperature difference between the fluid and solid with time will cause the thermal interaction between them to change with time as well. It would not be possible to capture this time dependence accurately with a boundary condition on the surface of the solid which models the effects of the fluid. It is necessary to know the temperature distribution in the surrounding fluid explicitly to accurately model the convective heat losses.

For this work a new technique is needed at the boundary which will ac-

curately represent the physics of the heat transfer. A boundary condition is needed which will not require an assumption to be made regarding an interface temperature or surface heat flux amount. Thermal phenomena at the interface between the fluid and shape memory alloy must be accurately modelled without incorrectly affecting the solution. A new boundary condition will be described which represents the physics and allows the solution to develop with time.

CHAPTER 2

PROBLEM DESCRIPTION

2.1 Selected Application

The capability of the completed analytical and numerical work will be demonstrated with a specific application. The selected application is an inferior vena cava filter (IVCF) comprised of a shape memory alloy. An example of a currently available 'smart' IVCF is the Simon Nitinol Filter® developed and manufactured by Nitinol Medical Technologies, Inc. [31], [32], [33].

IVCF's are a surgical attempt at preventing a pulmonary embolism. A pulmonary embolism is the possible fatal result of a blood clot reaching the lungs through the circulation system. The majority of pulmonary embolisms begin as deep leg thromboses which travel through the venous pathway to the lungs [22]. IVCF's are placed in the inferior vena cava to physically prevent any large clots from reaching the lungs. Surgical implanting of the filter is achieved through an angiographic introducer inserted into a large vein in one of the extremities.

2.2 Simon Nitinol Filter®

The Simon Nitinol Filter® will be modelled in this work, it can be seen in Figure 2.1, taken from [46].

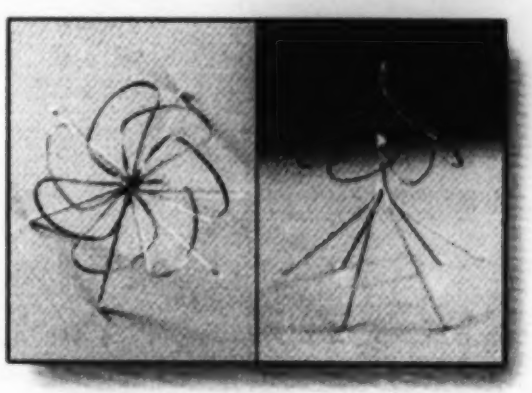

Figure 2.1: Simon Nitinol Inferior Vena Cava Filter

As shown in Figure 2.1 the device is in the austenitic phase. In this material phase the IVCF is in the designed filter shape. The shape of the device in the martensitic state is a drawn out linear shape, with a smaller cross sectional area and greater axial length. An explanation of the phase change of a shape memory alloy will be given in Section 3.3.1.

The top curved portion of the device is intended to perform the majority of the filtering duties. The lower straight portion of the device, consisting of six equally spaced legs, is designed to anchor the filter to the walls of the inferior vena cava.

2.3 Insertion of Inferior Vena Cava Filter

Following is the insertion procedure as described by Simon *et al* in [31]. This information is important as it will be used for selection of values for initial conditions and boundary conditions. Correct boundary and initial conditions are part of an accurate and complete problem formulation. Information regarding the phase change of the filter is included in the description. As well, the benefit of a shape memory alloy IVCF is explained.

The procedure begins with a bag of saline solution being chilled for half an hour in ice. This saline is then drawn into the angiographic introducer which will be used to implant the filter. Chilling the filter with ice results in the initial phase of the material being martensite. In this phase the material is pliable, and the initial shape is a drawn out linear form which reduces the overall cross sectional area. The reduced cross sectional area in the martensitic phase is the main benefit of the smart material filter. The reduced cross section requires a smaller diameter of tubing to insert the filter into place, which means a smaller incision is needed. The Simon Nitinol Filter® requires the smallest diameter tubing for insertion of all commercially available IVCF's [46]. This is beneficial since the incision used to implant the filter can itself result in a thrombosis, the very problem the filter is intended to minimize.

The angiographic introducer is inserted into the blood stream and directed to the desired location in the inferior vena cava. A plunger is used to expel the filter from the angiographic introducer. As the filter is forced from the introducer its external environment changes from stationary saline at $0°C$ to blood flow at $37°C$. The higher temperature of the surrounding

flow causes the smart material to change from martensite to austenite. This change in phase results in a change in shape, and the filter transforms to the designed filter shape. Hooks on the end of the filter legs sink into the veinal walls to secure the filter in place.

The phase change of the filter is actuated differently than other applications where shape memory alloys are used as actuators. As mentioned previously, the phase change is normally initiated by resistive heating of the device to increase the temperature. The temperature is decreased by allowing the additional heat to be lost convectively to the surrounding environment. For a shape memory alloy IVCF the temperature increase is a result of convective heat gained from being immersed in blood flow at body temperature. This is the reason the thermal interaction between the shape memory alloy and the surrounding fluid is a key phenomenon for this work. The phase change will occur as a result of heat gained convectively across the shape memory alloy surface.

2.4 Computational Domain

The real three dimensional and time dependent problem would be computationally expensive and difficult to formulate analytically. Reducing the problem to two dimensions and assuming no geometry change simplifies the analytical formulation. This also makes the numerical solution less computationally expensive, and more importantly realistically solvable with available resources. However these assumptions will affect the applicability of the model to the real problem.

Assuming there is no geometry change has the greatest limiting effect on

the applicability of the model. The very nature of the problem is a shape memory alloy which changes shape. As the alloy changed shape it would influence the fluid flow around it and thus change the thermal interaction between the fluid and shape memory alloy. Not incorporating this interaction into the simulation reduces how well the model represents the true problem. However, a numerical solution with changing geometry would be much more computationally expensive than a constant geometry problem. Variable geometry could be incorporated into the formulation as future work, but is beyond the scope of this project. The geometry will be assumed constant as an approximation. The thermal interaction between the fluid and solid is the primary interest of this work, the shape change is secondary.

A cross-sectional plane or slice of the 3D geometry will be selected as the two dimensional plane. Using a 2D geometry of this form instead of three dimensions is a common technique used in numerical analysis and design of turbomachinery.

Selection of the proper two dimensional plane is crucial to ensure accurate representation of the true problem in a two dimensional manner. Consider Figure 2.2, a two dimensional diagram of the inferior vena cava and filter. This is a cross sectional view, looking down the axis of the vena cava.

In this view the wall of the IVC and the cylindrical cut plane extend out of the page. The cut plane is the two dimensional plane which will be used as the coordinate axis for this work. The radial location of the cut plane has been selected such that the anchor legs of the IVCF are intersected at the radial midpoint between the center of the IVC and the venal wall. Only the anchor leg portion of the filter has been included in the model to simply the

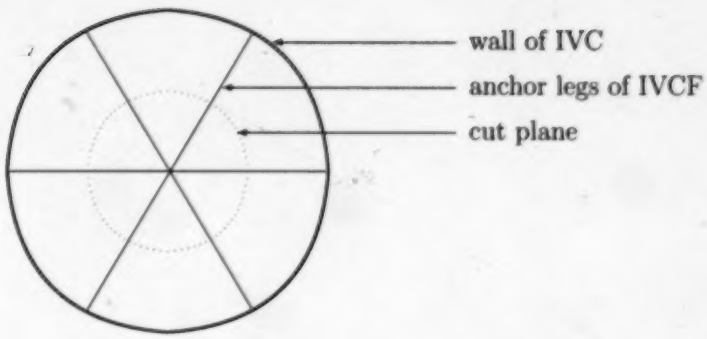

Figure 2.2: Inferior Vena Cava Viewed Along Axis

analysis.

When the cut plane is chosen as shown in Figure 2.2 the domain becomes periodic. Only 1/6 of the circumference of the cut plane needs to be considered, provided the proper periodic boundary conditions are applied.

The cut plane intersects each of the anchor legs once, and at an angle. The circular cross section of the anchor legs results in an elliptical projection on the cut plane. The top portion of the filter will not be included in the model to further simplify the analysis. The domain must be extended a suitable distance upstream and downstream of the intersection point with the anchor legs of the IVCF. A suitable distance is one which allows the flow phenomena to develop without extending too far upstream or downstream. An overly large computational domain will result in extraneous calculations being completed.

The plane can be cut longitudinally and unwrapped, as demonstrated in Figure 2.3.

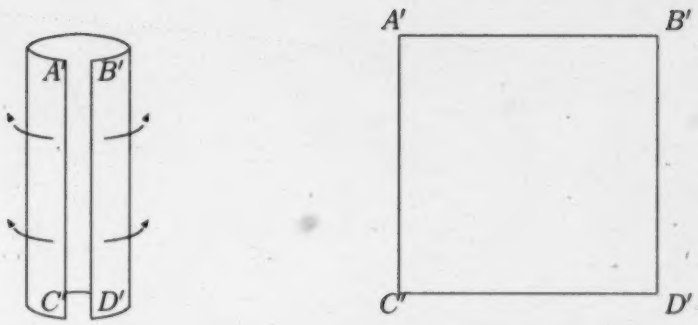

Figure 2.3: Mapping of Curved Plane onto Flat Space

Once the cut plane is mapped onto a flat coordinate axis, and a suitable upstream and downstream distance is selected, the domain of the problem is as shown in Figure 2.4.

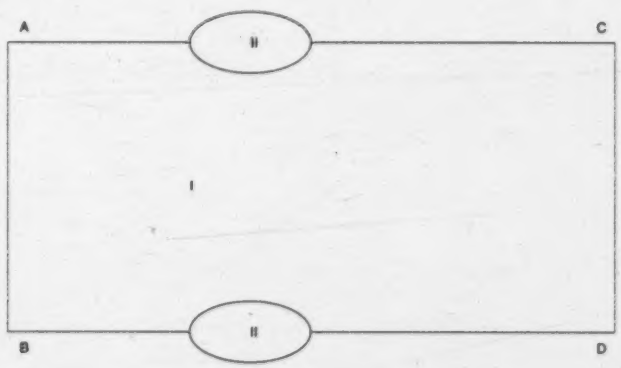

Figure 2.4: Domain of Problem

In Figure 2.4 the distance $A-B$ and $C-D$ is 1/6 the distance of $A'-B'$ and $C'-D'$ in Figure 2.3.

From Figure 2.4, region I is the fluid portion of the domain, region II is the anchor leg of the IVCF. The inlet is along A - B, and the outlet is at C - D, meaning the direction of fluid flow is left to right. Periodic boundary conditions will be applied along A - C and B - D. A detailed explanation of the applied boundary conditions will be given later.

CHAPTER 3

GOVERNING EQUATIONS

3.1 General Form of Equations

The equations which are relevant to this problem are the conservation of mass, momentum and energy. They are shown below in integral form for a volume Ω bounded by a surface W:

$$\frac{\partial}{\partial t}\iiint_{\Omega} \rho \, d\Omega + \iint_{W} \rho(\overline{v} \cdot \overline{n}) \, dW = 0 \tag{3.1}$$

$$\frac{\partial}{\partial t}\iiint_{\Omega} \overline{v}\rho \, d\Omega + \iint_{W} \overline{v}\rho(\overline{v} \cdot \overline{n}) \, dW = \iiint_{\Omega} \rho\overline{F} \, d\Omega + \iint_{W} \overline{R} \, dW \tag{3.2}$$

$$\frac{\partial}{\partial t}\iiint_{\Omega} \rho(e + \frac{1}{2}(\overline{v} \cdot \overline{v})) \, d\Omega = -\iint_{W} (\overline{n} \cdot \overline{q}) \, dW + \iint_{W} (\overline{R} \cdot \overline{v}) \, dW + \iiint_{\Omega} \rho(\overline{F} \cdot \overline{v}) \, d\Omega \tag{3.3}$$

(For definitions of the variables used, please see the Nomenclature section at the beginning of the text.)

By applying Stokes' Theorem and Leibnitz's Theorem [25] to the above equations it is possible to write them in differential form.

$$\frac{\partial \rho}{\partial t} + \nabla \cdot (\rho \overline{v}) = 0 \tag{3.4}$$

$$\rho \frac{D\overline{v}}{Dt} = \rho \overline{F} - \nabla p + \nabla \cdot \tau \tag{3.5}$$

$$\rho \frac{De}{Dt} = -\nabla \cdot \overline{q} - p \nabla \cdot \overline{v} + \tau : \nabla \overline{v} \tag{3.6}$$

Here it has been assumed that the surface force is comprised of pressure and viscous stresses.

$$\overline{R} = \hat{n}(-p\delta_K + \tau) \tag{3.7}$$

It is also assumed that only conservative body forces are present. In the differential form it will be easier to manipulate the equations as needed to simplify them to better match the problem being studied. Still, the equations as written are quite general and apply to a wide range of problems.

3.2 Modification of Equations

3.2.1 Boussinesq Approximation

It was first noted by Boussinesq that for some problems it is not necessary to solve the conservation equations as written above. There are a class of problems where changes in material properties such as density and viscosity are a result of only temperature changes of moderate amounts. An order of magnitude analysis reveals some simplifications which may be made to the governing equations [8].

In order to be able to apply the Boussinesq approximation, changes in density must be due only to changes in temperature. Making this assumption allows us to write density as a Taylor series expansion with respect to temperature; second order and higher terms will be neglected:

$$\rho(T) = \rho_o + \frac{d\rho}{dT}dT \tag{3.8}$$

where ρ_o refers to the density at some reference temperature.

Making use of:

$$\beta \equiv -\frac{1}{\rho}\frac{\partial \rho}{\partial T}\bigg|_p \tag{3.9}$$

We can write the following since density is assumed to be only a function of temperature:

$$\beta \equiv -\frac{1}{\rho}\frac{\partial \rho}{\partial T}\bigg|_p = -\frac{1}{\rho}\frac{d\rho}{dT} \tag{3.10}$$

Substituting Eqn.(3.10) into Eqn.(3.8), density can now be approximated as:

$$\rho = \rho_o(1 - \beta\Delta T) \tag{3.11}$$

Considering that β is of the order $O(10^{-3})$ to $O(10^{-4})$ for most fluids, moderate changes in temperature equate to small changes in density.

The values used for β and ρ_o are $\beta = 0.361(10^{-3})K^{-1}$ and $\rho_o = 1050kg/m^3$ [33]. As an approximation, the value of β for water at $37°C$ has been used for the β value of blood.

Using the above expression it is possible to write any density gradients as functions of temperature. This removes density as an independent variable,

reducing the number of unknowns. Gradients in density can be represented as follows:

$$\nabla\rho = -\beta\rho_o\nabla T \tag{3.12}$$

One limitation that this places on the problem is that the Mach number must be sufficiently small, $M < 0.3$, so that there are no velocity induced density gradients. Using the speed of sound for water again as an approximation, the Mach number is of order $O(10^{-5})$, which is sufficiently small. The limitations of low Mach number and moderate temperature changes place some restrictions on the possible applications of any solution algorithm developed. However, it is felt that the Boussinesq approximation is one which must be made in this case. If it were not applied it would be necessary to consider the fully compressible fluid flow problem, this would complicate the solution process by increasing the number of independent variables.

3.2.2 Application of Assumptions to Governing Equations

In order to make the general conservation equations more applicable to this specific problem, a few basic assumptions regarding the physics of the problem must be made. The first simplification will be to apply the Boussinesq approximation to the continuity equation. Substituting Eqn.(3.11) into Eqn.(3.4) gives the following:

$$\frac{D\rho}{Dt} + \rho\nabla\cdot\overline{v} = 0 \tag{3.13}$$

$$\frac{D[\rho_o - \rho_o\beta\Delta T]}{Dt} + (\rho_o - \rho_o\beta\Delta T)\nabla\cdot\overline{v} = 0 \tag{3.14}$$

$$\frac{D\rho_o}{Dt} - \rho_o\beta\frac{D(\Delta T)}{Dt} + \rho_o\nabla\cdot\overline{v} - \rho_o\beta\Delta T\nabla\cdot\overline{v} = 0 \tag{3.15}$$

$$\rho_o \nabla \cdot \overline{v} - \beta \rho_o \left[\frac{D(\Delta T)}{Dt} + \Delta T \nabla \cdot \overline{v} \right] = 0 \tag{3.16}$$

$$\rho_o \nabla \cdot \overline{v} = \beta \rho_o \left[\frac{D(\Delta T)}{Dt} + \Delta T \nabla \cdot \overline{v} \right] \tag{3.17}$$

Variations in T and $\overline{v}$ are assumed to be of the same order. Recalling that β is of the order $O(10^{-3})$ to $O(10^{-4})$, the left hand term will be three to four orders smaller than the right hand term in the above equation.

This allows us to simplify Eqn.(3.17) as follows:

$$\nabla \cdot \overline{v} = 0 \tag{3.18}$$

Another assumption to be made is that the fluid is Newtonian with constant viscosity. Applying the Boussinesq approximation allows us to simplify the form of the shear stress tensor, τ, in the following manner:

$$\nabla \cdot \tau = \nabla(\mu \left(\nabla \overline{v} + (\nabla \overline{v})^T \right) - \mu \frac{2}{3} (\nabla \cdot \overline{v}) \delta_K) \tag{3.19}$$

Applying Eqn.(3.18) simplifies this to:

$$\nabla \cdot \tau = \mu \nabla^2 \overline{v} \tag{3.20}$$

It is known that this is not the most accurate model for the viscosity of blood. A more accurate choice would be to model it as a Casson fluid [37]:

$$\mu_{\text{eff}} = \frac{\tau}{\left| \frac{dv}{dy} \right|} = \frac{\left[\sqrt{(\tau_y)} + \sqrt{\left(\mu \left| \frac{dv}{dy} \right| \right)} \right]^2}{\left| \frac{dv}{dy} \right|} \tag{3.21}$$

where μ_{eff} is the effective viscosity, τ is a shear stress, τ_y is the yield stress and μ is a constant.

However, viscosity will not be modelled in this manner since the rheology of the fluid is not the primary interest of the current work; the thermal interaction between the fluid and solid is the primary interest.

From Eqn.(3.21) it can be seen that when τ_y is taken to be zero that $\mu_{eff} = \mu$. Therefore assuming a Newtonian fluid is a first order approximation.

As was mentioned previously it has been assumed that only conservative body forces are present. This assumption regarding body forces will be taken a step further by assuming that gravity is the only body force present. The gravity force will be written as a potential in the following manner:

$$\overline{F} = -\nabla(gy) \tag{3.22}$$

Here g is given the scalar value of 9.8.

The energy equation will be manipulated from its previous form with e as the independent variable to temperature as the independent.

$$e = c_p T \tag{3.23}$$

Later the energy variable will be discussed in more detail. An additional term will be added to the right hand side of the above expression for the energy equation in the solid. The purpose of this term will be to capture the effects of the phase change.

Fourier's law will be applied to the conduction term to reduce the number of independent variables:

$$\overline{q} = -k\nabla T \tag{3.24}$$

It can be shown that the viscous heating term in Eqn.(3.6), $\nabla : \tau$, is eight orders of magnitude smaller than the convection term. Therefore this term will be neglected.

Once the above simplifications have been applied to the conservation equations, they appear as follows:

$$\nabla \cdot \overline{v} = 0 \tag{3.25}$$

$$\rho \frac{D\overline{v}}{Dt} = -\rho \nabla (gy) - \nabla p + \mu \nabla^2 \overline{v} \tag{3.26}$$

$$\rho \frac{D(c_p T)}{Dt} = \nabla (k \nabla T) \tag{3.27}$$

3.2.3 Governing Equations in Fluid Region

Now the specific form of the conservation equations applicable in the fluid region will be considered. One additional assumption to be made in the fluid region is that the thermal conductivity of the fluid is constant. From the literature a value of $k = 0.5\ W/mK$ will be used for blood [37]. Again, constant thermal conductivity is a first approximation and may be revisited at a later time. For the model problem being studied the largest contributor to variations in thermal conductivity would be temperature changes. For example, for water between $0°C$ and $37°C$, the expected temperature extremes, thermal conductivity changes by 10%. This change is not as drastic as the order of magnitude increase the thermal conductivity of the shape memory alloy undergoes. The thermal conductivity of the smart material will be explained in Section 3.3.4.

If the conservation of momentum were left as it is in Eqn.(3.26), pressure would be an additional independent variable. By transforming the momen-

tum equation from this form to the vorticity transport equation, we will eliminate p completely from the equations. When completing this transformation, density will be considered as variable only in the body force term. An order of magnitude analysis indicates that variable density has the most substantial effects on the equation in this term. This is an additional application of the Boussinesq approximation [8].

Transforming Eqn.(3.26) to the vorticity transport equation requires the following steps. First density is variable only in the body force term by the following argument:

$$\rho\frac{D\overline{v}}{Dt} = -\rho\nabla(gy) - \nabla p + \mu\nabla^2\overline{v} \tag{3.28}$$

Substitute Eqn.(3.11) for the density:

$$(\rho_o - \rho_o\beta\Delta T)\frac{D\overline{v}}{Dt} = -(\rho_o - \rho_o\beta\Delta T)\nabla(gy) - \nabla p + \mu\nabla^2\overline{v} \tag{3.29}$$

Simplify:

$$\rho_o\frac{D\overline{v}}{Dt} - \rho_o\beta\Delta T\frac{D\overline{v}}{Dt} = -(\rho_o - \rho_o\beta\Delta T)\nabla(gy) - \nabla p + \mu\nabla^2\overline{v} \tag{3.30}$$

Collect terms:

$$\rho_o\frac{D\overline{v}}{Dt} = -(\rho_o - \rho_o\beta\Delta T)\nabla(gy) - \nabla p + \mu\nabla^2\overline{v} + \rho_o\beta\Delta T\frac{D\overline{v}}{Dt} \tag{3.31}$$

Assume the following:

$$\left|\rho_o\beta\Delta T\frac{D\overline{v}}{Dt}\right| \sim O(0)^2 \tag{3.32}$$

$$|\rho_o\beta\Delta T\nabla(gy)| \sim O(0) \tag{3.33}$$

which is valid for low velocity flows.

The result is the following form of the momentum equation:

$$\rho_o \frac{D\overline{v}}{Dt} = -\rho\nabla(gy) - \nabla p + \mu\nabla^2\overline{v} \tag{3.34}$$

Next the curl of the equation is taken:

$$\nabla \times \left[\rho_o \frac{D\overline{v}}{Dt} = -\rho\nabla(gy) - \nabla p + \mu\nabla^2\overline{v}\right] \tag{3.35}$$

Carrying the cross product inside the brackets:

$$\rho_o \frac{D\omega}{Dt} + (\omega\cdot\nabla)\overline{v} - \omega(\nabla\cdot\overline{v}) = -(\nabla\rho\times\nabla(gy)) - (\nabla\times\nabla p) + \mu\nabla^2\omega \tag{3.36}$$

Applying Eqn.(3.18) to the third term on the left hand side allows this term to be eliminated. The second term on the left hand side is zero since we are considering a two dimensional problem. The second term on the right hand side is zero since it is the cross product of a gradient. These simplifications result in the following form of the equation:

$$\rho_o \frac{D\omega}{Dt} = -(\nabla\rho\times\nabla(gy)) + \mu\nabla^2\omega \tag{3.37}$$

As stated above, pressure has been removed as an independent variable from the formulation.

Applying the approximation for density gradients, Eqn.(3.12) to the above, and dividing through by ρ_o results in the following:

$$\frac{D\omega}{Dt} = \beta g(\nabla T\times\nabla y) + \frac{\mu}{\rho_o}\nabla^2\omega \tag{3.38}$$

This is the form of the vorticity transport equation which will be used for this work. The first term on the right hand side of Eqn.(3.38) generates vorticity in the presence of x-direction temperature gradients, coupling the temperature and velocity fields in the fluid. From the literature, this is the

equation used to study the effects of moderate temperature changes on fluid flow [9], [23], [24], [39].

The thermal conductivity and heat capacity will be assumed constant for the fluid in the solution of the energy equation. This is an acceptable assumption since the flow is a low velocity incompressible flow. Changes to these parameters would be primarily due to thermal changes, and only moderate variations in temperature are expected.

Starting with Eqn.(3.27):

$$\rho \frac{D(c_p T)}{Dt} = \nabla(k(\nabla T)) \tag{3.39}$$

Constant k and c_p results in the following form of the equation:

$$\rho c_p \frac{DT}{Dt} = k\nabla^2 T \tag{3.40}$$

Next apply Eqn.(3.11) for the density:

$$(\rho_o - \rho_\beta \Delta T) c_p \frac{DT}{Dt} = k\nabla^2 T \tag{3.41}$$

$$\rho_o c_p \frac{DT}{Dt} = k\nabla^2 T + \rho_o \beta \Delta T \frac{DT}{Dt} \tag{3.42}$$

Recalling that β is of order O(10^{-3}) - O(10^{-4}) for most fluids, the last term on the right hand side is three to four orders of magnitude smaller than the left hand side. As a first order approximation the last term on the right hand side will be dropped.

The final form of the energy equation in the fluid is the following:

$$\rho_o c_p \frac{DT}{Dt} = k\nabla^2 T \tag{3.43}$$

with $c_p = 3.85(10^3) J/kgK$, $k = 0.5 W/mK$ and $\rho_o = 1050 kg/m^3$.

Eqn.'s (3.38) and (3.43) are the ones which will be solved in the fluid region of the domain.

3.3 Modeling of Shape Memory Alloy Properties

3.3.1 Property Model

Shape memory alloys in the solid state can exist at two different phases, martensite and austenite. It is possible for the material to change between the two phases as a result of either external stress or heat addition/removal. The phase names refer to the type of transformation which occurs and are not references to the different phases of steel, where their use originated [40]. A martensitic transformation is one in which heat is removed. The transformation is governed by temperature and not time. Martensite is the cold temperature phase and austenite is the high temperature phase, sometimes referred to as the parent phase. In each of the two phases the molecules of the material are arranged in two different ways in a crystal structure.

When changing phases the crystal structure undergoes what is known as a displacive transformation. The arrangement of the molecules in the structure relative to each other does not change, they uniformly rearrange into a new formation. Consider the two dimensional representation of a displacive transformation shown in Figure 3.1.

In Figure 3.1 a direction of travel for the phase boundary has not been shown. If the matrix structure were cooling down the phase boundary would travel towards the bottom of the page as the temperature dropped and more martensite would be formed. If the matrix structure were being heated the phase boundary would travel towards the top of the page as the temperature increased and more austenite would be formed. This represents a single crystal sample of smart material since the entire crystal matrix is oriented

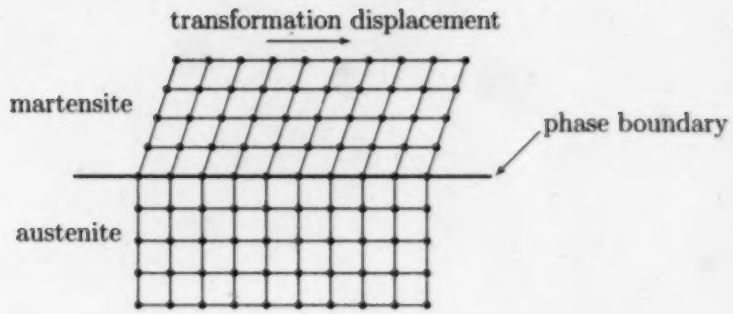

Figure 3.1: Displacive Phase Transformation between Austenite and Martensite

in the same direction.

Polycrystal samples of smart material are comprised of many grains each having their own orientation direction. When a phase change is initiated, a phase boundary forms within in each crystal, and then travels outward to the grain boundary as the phase change progresses. The shape memory alloy device being studied for this work is a polycrystal.

For a numerical solution the domain is discretized into small divisions called grid cells. There is no guarantee that a grid will be generated such that the grid lines will coincide with all phase boundaries. The possibility also exists for multiple grains to be contained in a single grid cell, unless the grid in the solid area is adaptively regridded to ensure only one grain exists in one cell, or only one phase exists within one cell. The smallest geometric level to which a numerical solution can accurately resolve an independent

variable is the size of a grid cell. For these reasons it would be difficult to accurately track multiple phase boundaries in a grid cell. A property model is needed which will functionally describe the state of the material of a grid cell. This will average the effects over a grid cell of multiple grains being composed of different quantities of the two phases.

By using a cell averaged property model to describe the phase of the smart material we need not track the travelling phase boundary. If a travelling phase boundary were to be captured numerically it would be necessary to solve Eqn.'s (3.4) and (3.5) for the velocity field in the solid. It would also be necessary to solve for the material phase of each individual grain within the solid. Instead of having multiple grains composed of varying amounts of both phases, an entire grid cell as a whole will be assumed to be uniformly at some point in the phase change. The material property models are then constructed using this cell averaged concept.

Using a cell averaged approach to the material phase limits the possible applications of the material model. This model may only be applied to problems where the shape memory alloy being studied is a polycrystal. A single crystal sample of shape memory alloy could not be represented using this model. Individual crystals of shape memory alloy exist in one of two states, martensite and austenite. The cell averaged material phase model allows for the state of the material to exist in combinations of martensite and austenite. As explained previously, this is done to represent the fact that some grains within a grid cell could be martensite and simultaneously some grains within the same grid cell could be austenite.

3.3.2 Mathematical Representation of Phase

Shape memory alloys are materials which undergo a change in crystal structure in response to an applied stress or temperature change. The SMA may have different material properties for the two phases, and may have varying material properties during the phase change. To properly model the changing properties of the SMA, it is necessary to model the phase change. Material properties which can change as a result of the phase are density, thermal conductivity, electrical resistivity, and heat capacity.

To simplify the problem a zero stress state, $\overline{\sigma} = 0$, will be assumed. This makes the phase of the SMA a function of temperature only. By removing stress from the phase model formulation we reduce the number of independent variables and the number of equations which would have to be solved. Consider the following formulation for the state of a smart material including both temperature and stress:

$$\xi_A(T,\sigma) = 1 + \int_{M_s^o + \frac{\sigma}{D}}^{T} P(\tilde{T},\sigma)\, d\tilde{T} \tag{3.44}$$

where D is a measure of how the transformation temperature is affected by the stress level. In addition, a thermoelastic coupling term would have to be added to the energy equation being solved in the solid.

This assumption limits the possible applications of the phase model to zero stress conditions only. This is an important limitation since one application for smart materials is as actuators where they are required to carry a load. For this work the phase change of the material will be driven by temperature change and therefore there is no need for stress in the phase model.

The thermal conductivity will be modeled as a function of the phase, while the product of density and specific heat capacity of the solid will be assumed constant. This is a reasonable approximation since thermal conductivity changes by an order of magnitude, while the heat capacity changes no more than 11% [1].

In nature, it is the state of the material which determines the material properties. To reduce the number of independent variables which need to be solved for numerically, the material properties will be written as functions of temperature. An analytical expression will be used which expresses the state as a function of temperature.

$\xi(T)$ is the austenite volume fraction of the SMA. ξ ranges between 0 and 1, when $\xi = 0$ the material is martensite, when $\xi = 1$ the material is austenite. This expression tracks the phase of the material within the transformation process. The two functional forms of $\xi(T)$ are given below for austenite and martensite respectively [1]:

$$\xi_A(T) = 1 + \int_{M_s^o}^{T} P(\tilde{T})\, d\tilde{T} \tag{3.45}$$

$$\xi_M(T) = \int_{A_s^o}^{T} G(\tilde{T})\, d\tilde{T} \tag{3.46}$$

where $\tilde{T}$ is a dummy integration variable, T is the temperature at which the state is being determined, M_s^o is the temperature at which the martensite transformation starts and A_s^o is the temperature at which the austenite transformation starts. The subscripts on ξ refer to the material phase.

The two functions P and G are taken to be normal distributions [19]:

$$P(T) = \frac{1}{S\sqrt{2\pi}} \exp\left[-\frac{1}{2}\left[\frac{T - \frac{1}{2}(M_s^o + M_f^o)}{S}\right]^2\right] \tag{3.47}$$

$$G(T) = \frac{1}{S\sqrt{2\pi}} \exp\left[-\frac{1}{2}\left[\frac{T - \frac{1}{2}(A_s^o + A_f^o)}{S}\right]^2\right] \tag{3.48}$$

where $S = 1.5$ is the standard deviation of the normal distributions P and G, M_f^o is the temperature at which the martensite transformation finishes and A_f^o is the temperature at which the austenite transformation finishes.

As stated by Bhattacharyya and Lagoudas [4], the selection of the normal distribution for the form of Eqn.'s (3.47) and (3.48) is not a unique one. There are several possible functions which could have been used; such as the Gaussian, Poisson and Weibull functions. The normal distribution was selected by Bhattacharyya and Lagoudas to represent the physics of a polycrystal. Slight variations in composition between individual crystals in a polycrystal sample are expected to result in the distribution of the transformation temperatures around some mean value.

Eqn.'s (3.47) and (3.48) are fitted to experimental data with S, A_s^o, A_f^o, M_s^o and M_f^o being manipulated to match the data. Values of these parameters are valid for only the sample of smart material for which they are experimentally determined. Material properties used for this work are taken from the paper by Amalraj *et al* [1].

The following are the temperature values used for start and finish temperatures of the phase changes:

$$\begin{aligned} A_s^o &= 288K \\ A_f^o &= 298K \end{aligned} \tag{3.49}$$

$$M_s^o = 275K$$
$$M_f^o = 265K$$

These values were chosen to reside between the initial temperatures of the fluid and solid.

The integral of P is normalized so that over the martensite transformation temperatures it equates to -1. The integral of G is normalized so that over the austenite transformation temperatures it equates to 1.

It is now possible to write expressions for the material properties of the SMA as functions of temperature.

3.3.3 Functional Fit to Phase Equation

The phase equations described by Eqn.'s (3.47) and (3.48) require an integration of the normal distribution functions, Eqn.'s (3.45) and (3.46). Unfortunately, there are no analytical solutions for these integrals, hence an alternative solution to analytical integration is required.

Possible options are a numerical integration to the equation, an approximate function, or tabulated values with interpolation. A numerical integration would be computationally expensive since it would need to be computed at each grid cell for all time steps. Interpolating tabulated values would also be computationally expensive since it would require sorting data at each grid cell for all time steps. If a suitable approximate function could be found it would be the least computationally expensive of the three options, requiring only the evaluation of a single function at each grid cell for all time steps.

To aid in finding a functional approximation, a numerical integration was completed over the austenite to martensite transformation temperature

range. The numerical integration had a maximum error of $4.92(10^{-6})$ [34] over the transformation temperature range, relative to the maximum value of 1 for Eqn.(3.45). The numerical integration was only completed for the austenite to martensite transformation temperature range. Any function used for this transformation could be translated along the temperature axis to be used for the martensite to austenite transformation.

The numerical integration was then used to develop an approximate function which has an average error of 0.63% and a maximum error of 1.05%, relative to the numerical integration. Both of these errors are normalized by the maximum value of 1 for Eqn.(3.45). The maximum error occurs near a minimum slope so its' effects are minimized because an error in the independent variable does not lead to a larger error in the approximated variable. It is believed that a maximum error of 1.05% is tolerable when the savings in computation time are considered; because a substantial savings in computational time has been realized with the introduction of an error two orders magnitude smaller than the variable being approximated.

The approximate function developed for the austenite to martensite phase change is the following:

$$\tilde{\xi}_A(T) = \frac{1}{2}\left(1 + \tanh\left(C\left(T - \left(\frac{M_s^o + M_f^o}{2}\right)\right)\right)\right) \tag{3.50}$$

where $\tilde{\xi}$ denotes the phase when formulated with the approximate function, the subscript on $\tilde{\xi}$ refers to the phase. Similar to ξ, the range of $\tilde{\xi}$ is $0 \leq \tilde{\xi} \leq 1$.

The *tanh* function was prescribed to match the shape of the numerical integration. The scalar constant '$C = 0.56$' was found using an iterative search with the program MATLAB. This quantity is a shape factor which controls the spread of the tanh function in the direction of the independent

variable, T. This value was chosen to minimize the average and maximum error relative to the numerical integration. The term $((M_s^o + M_f^o)/2)$ centers the tanh function at the average of M_s^o and M_f^o, translating the function along the independent variable axis.

Figure 3.2 shows both the numerical integration and the approximate function, Eqn.(3.50), for the austenite to martensite transformation.

A second equation is needed for the state of the material when it transforms from austenite to martensite. The only difference between Eqn.(3.50) and the approximate function for the martensite to austenite transformation is the start and finish temperatures. A_s^o replaces M_s^o, and A_f^o replaces M_f^o. The equation for the martensite to austenite transformation is as follows:

$$\tilde{\xi}_M(T) = \frac{1}{2}\left(1 + \tanh\left(0.56\left(T - \left(\frac{A_s^o + A_f^o}{2}\right)\right)\right)\right) \tag{3.51}$$

In Eqn.'s (3.50) and (3.51) T is the temperature at which the state variable, $\tilde{\xi}(T)$, is being determined.

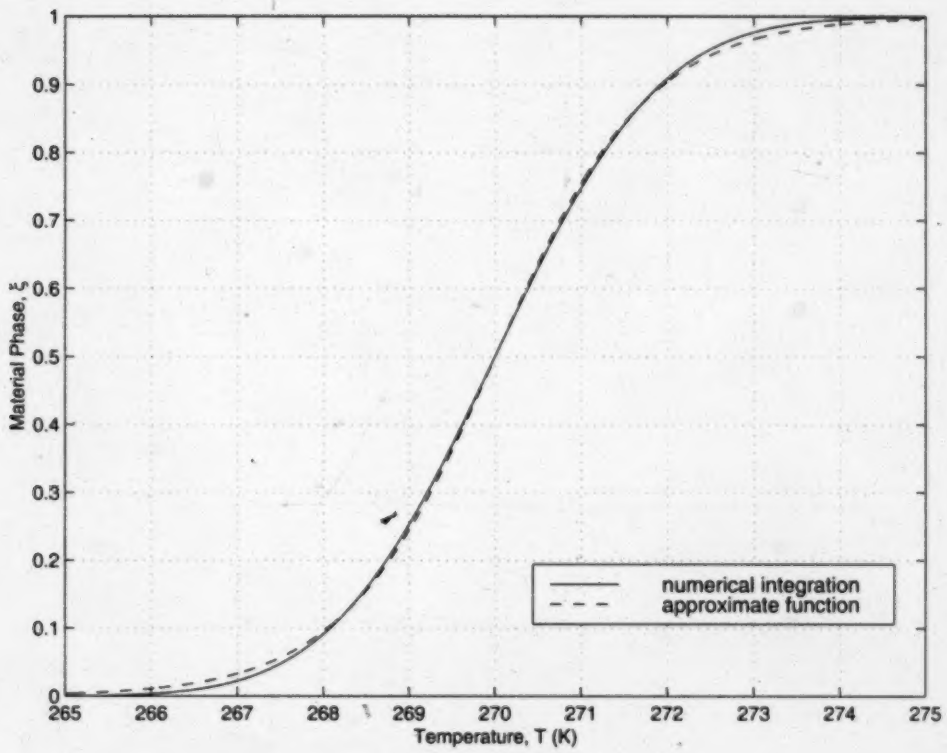

Figure 3.2: Comparison of Approximate Function to Numerical Integration

3.3.4 Numerical Modeling of Thermal Conductivity

The thermal conductivity of the SMA varies by an order of magnitude between the two material phases. This variation in k will be incorporated in the numerical model since it will have a affect on the temperature field in the solid. An assumption will be made that the thermal conductivity of the SMA is a linear function of ξ of the following form [1]:

$$k(\xi) = k_M + \xi(k_A - k_M) \tag{3.52}$$

where the subscripts refer to the phase, $k_M = 1.8\ W/mK$, $k_A = 18\ W/mK$ [1], and again $0 \leq \xi \leq 1$.

Eqn.'s (3.45) - (3.48) for the martensitic volume fraction, $\xi(T)$, are applied to Eqn.(3.52). This makes k a function of temperature, shown below for austenite and martensite respectively:

$$k_{AM}(T) = k_M + \left(1 + \left[\int_{M_s^o}^{T} \frac{\exp\left[-\frac{1}{2} \left[\frac{T - \frac{1}{2}(M_s^o + M_f^o)}{S} \right]^2 \right]}{S\sqrt{2\pi}} d\tilde{T} \right] \right) (k_A - k_M) \tag{3.53}$$

$$k_{MA}(T) = k_M + \left[\int_{A_s^o}^{T} \frac{\exp\left[-\frac{1}{2} \left[\frac{T - \frac{1}{2}(A_s^o + A_f^o)}{S} \right]^2 \right]}{S\sqrt{2\pi}} d\tilde{T} \right] (k_A - k_M) \tag{3.54}$$

where the subscripts on $k(T)$ refer to the starting phase, first subscript, and the finish phase, second subscript.

Since the approximate functions, Eqn.'s (3.50) and (3.51), have been used in the solution for this work, the thermal conductivity is written for martensite and austenite as follows:

$$\tilde{k}_{MA}(T) = k_M + \frac{1}{2} \left(1 + \tanh\left(0.56 \left(T - \left(\frac{A_s^o + A_f^o}{2} \right) \right) \right) \right) (k_A - k_M) \tag{3.55}$$

$$\tilde{k}_{AM}(T) = k_M + \frac{1}{2}\left(1 + \tanh\left(0.56\left(T - \left(\frac{M_s^o + M_f^o}{2}\right)\right)\right)\right)(k_A - k_M) \quad (3.56)$$

where the subscripts on $\tilde{k}$ refer to the starting phase, first subscript, and finish phase, second subscript.

A plot of $\tilde{k}(T)$ using the approximate function is shown in Figure 3.3. With this plot it is important to note that the properties are determined from the curve corresponding to which ever phase the material is in.

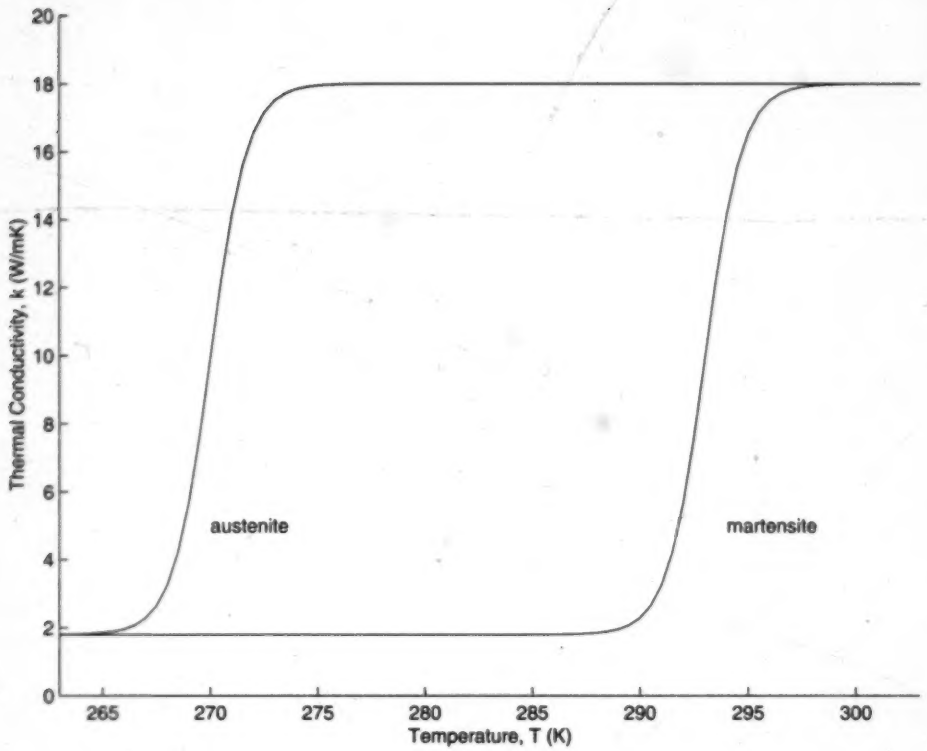

Figure 3.3: Thermal Conductivity for Both Material Phases

3.3.5 Latent Energy of Transformation

When the SMA undergoes a phase change the crystal structure of the material is rearranged and energy is either absorbed or released. Over the transformation temperature range the latent energy of the phase change is significantly greater than the sensible energy of the temperature change. For the material used in this work, the latent energy of phase change is seven times larger than the sensible heat over the transformation temperature range. Therefore, to completely describe the internal energy in the smart material it is necessary to incorporate a latent energy term:

$$e(T) = \rho(c_p T + H\xi(T)) \tag{3.57}$$

where c_p is the specific heat capacity of the material, and H is the latent heat of transformation. $\rho c_p = 2.12(10^{-3})\ J/mm^3K$ and $\rho H = 0.148\ J/mm^3$. These values are valid only for the sample of nitinol being investigated for the current research.

The $\rho H\xi(T)$ term models the latent heat of transformation for the phase change. Similar to the method for the thermal conductivity, Eqn.'s (3.45) - (3.48) are applied to the phase term, $\xi(t)$. The result is shown below:

$$e_A(T) = \rho(c_p T + H\left(1 + \left[\int_{M_s^o}^{T} \frac{\exp\left[-\frac{1}{2}\left[\frac{T-\frac{1}{2}(M_s^o+M_f^o)}{S}\right]^2\right]}{S\sqrt{2\pi}}\, d\tilde{T}\right]\right)) \tag{3.58}$$

$$e_M(T) = \rho(c_p T + H\left[\int_{A_s^o}^{T} \frac{\exp\left[-\frac{1}{2}\left[\frac{T-\frac{1}{2}(A_s^o+A_f^o)}{S}\right]^2\right]}{S\sqrt{2\pi}}\, d\tilde{T}\right]) \tag{3.59}$$

Again there are two functions for the internal energy dependent upon the material's state.

Also as before the approximate functions, Eqn.'s (3.50) and (3.51), will be employed. When written with the approximate function, the internal energy $\tilde{e}$, for the martensite and austenite phases are as follows, respectively:

$$\tilde{e}_A(T) = \rho \left[c_p T + H \frac{1}{2} \left(1 + \tanh \left(0.56 \left(T - \left(\frac{A_s^o + A_f^o}{2} \right) \right) \right) \right) \right] \quad (3.60)$$

$$\tilde{e}_M(T) = \rho \left[c_p T + H \frac{1}{2} \left(1 + \tanh \left(0.56 \left(T - \left(\frac{M_s^o + M_f^o}{2} \right) \right) \right) \right) \right] \quad (3.61)$$

A plot of the specific internal energy for both material phases as a function of temperature can be seen in Figure 3.4.

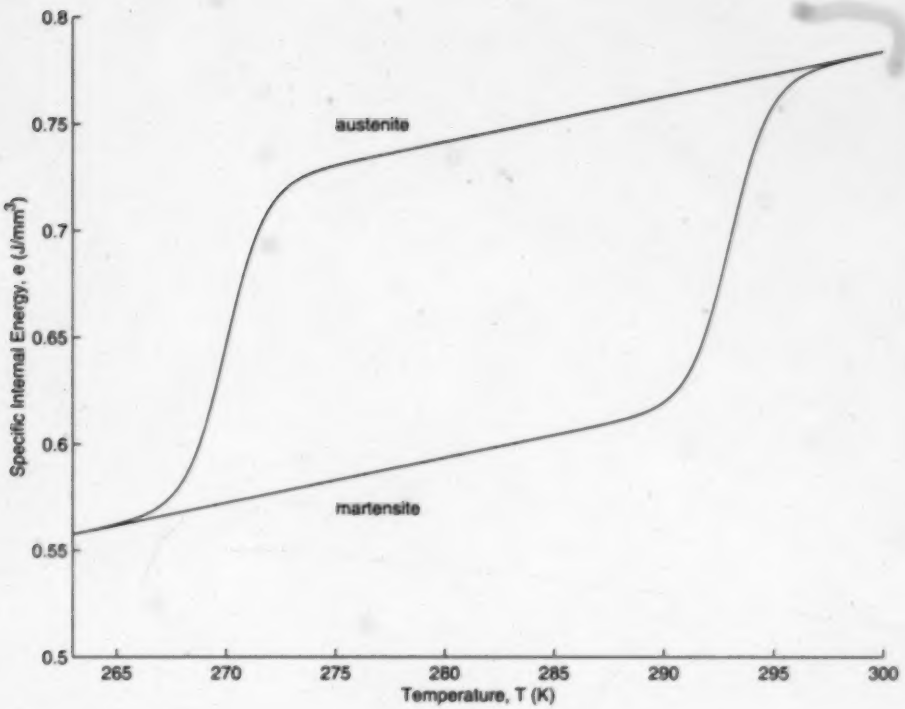

Figure 3.4: Specific Internal Energy for Both Material Phases

3.3.6 Governing Equations in Solid Region

Since grid cell averaged properties are being used in the phase model for the smart material, the need to track travelling phase boundaries in the solid has been removed. The phase of the material transitions smoothly between martensite and austenite, there is no discontinuous boundary between the two phases. This model does not have any velocities as independent variables. Therefore it is not necessary to solve Eqn.'s (3.4) and (3.5) for the velocity field in this region of the domain. This also means the material derivative in Eqn.(3.27) becomes a time derivative since the velocities are nonexistent:

$$\frac{De}{Dt} = \frac{\partial e}{\partial t} + u\frac{\partial e}{\partial x} + v\frac{\partial e}{\partial y} = \frac{\partial e}{\partial t} \quad (u, v = 0) \tag{3.62}$$

In order to capture the effects of the phase change on the material properties, there will be variable thermal conductivity for the solid when solving Eqn.(3.27). In addition, a term to model the latent energy of the phase change, $\rho H \xi(T)$, has been added. The conservation equation to be solved in the solid region of the domain is the following:

$$\frac{\partial(\rho c_p T + \rho H \xi(T))}{\partial t} = \frac{\partial}{\partial x}\left(k\frac{\partial(T)}{\partial x}\right) + \frac{\partial}{\partial y}\left(k\frac{\partial(T)}{\partial y}\right) \tag{3.63}$$

where k is defined in Eqn.'s (3.55) and (3.56), and $\xi(T)$ is defined in Eqn.'s (3.50) and (3.51).

3.4 Flow Decomposition

This work has been based on existing research which was completed to study the effects of starting vortices on the vortex roll-up on a turbine blade [43].

The original research was isothermal and did not consider the interior of the blade as part of the solution domain.

A complex-lamellar decomposition of the flow field is used in the solution of the velocity field in the original research. This decomposition allows for shear velocities to be supplied as input. This feature was not used in the current work, but the potential exists to take advantage of this capability. The decomposition used for the current investigation involved separating the flow into an inviscid potential and a viscous correction.

$$\overline{v} = U_\infty + \nabla\phi + \nabla \times \psi \tag{3.64}$$

The ϕ potential is an irrotational potential, ψ is the viscous correction stream function.

With the velocity written in this manner, the continuity equation for the fluid becomes the following:

$$\nabla^2\phi = 0 \tag{3.65}$$

3.5 Coordinate Transformation

Before the governing equations are solved, the coordinate system is transformed from the physical space, (x, y), to the computational space, (ξ, η), where $x = x(\xi, \eta)$ and $y = y(\xi, \eta)$. The (x, y) coordinates are mapped onto the (ξ, η) coordinates in a simply connected manner [35]. That is, each point in the physical space is represented by only one point in the computational space.

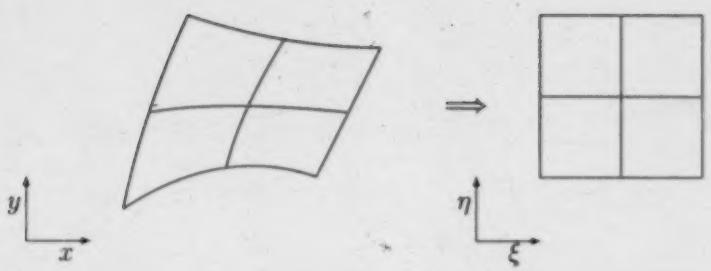

Figure 3.5: Transformation from (x, y) to (ξ, η) Coordinate System

The computational domain is constructed such that $\Delta\xi = \Delta\eta = 1$. The computational domain is a generalized orthogonal curvilinear coordinate system.

To demonstrate the effect this transformation has on the governing equations, the coordinate transformation will be done on the following equation:

$$\frac{\partial w}{\partial t} + u\frac{\partial w}{\partial x} + v\frac{\partial w}{\partial y} = \nu\frac{\partial^2 w}{\partial x^2} + \nu\frac{\partial^2 w}{\partial y^2} \tag{3.66}$$

where the first order differential terms are convection quantities and the second order differentials are conduction quantities.

This is a two dimensional convection/diffusion equation, representing Eqn.'s (3.38) and (3.43). Eqn.(3.63) would be transformed in a similar manner, without the convection terms present.

First Eqn.(3.66) is written in conservative form by making use of Eqn.(3.18). The result is as follows:

$$\frac{\partial w}{\partial t} + \frac{\partial (uw)}{\partial x} + \frac{\partial (vw)}{\partial y} = \nu\frac{\partial^2 w}{\partial x^2} + \nu\frac{\partial^2 w}{\partial y^2} \tag{3.67}$$

By invoking the continuity equation, Eqn.(3.18) , the convection speeds u and v can be moved to the inside of the spatial derivatives.

With (x, y) both functions of (ξ, η), derivatives in (x, y) must then be expanded using the chain rule:

$$\frac{\partial}{\partial x} = \frac{\partial \xi}{\partial x}\frac{\partial}{\partial \xi} + \frac{\partial \eta}{\partial x}\frac{\partial}{\partial \eta} \quad \text{and:} \quad \frac{\partial}{\partial y} = \frac{\partial \xi}{\partial y}\frac{\partial}{\partial \xi} + \frac{\partial \eta}{\partial y}\frac{\partial}{\partial \eta} \tag{3.68}$$

Derivatives of (ξ, η) with respect to (x, y) can be rewritten making use of the Jacobian of the transformation, where subscripts refer to partial derivatives:

$$J = \begin{bmatrix} x_\xi & x_\eta \\ y_\xi & y_\eta \end{bmatrix} \tag{3.69}$$

with:

$$J^{-1} = \begin{bmatrix} \xi_x & \xi_y \\ \eta_x & \eta_y \end{bmatrix} = \frac{1}{\|J\|}\begin{bmatrix} y_\eta & -x_\eta \\ -y_\xi & x_\xi \end{bmatrix} \tag{3.70}$$

and the determinant of the Jacobian is:

$$\|J\| = x_\xi y_\eta - x_\eta y_\xi \tag{3.71}$$

The partial derivatives are now written as:

$$\frac{\partial}{\partial x} = \frac{1}{\|J\|}\left(y_\eta \frac{\partial}{\partial \xi} - y_\xi \frac{\partial}{\partial \eta}\right) \quad \text{and:} \quad \frac{\partial}{\partial y} = \frac{1}{\|J\|}\left(-x_\eta \frac{\partial}{\partial \xi} + x_\xi \frac{\partial}{\partial \eta}\right) \tag{3.72}$$

Applying Eqn.(3.72) to Eqn.(3.66) can be shown to result in the following transformed equation:

$$\frac{\partial(\|J\|w)}{\partial t} + \frac{\partial(\|J\|Uw)}{\partial \xi} + \frac{\partial(\|J\|Vw)}{\partial \eta} = \frac{\partial}{\partial \xi}\left(a_1 \frac{\partial w}{\partial \xi} + a_2 \frac{\partial w}{\partial \eta}\right) + \frac{\partial}{\partial \eta}\left(b_1 \frac{\partial w}{\partial \xi} + b_2 \frac{\partial w}{\partial \eta}\right) \tag{3.73}$$

where U and V are the contravariant velocities and are defined in the following manner:

$$\begin{bmatrix} U \\ V \end{bmatrix} = J^{-1} \begin{bmatrix} u \\ v \end{bmatrix} \tag{3.74}$$

and;

$$\begin{aligned} a_1 &= \frac{y_\eta^2 + x_\eta^2}{\|J\|} \\ a_2 &= \frac{-y_\xi y_\eta - x_\xi x_\eta}{\|J\|} \\ b_1 &= \frac{x_\xi^2 + y_\xi^2}{\|J\|} \\ b_2 &= \frac{-y_\xi y_\eta - x_\xi x_\eta}{\|J\|} \end{aligned} \tag{3.75}$$

Eqn.(3.75) are known as the transformation geometrics, they must be calculated numerically for each cell.

The transformation requires that the Jacobian terms be constructed numerically so that the following is true:

$$\frac{\partial^2 y}{\partial \xi \partial \eta} = \frac{\partial^2 y}{\partial \eta \partial \xi} \quad \text{and:} \quad \frac{\partial^2 x}{\partial \xi \partial \eta} = \frac{\partial^2 x}{\partial \eta \partial \xi} \tag{3.76}$$

This is enforced through the application of the finite volume formulation.

3.6 Dimensional Analysis

The final modification to be made to the governing equations is to put them into dimensionless form. The first step is to select reference values of velocity, length and temperature. The axial length of the solid, L, will be used as the reference length. The freestream velocity of the fluid, U_∞, will be used as the

reference velocity. The initial temperature of the solid, $T^{(solid)}_{(initial)}$, will be used as the reference temperature value. Using the reference values the variables x, y, T, t, u, v and ω are nondimensionalized as follows:

$$\begin{aligned} x^* &= \frac{x}{L},\ y^* = \frac{y}{L},\ t^* = \frac{tU_\infty}{L},\ T^* = \frac{T}{T^{(solid)}_{(initial)}}, \\ u^* &= \frac{u}{U_\infty},\ v^* = \frac{v}{U_\infty},\ \omega^* = \frac{\omega L}{U_\infty} \end{aligned} \tag{3.77}$$

where the * indicates a dimensionless quantity.

In this format, one dimensionless unit of time refers to the time needed for a particle in the free stream to travel a distance equivalent to the axial length of the solid.

Using the dimensionless variables from Eqn.(3.77) it is possible to nondimensionalize the vorticity transport equation in the fluid, Eqn.(3.38), and the energy equation in the fluid, Eqn.(3.43). The energy equation in the solid, Eqn.(3.63), requires two additional variables, e and k, to be nondimensionalized. This is done as follows:

$$k^* = \frac{k(T)}{k_M},\ e^* = \frac{e}{\rho c_p T^{(solid)}_{(initial)}} \tag{3.78}$$

where the martensitic thermal conductivity value, k_M, has been used to nondimensionalize the temperature dependent thermal conductivity. Again the dimensionless quantities are represented with a superscript *.

The nondimensionalization of the vorticity transport equation proceeds as follows; begin with the equation in dimensional form:

$$\frac{\partial \omega}{\partial t} + u\frac{\partial \omega}{\partial x} + v\frac{\partial \omega}{\partial y} = \beta g \frac{\partial T}{\partial x} + \frac{\mu}{\rho}\left(\frac{\partial^2 \omega}{\partial x^2} + \frac{\partial^2 \omega}{\partial y^2}\right) \tag{3.79}$$

Substituting the values for the dimensionless variables from Eqn.(3.77) and simplifying results in the following:

$$\frac{\partial \omega^*}{\partial t^*}+u^*\frac{\partial \omega^*}{\partial x^*}+v^*\frac{\partial \omega^*}{\partial y^*}=\frac{\beta g(T_1-T_0)L}{U_\infty^2}\frac{\partial T^*}{\partial x^*}+\frac{\mu}{\rho U_\infty L}\left(\frac{\partial^2 \omega^*}{\partial x^{*2}}+\frac{\partial^2 \omega^*}{\partial y^{*2}}\right) \quad (3.80)$$

The Reynolds number, Prantl number and Grashof number are defined as follows:

$$\begin{aligned} Re &= \left[\frac{\rho_o U_\infty L}{\mu}\right] \\ Pr &= \left[\frac{c_p \mu}{k}\right] \\ Gr &= \left[\frac{g\beta T_{(initial)}^{(solid)} L^3 \rho_o^2}{\mu^2}\right] \end{aligned} \quad (3.81)$$

Since these parameters are for the fluid flow, all properties in Eqn.(3.81) are for the fluid in the freestream. This means that the values for ρ, μ, c_p, k and β will be chosen based on the inlet conditions.

Substituting the Reynolds number and Grashof number into Eqn.(3.80) results in the dimensionless form of the vorticity transport equation:

$$\frac{D\omega^*}{Dt^*}=\left[\frac{Gr}{Re^2}\right]\frac{\partial T^*}{\partial x^*}+\left[\frac{1}{Re}\right]\nabla^{*2}\omega^* \quad (3.82)$$

The process for the energy equation in the fluid is the same. Start with the dimensional form, substitute for the dimensionless variables and simplify. Making use of the Prantl number and Reynolds number, the result is as follows:

$$\frac{DT^*}{Dt^*}=\left[\frac{1}{RePr}\right]\nabla^{*2}T^* \quad (3.83)$$

To nondimensionalize the energy equation in the solid begin with the following form of the equation:

$$\frac{\partial e}{\partial t}=\frac{\partial}{\partial x}\left(k(T)\frac{\partial T}{\partial x}\right)+\frac{\partial}{\partial y}\left(k(T)\frac{\partial T}{\partial y}\right) \quad (3.84)$$

Substitute the dimensionless variables from Eqn.'s (3.77) and (3.78) then simplify to get the following:

$$\frac{\partial e^*}{\partial t^*} = \frac{1}{\rho c_p U_\infty L}\frac{\partial}{\partial x^*}\left(k^* k_M \frac{\partial T^*}{\partial x^*}\right) + \frac{1}{\rho c_p U_\infty L}\frac{\partial}{\partial y^*}\left(k^* k_M \frac{\partial T^*}{\partial y^*}\right) \tag{3.85}$$

Since k_M is constant it can moved to the exterior of the spatial derivatives:

$$\frac{\partial e^*}{\partial t^*} = \frac{k_M}{\rho c_p U_\infty L}\frac{\partial}{\partial x^*}\left(k^* \frac{\partial T^*}{\partial x^*}\right) + \frac{k_M}{\rho c_p U_\infty L}\frac{\partial}{\partial y^*}\left(k^* \frac{\partial T^*}{\partial y^*}\right) \tag{3.86}$$

The Peclet number is defined as follows:

$$Pe = \left[\frac{\rho c_p U_\infty L}{k_M}\right] \tag{3.87}$$

Note that the Peclet number has been defined based on the martensitic thermal conductivity, k_M.

Substituting for the Peclet number, the energy equation to be solved in the solid region of the domain in nondimensional form is as follows:

$$\frac{\partial e^*}{\partial t^*} = \left[\frac{1}{Pe}\right]\left(\frac{\partial}{\partial x^*}\left(k^* \frac{\partial T^*}{\partial x^*}\right) + \frac{\partial}{\partial y^*}\left(k^* \frac{\partial T^*}{\partial y^*}\right)\right) \tag{3.88}$$

CHAPTER 4

NUMERICAL FORMULATION

4.1 Solution Sequence

To unify the ideas of the previous chapter, the sequence of steps needed to solve the various equations will now be explained.

1: An initial condition for the flow is developed by solving the inviscid potential equation:

$$\frac{\partial^2 \phi}{\partial x^2} + \frac{\partial^2 \phi}{\partial y^2} = 0 \tag{4.1}$$

This equation only needs to be solved once since the velocity decomposition, Eqn.(3.64), satisfies the continuity equation, Eqn.(3.18), at all times. Eqn.(4.1) is solved using an approximate LU factorization scheme. The convergence to steady state is accelerated by the application of multigrid.

2: The next item in the sequence is to begin the time stepping. This is done by solving the energy equation in the solid, the viscous vorticity transport

equation and the energy equation in the fluid at the same time. This entails solving Eqn.'s (3.82), (3.83) and (3.88).

The time stepping of Eqn.'s (3.82) and (3.83) is accomplished through a two stage, second order accurate, explicit Runge Kutta technique. Linear interpolation will be used to construct second order spatial derivatives. A nonoscillatory quadratic interpolation will be used to construct first order spatial derivatives.

Time advancement of Eqn.(3.88) is achieved through a semi-implicit, second order accurate single step technique. Jameson's four level multistage scheme is used to iterate the semi-implicit formulation to convergence at each time step. Again linear interpolation will be used to construct the second order derivatives.

3: Eqn.(3.88) solves for the energy and not the temperature in the solid. Therefore the following must be solved for the temperature of the solid:

$$e = \rho(c_p T + H\xi(T)) \qquad (4.2)$$

Eqn.(4.2) is a decomposition of the internal energy in the smart material into two components. The first is a sensible component, $c_p T$, and the second component represents the phase change latent energy, $H\xi(T)$. This second term represents the increased energy requirements as the material undergoes a solid state phase change. T cannot be directly solved from Eqn.(4.2) because the formulation of $\xi(T)$ is nonlinear. Therefore a Newton Iteration will be used to converge to a solution for T corresponding to e.

4: In order to construct the viscous velocity field it is necessary to obtain the viscous correction stream function. The relation between the stream function and the vorticity is the following:

$$\frac{\partial^2 \psi}{\partial x^2} + \frac{\partial^2 \psi}{\partial y^2} = -\omega \tag{4.3}$$

Eqn.(4.3) represents the viscous *correction* to the inviscid potential flow obtained from Eqn.(4.1). Therefore, only regions of the flow field experiencing viscous effects will have nonzero values for the viscous correction stream function. The viscous effects will mainly be present in the boundary layer along the solid surface and the wake behind the shape memory alloy. This will increase the numerical efficiency of the solution process since large portions of the domain will have no viscous correction to the potential flow.

Eqn.(4.3) will be solved using an approximate LU factorization scheme. Again multigrid is applied to accelerate the convergence to steady state. This is the same technique used to solve the potential equation, Eqn.(4.1). An explanation of the technique will be given for Eqn.(4.3), with the differences in the solution process for Eqn.(4.1) being pointed out.

This sequence is one that will develop a time accurate solution of the independent variables that will progress forward in time. To maintain time accuracy the above three steps of the solution sequence, 2 - 4, must be completed for each time increment.

4.2 Convergence of Viscous Stream Function

At each time step the viscous correction stream function corresponding to the new vorticity must be found. The new stream function is used to construct the velocity at the new time step. The stream function is obtained from vorticity as follows:

$$\frac{\partial^2 \psi}{\partial x^2} + \frac{\partial^2 \psi}{\partial y^2} = -\omega \tag{4.4}$$

The method used to solve this equation is an approximate LU factorization scheme. The convergence of the solution is accelerated by applying multigrid.

An approximate LU factorization is also used for the first solution of the potential field for the flow, Eqn. (4.1). An explanation of the solution scheme will be given for the viscous stream function equation. The process would be the same for the potential equation, the only difference being there is no source term on the right hand side of Eqn.(4.1).

4.2.1 Approximate LU Factorization

The first step is to rewrite the equation as a time dependent partial differential equation.

$$\frac{\partial \psi}{\partial \tilde{t}} = \frac{\partial^2 \psi}{\partial x^2} + \frac{\partial^2 \psi}{\partial y^2} + \omega = 0 \tag{4.5}$$

The time variable, $\tilde{t}$, is a pseudo time variable that differs from the global time variable. Solving Eqn.(4.5) means driving the pseudo time derivative to zero to produce a steady state solution.

Written with an implicit parameter, λ, this equation becomes:

$$\frac{\partial \psi}{\partial \tilde{t}} = \left((1-\lambda) \left[\frac{\partial^2 \psi}{\partial x^2} + \frac{\partial^2 \psi}{\partial y^2} + \omega \right]^k + \lambda \left[\frac{\partial^2 \psi}{\partial x^2} + \frac{\partial^2 \psi}{\partial y^2} + \omega \right]^{k+1} \right) \tag{4.6}$$

When $\lambda = 0$ the equation is explicit, when $\lambda = 1$ the equation is fully implicit. The time derivative and counter, k, refer to the sequential steps of the pseudo time integration.

Approximating the time derivative as finite changes, and converting the values at iteration $k+1$ to iteration k, the above can be shown to reduce to:

$$\left[I - \Delta\tilde{t}\lambda \left(\frac{\partial^2}{\partial x^2} + \frac{\partial^2}{\partial y^2} \right) \right] \Delta\psi^k = \Delta\tilde{t} \left[\frac{\partial^2 \psi}{\partial x^2} + \frac{\partial^2 \psi}{\partial y^2} + \omega \right] \tag{4.7}$$

The term on the right hand side in square brackets is the residual, explained in Section 4.5. $\Delta\tilde{t}$ is the time step of the pseudo integration. $\Delta\psi^k$ is the change in ψ with each pseudo time integration.

The approximate factorization is applied to the term on the left hand side in square brackets [44].

$$\left[I - \Delta\tilde{t}\lambda(\delta_x^+ + \delta_y^+) \right] \left[I + \Delta\tilde{t}\lambda(\delta_x^- + \delta_y^-) \right] \Delta\psi^k = r\Delta\tilde{t}\ \mathrm{Res}^k \tag{4.8}$$

where r is a relaxation factor.

This is solved in two steps:

$$\begin{aligned} &(1) \quad \left[I + \Delta\tilde{t}\lambda(\delta_x^- + \delta_y^-) \right] \Delta\psi' = r\Delta\tilde{t}\ \mathrm{Res}^k \\ &(2) \quad \left[I - \Delta\tilde{t}\lambda(\delta_x^+ + \delta_y^+) \right] \Delta\psi^k = \Delta\psi' \end{aligned} \tag{4.9}$$

The unknown in step (1) is $\Delta\psi'$. It is solved for by directly inverting the lower diagonal matrix constructed from the term in square brackets in step (1) of Eqn.(4.10). The unknown in step (2) is the change in the stream function, $\Delta\psi^k$. It is solved for by directly inverting the upper diagonal matrix

constructed from the term in square brackets in step two of Eqn.(4.10). The implicit parameter and relaxation factor are both given values of 1.

The technique described above is also used to solve the potential equation, Eqn.(4.1). For this equation the implicit parameter is 0.5 and the relaxation factor is 1.

4.2.2 Multigrid Convergence Acceleration

Eqn.(4.3) is a steady state elliptic equation which must be iterated to convergence for each time step. Steady state equations have their solutions governed by the boundary conditions. The quicker that information on the boundaries can influence the interior of the domain the quicker the solution will converge. In addition, the approximate LU factorization scheme being used can be shown to have excellent high frequency error damping performance [42]. Both of these factors make multigrid useful for this problem.

A multigrid cycle begins by calculating a solution correction on the fine grid and the new solution after this correction is applied [41]. This is shown below in operator form.

$$\mathrm{LU}_h \Delta w_h = -\Delta t \mathrm{Res}_h \tag{4.10}$$

$$w_h^{k+1} = w_h^k + \Delta w_h^k \tag{4.11}$$

where L and U are lower and upper operators respectively, Res_h is the residual on the h grid level and Δw_h is the correction to w on the h grid level.

This new solution is passed down to the next coarsest grid by an area weighted accumulation method, denoted by the operator T.

$$w_{h-1}^t = T_{h-1}^h w_h \tag{4.12}$$

The residual is passed down to the next coarsest grid by a direct summation, denoted by the operator $\tilde{T}$

$$\mathrm{Res}^c_{h-1} = \tilde{T}^h_{h-1}\mathrm{Res}_h \tag{4.13}$$

A new coarse grid residual is developed at this grid level.

$$\begin{aligned} \mathrm{Res}^t_{h-1} &= \mathrm{Res}(w^t_{h-1})_{h-1} \\ &= \mathrm{Res}(T^h_{h-1}w_h)_{h-1} \end{aligned} \tag{4.14}$$

The difference between the calculated residual on the coarse grid and the residual passed down from the fine grid is calculated. It is known as the forcing function, FF.

$$\begin{aligned} \mathrm{FF}_{h-1} &= \mathrm{Res}^c_{h-1} - \mathrm{Res}^t_{h-1} \\ &= \tilde{T}^h_{h-1}\mathrm{Res}_h - \mathrm{Res}(T^h_{h-1}w_h)_{h-1} \end{aligned} \tag{4.15}$$

The new solution residual on the coarse grid is the sum of the residual calculated with the solution at the coarse grid, and the forcing function.

$$\begin{aligned} \mathrm{LU}_{h-1}\Delta w_{h-1} &= -\Delta t(\mathrm{Res}_{h-1} + \mathrm{FF}_{h-1}) \\ &= -\Delta t(\mathrm{Res}_{h-1} + \tilde{T}^h_{h-1}\mathrm{Res}_h - \mathrm{Res}(T^h_{h-1}w_h)_{h-1}) \end{aligned} \tag{4.16}$$

This manner of calculating on the present grid and passing information to coarser grids continues until the lowest grid level is reached.

At this point the process of passing the coarse grid correction values upwards to the finer grids begins. At each up-pass the difference between the fine grid solution and the interpolated coarse grid solution is applied to the fine grid.

$$w'_h = w_h + I^{h-1}_h(w'_{h-1} - T^h_{h-1}w_h) \tag{4.17}$$

Passing the solution corrections up to the finer meshes continues until the uppermost mesh is reached.

The operators T and I are transfer and interpolation operators used to pass information down and up, respectively, between the grid levels. They are not inverses of each other.

A five level W cycle is the multigrid scheme used for this work. At each time step the maximum residual is reduced to the order of $O(10^{-9})$ before the equation is considered to be converged. Convergence of the viscous stream function equation is normally achieved within no more than 10 multigrid cycles. One complete multigrid cycle is shown in Figure 4.1.

Figure 4.1: Schematic of Six Level 'W' Cycle used in Multigrid Scheme

4.3 Model Equation

The following sections will describe the numerical techniques used to solve the governing conservation equations. To demonstrate the numerical techniques a model equation will be used which represents both the viscous momentum

equation, and the energy equation. This model equation has both the convection and conduction terms present. The model equation is shown below.

$$\frac{\partial w}{\partial t} + c\frac{\partial w}{\partial x} = \nu\frac{\partial^2 w}{\partial x^2} \tag{4.18}$$

where the first order derivative term is a convection quantity and the second order differential term is a conduction (diffusion) quantity.

Note that the model equation has been reduced from two dimensions to one, and the velocity has been assumed to be constant along with all properties.

4.4 Time Integration of Equations in Fluid Region

The numerical technique used to approximate the time integration in Eqn.'s (3.82) and (3.83) is a two stage, explicit, time accurate, Runge Kutta method. An algebraic representation of one complete time step for this technique is shown below:

$$\begin{aligned} w^{(0)} &= w^{[N]} \\ w^{(1)} &= w^{(0)} + \alpha_1 \Delta t \ \mathrm{Res}(w^{(0)}) \\ w^{(2)} &= w^{(0)} + \alpha_2 \Delta t \ \mathrm{Res}(w^{(1)}) \\ w^{[N+1]} &= w^{(2)} \end{aligned} \tag{4.19}$$

The α_l terms are Runge Kutta stage coefficients. They affect both the numerical stability and time accuracy of the solution. The Δt term is the time step used to time advance Eqn.'s (3.82),(3.83) and (3.88). The superscript terms in round brackets refer to the Runge Kutta stage, the superscript terms in square brackets refer to the time step.

An explanation of how to construct the $\text{Res}(w^{(l)})$ terms, known as residuals, will be described in Section 4.5. They are a method of calculating the spatial derivatives on a grid cell:

$$\text{Res}(w^{(l)}) = \nu \frac{\partial^2 w^{(l)}}{\partial x^2} - c \frac{\partial w^{(l)}}{\partial x} \tag{4.20}$$

By rewriting the original differential equation, Eqn.(4.18), it is possible to recover the Taylor series expansion for the time derivative. This is done by making it resemble Eqn.(4.20), putting the result into Eqn.(4.19) and simplifying:

$$w^{[N+1]} = w^{[N]} + \alpha_1 \, \Delta t \, \frac{\partial w^{[N]}}{\partial t} + \alpha_2 \, (\Delta t)^2 \, \frac{\partial^2 w^{[N]}}{\partial t^2} \tag{4.21}$$

Eqn.(4.21) has been written to show the result for a two stage Runge Kutta. If desired, additional stages can be added to the Runge Kutta time integration to increase the accuracy level or aid in stability. The values of α_l are selected to satisfy time accuracy and guarantee numerical stability. For this work $\alpha_1 = 0.5$ and $\alpha_2 = 1.0$ to ensure a solution which is second order accurate in time, $O(\Delta t^2)$, and numerically stable.

4.5 Spatial Integration Scheme

This section will deal with the construction of the residuals from Eqn.(4.19). As was previously stated, the residuals are a method of calculating the spatial derivatives, shown in Eqn.(4.20). For this work they are solved for using a finite volume method.

To illustrate the technique consider the following example equation written in the computational coordinates:

$$\text{Res} = \frac{\partial}{\partial \xi}(A) + \frac{\partial}{\partial \eta}(B) \tag{4.22}$$

where A and B are known as fluxes.

The A and B fluxes can be comprised of convection terms, conduction terms, material properties, transformation geometrics or any combination of these. The key is that transformed equations can be rewritten to resemble the conservative form of Eqn.(4.22).

The differential in the ξ direction in Eqn.(4.22) represents change across the cell of the A flux in the ξ direction. Similarly, the differential in the η direction in Eqn.(4.22) represents change across the cell of the B flux in the η direction. To calculate the change of A across the cell, the value of A on the right and left cell faces is determined. The difference between these two amounts represents the ξ differential in Eqn.(4.22), since $\Delta\xi = 1$. To construct the η differential values of B at the top and bottom cell faces are calculated and differenced from each other. The residual is the result of constructing these differences over the cell:

$$\text{Res}_{i,j} = (\text{A}_{i+\frac{1}{2},j} - \text{A}_{i-\frac{1}{2},j}) + (\text{B}_{i,j+\frac{1}{2}} - \text{B}_{i,j-\frac{1}{2}}) \tag{4.23}$$

The difficulty lies in obtaining values for the possible components of the A and B terms on the cell faces. The independent variables and material properties are assumed to reside at the cell center, and the geometric terms reside along the cell faces. For the diffusion term in the model equation linear interpolation is used to construct values at the cell face. For the convection

term in the model equation the UNO2 interpolation method is used to obtain values at the faces. UNO2 will be explained in Section 4.6.

The viscous correction stream function, Eqn.(4.3) and potential equation, Eqn.(4.1), are elliptic equations. As such they have smooth solutions where information is transmitted equally in all directions. Therefore in the construction of the residuals for elliptic equations, it is acceptable to use a linear interpolation of the independent variables at the cell faces.

4.6 Interpolation of Convection Term

The viscous stream function, Eqn.(4.3), and potential equation, Eqn.(4.1), are elliptic equations. Conversely, the vorticity transport equation, Eqn.(3.82), and energy equation in the fluid, Eqn.(3.83) are hyperbolic. Hyperbolic equations contain convection terms that do not have smooth solutions, and information is not transferred equally in all directions. There is a convection velocity which governs the direction in which information travels. As a result linear interpolation is not acceptable for interpolation of the independent variables to the cell faces for convection terms.

The interpolation technique used for the convection term is a nonoscillatory quadratic interpolation scheme known as the Uniformly Nonoscillatory Second Order Accurate method (UNO2). This method was developed by Harten and Osher [13]. The explanation here is the one given by Yokota [42], [44].

Interpolations of the independent variables are completed in the following

manner, with S_i^x representing the slope of w in the x direction.

$$w = w_i + S_i^x(x - x_i) \tag{4.24}$$

The repeated indices do not imply summation.

This interpolation is used to construct values for the independent variables at the cell faces, $w_{i+1/2}$, for construction of the differences.

The UNO2 scheme uses the following selection process to determine the value of the slope.

$$S_i^x = \frac{\text{median}(0, w_{i+1/2}^c - w_i, w_i - w_{i-1/2}^c)}{\Delta x/2} \tag{4.25}$$

The $w_{i+1/2}^c$ values are constructed using a quadratic interpolation:

$$w_{i+1/2}^c = \frac{1}{2}(w_i + w_{i+1}) - \frac{1}{4}D_{i+1/2} \tag{4.26}$$

where:

$$D_{i+1/2} = \text{minmod}(w_{i+1} - 2w_i + w_{i-1}, w_{i+2} - 2w_{i+1} + w_i) \tag{4.27}$$

and:

$$\text{minmod}(a, b) = \text{sign}(a)\max(0, \text{sign}(ab)\min(|a|, |b|)) \tag{4.28}$$

The $D_{i+1/2}$ term represents the extension of the $w_{i+1/2}^c$ term from a linear interpolation in van Leer's *Minmod* [36] to the quadratic interpolation in UNO2.

The face centered values, $w_{i+1/2}$, must be constructed for the convection term at both stages of the Runge Kutta time stepping scheme.

4.7 Time Integration of Energy Equation in Solid

The numerical technique used to approximate the time integration of Eqn.(3.88) is a semi-implicit, second order accurate single step technique. The finite difference approximation of Eqn.(3.88) using this time advancement technique is:

$$\frac{e^{[N+1]} - e^{[N]}}{\Delta t} = (1-\lambda)\left(\frac{\nabla(k\nabla T)}{Pe}\right)^{[N]} + \lambda\left(\frac{\nabla(k\nabla T)}{Pe}\right)^{[N+1]} \tag{4.29}$$

where λ is an implicit parameter.

The implicit parameter is set to 1/2 to ensure second order accuracy in time. The time step, Δt, in Eqn.(4.29) is the same time step used in the Runge Kutta time advancement of the vorticity transport and energy equations in the fluid region of the domain.

Due to the nonlinear relation between e and T given by Eqn.(4.2), and the semi-implicit formulation, an iterative solution is needed for Eqn.(4.29). The iteration technique used is the four level multistage scheme developed by Jameson.

To apply this method, Eqn.(4.29) must be rewritten in a pseudo time dependent form. The first step is to move all of the terms to the same side of the equality.

$$0 = -e^{[N+1]} + e^{[N]} + (1-\lambda)\Delta t\left(\frac{\nabla(k\nabla T)}{Pe}\right)^{[N]} + \lambda\Delta t\left(\frac{\nabla(k\nabla T)}{Pe}\right)^{[N+1]} \tag{4.30}$$

The variables e, T and k, at [N+1] are written as the iteration variables $\tilde{e}$, $\tilde{T}$ and $\tilde{k}$. The expression is then set equal to the rate of change of the energy variable with respect to a pseudo time variable:

$$\frac{d\tilde{e}}{dt^*} = -\tilde{e} + e^{[N]} + \frac{\Delta t}{2}\left(\frac{\nabla(k\nabla T)}{Pe}\right)^{[N]} + \frac{\Delta t}{2}\left(\frac{\nabla(\tilde{k}\nabla\tilde{T})}{Pe}\right) \tag{4.31}$$

The energy variable will be iterated with this technique, temperature will be updated using a Newton Iteration described in the following section. The thermal conductivity is then updated using Eqn's (3.55) and (3.56), which are the expressions for $k(T)$.

The term on the right hand side of Eqn.(4.31) is known as the residual. The goal of the iteration process is to drive the residual to zero. When the residual is zero Eqn.(4.30) is satisfied and the iteration variables are the desired quantities at time level [N+1].

Written in residual form Eqn.(4.31) is as follows:

$$\frac{d\tilde{e}}{dt^*} = \text{Res} \tag{4.32}$$

One cycle of the four level multistage scheme is shown below:

$$\begin{aligned}
\tilde{e}^{(1)} &= \tilde{e}^{[k]} + \alpha_1 \Delta t^* \text{Res}^{[k]} \\
\tilde{e}^{(2)} &= \tilde{e}^{(1)} + \alpha_2 \Delta t^* \text{Res}^{(1)} \\
\tilde{e}^{(3)} &= \tilde{e}^{(2)} + \alpha_3 \Delta t^* \text{Res}^{(2)} \\
\tilde{e}^{[k+1]} &= \tilde{e}^{(3)} + \alpha_4 \Delta t^* \text{Res}^{(3)}
\end{aligned} \tag{4.33}$$

where the superscript terms in round brackets refer to the stage level, and the superscript terms in square brackets refer to the pseudo time level.

After each of the four stages the Newton Iteration is applied to determine the new value of $\tilde{T}$ from the new $\tilde{e}$. Using this $\tilde{T}$ value the new $\tilde{k}$ is directly determined. The updated values of $\tilde{T}$ and $\tilde{k}$ are needed for calculation of the residual in the following stage.

This scheme is similar to a four stage Runge Kutta scheme. A few modifications are present which accelerate the convergence rate and reduce storage

requirements. The stage coefficients α_l are not constrained by time accuracy requirements since this is a pseudo time integration to steady state. They can be chosen to best accelerate convergence and aid in stability. The values used are $\alpha_1 = 0.25$, $\alpha_2 = 0.5$, $\alpha_3 = 0.75$ and $\alpha_4 = 1$.

At the completion of one multistage cycle the maximum residual is determined and compared to the specified convergence criteria of 10^{-9}. If the convergence criteria is not met, additional multistage cycles are applied as needed.

4.8 Newton Iteration Solution of Energy Equation

The time marching solution described in Eqn.(4.19) is for a model equation of the form shown in Eqn.(4.18). However, a model equation which more accurately represents the energy equation being solved in the solid is the following:

$$\frac{\partial e}{\partial t} = k\frac{\partial^2 T}{\partial x^2} \tag{4.34}$$

Here the independent variables in the time and spatial derivatives are not the same. The spatial derivative is written in terms of temperature, and the time derivative is written in terms of energy.

As Eqn.(4.34) is time advanced from time level [N] to time level [N+1] it is the energy variable which is updated at the new time level. However, it is the temperature variable which is used to solve for the residuals. It is the residuals which are used to update the energy variable. So the temperature is needed at the new time level, [N+1], before the solution can be time advanced further. An equation which relates energy and temperature is needed.

The specific internal energy is a function of temperature as follows:

$$e(T) = \rho(c_p T + H\xi(T)) \tag{4.35}$$

where Eqn.(4.35) is formulated as in Eqn.'s (3.60) and (3.61).

The Newton Iteration scheme is written as:

$$T^{[k+1]} = T^{[k]} - \frac{e^{[k]}(T) - e}{e'^{[k]}(T)} \tag{4.36}$$

The superscript $[k]$ refers to the iteration number, it is a local counter and does not correspond in any manner to the global time step. The derivative e' refers to change of Eqn.(4.35) with the independent variable T:

$$e'(T) = \frac{\partial e}{\partial T} = \frac{\partial}{\partial T}[\rho(c_p T + H\xi(T))] = \rho(c_p + H\frac{\partial \xi(T^{[k]})}{\partial T}) \tag{4.37}$$

The approximate function, Eqn.'s (3.50) and (3.51), will be used for $e(T)$ and in determining $e'(T)$.

Substituting Eqn.'s (4.35) and 4.37) into the Newton Iteration results in the following:

$$T^{[k+1]} = T^{[k]} - \frac{(\rho c_p T^{[k]} + \rho H\xi(T^{[k]}) - e)}{\rho(c_p + H\frac{\partial \xi(T^{[k]})}{\partial T})} \tag{4.38}$$

where e is the energy variable obtained from the multistage scheme.

Eqn. (4.38) is solved iteratively until the difference between two successive solutions satisfies some predetermined error criteria.

$$|T^{[k+1]} - T^{[k]}| < error \tag{4.39}$$

The error criteria has been chosen as: $error = 10^{-12}$, where T is of the order $O(10^0)$.

The Newton Iteration must be completed to convergence for each grid cell in the solid, at each time step and within all multistage levels.

4.9 Numerical Stability

The time stepping method being used to time advance Eqn.'s (3.82) and (3.83) is an explicit technique; the method being used to time advance Eqn.(3.88) is a semi-implicit technique. Therefore the numerical stability of the solution is an issue. As mentioned previously, the numerical component of the current work is based on previously existing research, discussed in the paper by Yokota [43]. The previous work solves an equation similar in form to Eqn.'s (3.82) and (3.83) with the same numerical techniques. Therefore a stability analysis will be completed on Eqn.(3.88), which is of a form not solved by the original research and is solved using a different numerical technique for time stepping.

A stability analysis will be done to verify Eqn.(3.88) has a stable numerical solution when solved using the aforementioned techniques. This includes the semi-implicit single step time advancement as well as the multistage method used to iterate to convergence at each time step. The stability analysis will be used to determine the maximum allowable time step which can be used to advance the solution in time.

A linearized one dimensional stability analysis will be performed on the following equation:

$$\rho c_p \frac{\partial T}{\partial t} = k \frac{\partial^2 T}{\partial x^2} \tag{4.40}$$

Note that the variable in the time derivative has been written as T instead of energy. Also the thermal conductivity has been assumed to be constant.

These assumptions change the equation from the form which is being solved. They are acceptable though since the results of the stability analysis

will only be used as a rough guideline for selection of the time step. The results of the analysis will be a necessary condition for local stability, not a sufficient condition [15]. In fact, it may be necessary to reduce the time step below the amount determined as a result of the analysis.

A von Neumann analysis involves writing the error in the solution as a Fourier decomposition [15]:

$$\epsilon(x,t) = \sum_{i=0}^{i_{max}} a_i^{(N)} e^{(\sqrt{-1})i\theta_x} \tag{4.41}$$

where θ_x is the phase angle of the decomposed error. The range of θ_x is $0 \leq \theta_x \leq \pi$. $\theta_x = 0$ refers to low frequency errors which act over the entire domain, $\theta_x = \pi$ refers to high frequency errors which act over only two grid cells. $a_i^{(N)}$ is a time dependent amplitude factor. i refers to the location in the grid. The sum will be assumed in further steps.

The numerical solution, T, is then written as the sum of the exact solution, $\overline{T}$, and any error, ϵ.

$$T(x,t) = \overline{T}(x,t) + \epsilon(x,t) \tag{4.42}$$

Since the numerical solution satisfies the original equation, Eqn.(4.40), the error must also satisfy this equation. This allows us to write an equation for the error by applying the specified differencing techniques to the space and time derivatives of the original equation.

4.9.1 Single Step Semi-Implicit Time Advancing

A stability analysis will first be completed on Eqn.(4.40) using the single step semi-implicit method. To reiterate, the finite difference approximation for

this expression is:

$$\frac{T^{[N+1]} - T^{[N]}}{\Delta t} = \frac{(T_{i-1} - 2T_i + T_{i+1})^{[N]}}{2Pe\Delta x^2} + \frac{(T_{i-1} - 2T_i + T_{i+1})^{[N+1]}}{2Pe\Delta x^2} \quad (4.43)$$

where Δt and Δx refer to the time step and grid spacing respectively.

A finite difference equation can be written for the error by making use of Eqn.(4.42), which allows substitution of Eqn.(4.41) into the finite difference approximation, Eqn.(4.43). The result is the following:

$$\begin{aligned} a^{(N+1)} \quad & e^{(\sqrt{-1})i\theta_x} = a^{(N)} e^{(\sqrt{-1})i\theta_x} + \\ & \tfrac{\Delta t}{2Pe\Delta x^2} \left[a^{(N)} e^{(\sqrt{-1})(i-1)\theta_x} - 2a^{(N)} e^{(\sqrt{-1})i\theta_x} + a^{(N)} e^{(\sqrt{-1})(i+1)\theta_x} \right] \quad (4.44) \\ + \quad & \tfrac{\Delta t}{2Pe\Delta x^2} \left[a^{(N+1)} e^{(\sqrt{-1})(i-1)\theta_x} - 2a^{(N+1)} e^{(\sqrt{-1})i\theta_x} + a^{(N+1)} e^{(\sqrt{-1})(i+1)\theta_x} \right] \end{aligned}$$

Eqn.(4.44) must be simplified into an expression to get the error at time level [N+1] as a function of the error at time level [N]. The following substitution can be made to simplify Eqn.(4.44):

$$e^{(\sqrt{-1})\theta} = \cos\theta + (\sqrt{-1})\sin\theta \quad (4.45)$$

The following trigonometric identity must also be applied:

$$\sin^2\theta = \frac{1 - \cos 2\theta}{2} \quad (4.46)$$

An error amplification factor, G, is defined as the ratio between the error from two successive time steps.

$$G = \frac{\text{error at } (N+1)}{\text{error at } (N)} = \frac{a^{(N+1)}}{a^{(N)}} \quad (4.47)$$

The amplification factor is a function of the differencing techniques used, the material properties, any velocities present, the time step and the mesh size.

Since the time step is the only one of these parameters not yet specified, the stability analysis is used to determine the allowable step size.

If the error grows with time the solution will be unstable, if the error does not grow with time the solution is stable. This requirement for stability is written as follows:

$$G \leq 1 \tag{4.48}$$

Once Eqn.'s (4.45) - (4.47) are applied to Eqn.(4.44), the finite difference approximation shown in Eqn.(4.40) can be shown to have an error amplification factor given by the following equation:

$$G = 1 - 2G\left[\frac{\Delta t}{\Delta x^2 \mathrm{Pe}}\right]\sin^2(\theta_x/2) - 2\left[\frac{\Delta t}{\Delta x^2 \mathrm{Pe}}\right]\sin^2(\theta_x/2) \tag{4.49}$$

Further algebraic manipulation results in the final form of the expression for the error amplification factor:

$$G = \frac{1 - 2\left[\frac{\Delta t}{\Delta x^2 Pe}\right]\sin^2(\theta_x/2)}{1 + 2\left[\frac{\Delta t}{\Delta x^2 Pe}\right]\sin^2(\theta_x/2)} \tag{4.50}$$

Recall that the range of the θ_x is: $0 \leq \theta_x \leq \pi$. Over this range $\sin^2(\theta_x/2)$ takes on the following values: $0 \leq \sin^2(\theta_x/2) \leq 1$. Therefore Eqn.(4.50) satisfies the stability requirement of $G \leq 1$ for all positive values of Δt, Δx^2 and Pe. Eqn.(4.40) is unconditionally stable when solved using a single step semi-implicit time integration with central differencing of the spatial derivative. Numerical stability requirements place no limitations on the allowable time step for the time advancement of the energy equation in the solid.

4.9.2 Multistage Convergence Iteration

Next the stability of the four level multistage technique which is used to iterate the energy equation in the solid to convergence at each time level will be considered. To reiterate, the equation being solved with this technique is the following:

$$\frac{d\tilde{e}}{dt^*} = -\tilde{e} + e^{[N]} + \frac{\Delta t}{2}\left(\frac{\nabla(k\nabla T)}{Pe}\right)^{[N]} + \frac{\Delta t}{2}\left(\frac{\nabla(\tilde{k}\nabla\tilde{T})}{Pe}\right) \tag{4.51}$$

To simplify the stability analysis, the energy variable will be replaced with temperature, and the thermal conductivity, $\tilde{k}$, will be assumed constant. The variables at time level N are constants and do not have any effect on the stability of the solution. After the above simplifications, the equation which will be analyzed for numerical stability is the following:

$$\frac{dT}{dt^*} = -T + \left(\frac{\Delta t}{2Pe}\right)\nabla^2 T \tag{4.52}$$

Eqn.(4.52) is solved with the 4 level multistage scheme, the solution sequence proceeds as follows:

$$\begin{aligned}
T^{(1)} &= T^{[k]} + 0.25\Delta t^* \left[-T + \left(\frac{\Delta t}{2Pe}\right)\nabla^2 T\right]^{[k]} \\
T^{(2)} &= T^{(1)} + 0.5\Delta t^* \left[-T + \left(\frac{\Delta t}{2Pe}\right)\nabla^2 T\right]^{(1)} \\
T^{(3)} &= T^{(2)} + 0.75\Delta t^* \left[-T + \left(\frac{\Delta t}{2Pe}\right)\nabla^2 T\right]^{(2)} \\
T^{[k+1]} &= T^{(3)} + \Delta t^* \left[-T + \left(\frac{\Delta t}{2Pe}\right)\nabla^2 T\right]^{(3)}
\end{aligned} \tag{4.53}$$

where the second order differential will be approximated with second order accurate central differencing. Again Δt^* is the pseudo time step of the iteration and Δt is the global time step.

Applying the same techniques as the previous stability analysis it is possible to write an expression for the error amplification factor of each stage. They are:

$$\begin{aligned} G^1 &= 1 - 0.25\Delta t^* \left[1 + 4\left[\frac{\Delta t}{\Delta x^2 Pe}\right]\sin^2(\theta_x/2)\right] \\ G^2 &= G^1\left(1 - 0.5\Delta t^* \left[1 + 4\left[\frac{\Delta t}{\Delta x^2 Pe}\right]\sin^2(\theta_x/2)\right]\right) \\ G^3 &= G^2\left(1 - 0.75\Delta t^* \left[1 + 4\left[\frac{\Delta t}{\Delta x^2 Pe}\right]\sin^2(\theta_x/2)\right]\right) \\ G &= G^3\left(1 - \Delta t^* \left[1 + 4\left[\frac{\Delta t}{\Delta x^2 Pe}\right]\sin^2(\theta_x/2)\right]\right) \end{aligned} \tag{4.54}$$

The expression for the error amplification factor of a complete cycle is a fourth order polynomial in the unknown Δt^*. This polynomial must be compared to the stability requirement of $G \leq 1$. From this comparison it can be determined if the scheme is conditionally stable, and then limits may be set on Δt^* to ensure the scheme is numerically stable. Ideally an analytical expression for the limiting values of Δt^* is preferred. However due to the complexity of the expression for G, the error amplification factor will be plotted with selected values of the parameters Δx^2, Δt, Pe and Δt^*.

A complication exists in that although Pe and Δt are constant, Δx^2 varies over the domain in the solid. However it is known that Δt is of order $O(10^{-4})$, Pe is of order $O(10^2)$ and Δx^2 varies between $O(10^{-3}) \leq \Delta x^2 \leq O(10^{-5})$. Therefore the following is true:

$$O(10^{-3}) \leq \Psi = \frac{\Delta t}{\Delta x^2 Pe} \leq O(10^{-1}) \tag{4.55}$$

Following in Figure 4.2 is a plot of the error amplification factor with Ψ varying from $O(10^{-3})$ to $O(10^0)$ with the selected value of $\Delta t^* = 0.1$. This

is the value of Δt^* used in the simulations which will be presented in the results.

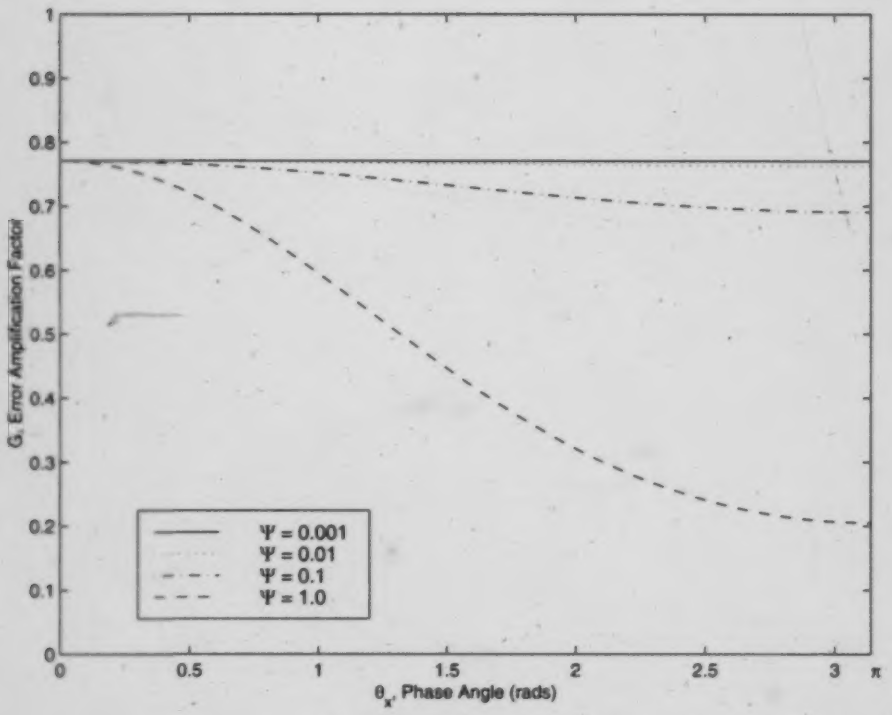

Figure 4.2: Error Amplification Factor for Multistage Solution of Conduction Equation

4.10 Boundary Conditions

4.10.1 Fluid Field Boundary Conditions

Referring to Figure (2.4), there are four different boundary conditions which must be considered in the fluid field: the inflow, outflow, periodic, and solid boundaries. The flow variables which require boundary conditions are the potential, ϕ, the viscous correction stream function, ψ, the vorticity, ω, and the temperature T. Since the periodic boundary is exactly what it implies, specific details of the application will not be given.

Inflow Boundary The flow field boundary conditions at the inlet are all set to model a uniform flow. Referring to the decomposition, Eqn.(3.64), a uniform flow across the inlet requires that there be no change in any of the flow variables across the inlet. The temperature at the inlet is set to the desired value of the flow. Since an inlet shear is not desired vorticity is set to zero.

$$\left.\frac{\partial \phi}{\partial \xi}\right|_{inlet} = 0 \tag{4.56}$$

$$\left.\frac{\partial \psi}{\partial \xi}\right|_{inlet} = 0 \tag{4.57}$$

$$\omega_{inlet} = 0 \tag{4.58}$$

$$T_{inlet} = \text{constant} \tag{4.59}$$

where the value of T_{inlet} will be specified to match the physical characteristics of the selected problem.

Outflow Boundary The conditions applied at the outlet are chosen to allow whatever phenomena may be present to convect out of the domain.

$$\phi_{outlet} = 0 \tag{4.60}$$

$$\left.\frac{\partial \psi}{\partial \xi}\right|_{outlet} = 0 \tag{4.61}$$

$$\left.\frac{\partial \omega}{\partial \xi}\right|_{outlet} = 0 \tag{4.62}$$

$$\left.\frac{\partial^2 T}{\partial \xi^2}\right|_{outlet} = 0 \tag{4.63}$$

On the inlet, outlet and solid boundaries the derivative of ϕ has been specified. Laplace's equation, Eqn.(4.1), gives solutions unique to a constant. Therefore it is necessary to prescribe a value for ϕ at the outlet to aid in convergence of the continuity equation.

Solid Boundary It is important to note that there are two different components to the boundary conditions applied at the solid surface. First there are the analytical conditions applied to the variables used in construction of the flow field. The second stage is in applying the no-flux condition at the surface, in the actual calculation of the residuals mentioned previously. The flux across the solid surface is set to be zero to ensure the solid surface is accurately represented.

The analytical condition applied to the flow potential is the following:

$$\left.\frac{\partial \phi}{\partial \eta}\right|_{wall} = -U_\infty \cdot \hat{n} \tag{4.64}$$

which comes from:

$$[\overline{v} \cdot \hat{n}]_{wall} = 0 \longrightarrow \left.\frac{\partial \phi}{\partial \eta}\right|_{wall} + U_\infty \cdot \hat{n} = 0 \tag{4.65}$$

where:

$$u_\eta = U_\infty \cdot \hat{n} + \frac{\partial \phi}{\partial \eta} + \frac{\partial \psi}{\partial \xi} \tag{4.66}$$

The final term is not needed since:

$$\psi_{wall} = \text{constant} \tag{4.67}$$

For the vorticity correction stream function the boundary condition at the wall comes from a second order Taylor series expansion of the stream function at the wall:

$$\psi_{wall+1} = \psi_{wall} + \left.\frac{\partial \psi}{\partial n}\right|_{wall} \Delta n + \frac{1}{2!} \left.\frac{\partial^2 \psi}{\partial n^2}\right|_{wall} \Delta n^2 + O(\Delta n^3)... \tag{4.68}$$

Recalling the relation between ω and ψ, Eqn.(4.3), and making use of Eqn.(4.67) this can be reduced to:

$$\psi_{wall+1} = \psi_{wall} + \left.\frac{\partial \psi}{\partial n}\right|_{wall} \Delta n + \frac{1}{2} \omega_{wall} \Delta n^2 \tag{4.69}$$

Rearranging this gives an expression for the vorticity at the wall:

$$\omega_{wall} = \frac{2(\psi_{wall+1} - \psi_{wall} - \left.\frac{\partial \psi}{\partial n}\right|_{wall} \Delta n)}{\Delta n^2} \tag{4.70}$$

Due to the importance and complexity of the thermal boundary condition along the wall, it will be treated separately in the following section.

4.10.2 Thermal Interaction Boundary Condition

For this work the most important physical phenomenon to capture is the thermal interaction between the fluid flow and the smart material. Numerically this is the boundary condition linking the energy equations in the two regions of the domain, Eqn.'s (3.83) and (3.88). Since it is the temperature of the smart material which determines the state, any heat loss or gain to the surrounding fluid is of extreme interest.

The requirement of this boundary condition is to accurately capture the physics at the boundary without affecting the solution in any way. A simplified schematic in Figure 4.3 diagrams the problem at the boundary.

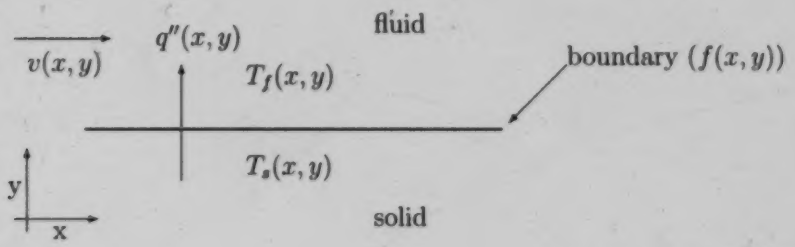

Figure 4.3: Diagram of Fluid and Smart Material Boundary

Complexities of the problem lie in the fact that the velocity and temperature fields are functions of two dimensions. The boundary itself is also a function of two dimensions.

From the literature, there are two standard methods used to handle this

thermal boundary condition between a solid and a surrounding fluid. Either specify the surface temperature of the solid to be a given constant [9],[16],[17],[28],[39], or specify the heat flux at the surface [28],[39]. For the current work both of these options are unacceptable. They govern the temperature field solution in the solid either directly (specified surface temperature), or indirectly (specified surface heat flux).

Numerically the solution is simplified in that the domain is discretized along the boundary into discrete cells. At an individual cell level this reduces the problem to one dimension. A numerical boundary condition is still required for the boundary cells which captures the physics. A diagram of a typical boundary cell is shown in Figure 4.4.

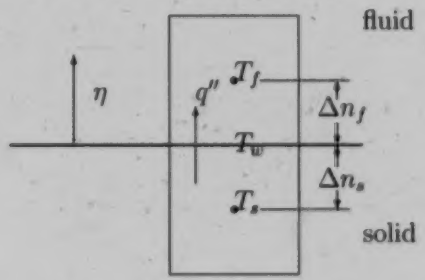

Figure 4.4: Boundary Cell

The thermal boundary condition which occurs in nature is that any heat which flows out of the solid must flow into the fluid. This is written as

follows:

$$q''_{fluid} = q''_{solid} \tag{4.71}$$

The heat flux in the solid is due only to conduction, since there is no convective velocities present internally. It is desired to write the heat flux in the fluid as a function of only conduction at the surface. Therefore it will be assumed that temperature gradients are linear in the fluid perpendicular to the surface. For this to be true the grid at the surface must be sufficiently fine so as to resolve the viscous boundary layer at the wall. In the viscous boundary layer the y direction velocities are small compared to the x direction velocities. Therefore any variations in T in the y direction would be primarily due to conduction. A flat plate boundary layer assumption may be made to calculate the approximate expected thickness of the viscous boundary layer [25]. Based on this calculation it can be shown that on the solid surface the viscous boundary layer is contained in more than one grid level. The numerical grid is fine enough to resolve the viscous boundary layer. Therefore the assumption of a linear temperature gradient at the surface is valid. This allows us to write Eqn.(4.71) as :

$$\left(k\frac{\partial T}{\partial n}\right)\Big|_{fluid} = \left(k\frac{\partial T}{\partial n}\right)\Big|_{solid} \tag{4.72}$$

A first order discretization of the differentials has been used over the half of the boundary cells nearest the interface, as shown below:

$$k_f\left(\frac{T_f - T_w}{\Delta n_f}\right) = k_s\left(\frac{T_w - T_s}{\Delta n_s}\right) \tag{4.73}$$

Rearranging for the temperature at the wall ,T_w, gives the following:

$$T_w = \left[\frac{T_f + \left(\frac{k_s}{k_f}\right)\left(\frac{\Delta n_f}{\Delta n_s}\right)T_s}{1 + \left(\frac{k_s}{k_f}\right)\left(\frac{\Delta n_f}{\Delta n_s}\right)}\right] \tag{4.74}$$

An alternative would have been to use a convective heat transfer coefficient, h, at the boundary. The equation for the boundary condition would have been as follows:

$$h\left(T_f - T_{wall}\right)\Big|_{fluid} = \left(k\frac{\partial T}{\partial \eta}\right)\Big|_{solid} \tag{4.75}$$

The parameter h is an approximation made when it is not possible to study the thermal interaction between the fluid and solid on a small scale. For this work the domain is resolved into finite divisions small enough to discern boundary layers. Therefore it is possible to resolve the linear temperature distribution region of the fluid, and it is not necessary to use h values at the boundary.

CHAPTER 5

RESULTS

5.1 Values of Dimensionless Groups

Before any simulations can be completed, values of the dimensionless groups present in the nondimensional form of the governing equations must be prescribed. To do this quantities are needed for the specific fluid properties, solid properties and reference variables.

Table 5.1 contains values of the fluid properties used for this work [37].

Property	Symbol	Value
Thermal conductivity	k	$0.5W/mK$
Density	ρ_o	$1050kg/m^3$
Volumetric thermal expansion coefficient	β	$0.361(10^{-6})$
Specific heat capacity	c_p	$3.85(10^3)J/kgK$
Viscosity	μ	$2.09(10^{-3})kg/ms^2$

Table 5.1: Fluid Material Properties

As an approximation the volumetric thermal expansion coefficient for

water at the freestream temperature of $37°C$ has been used.

Table 5.2 contains the property values used for the smart material [1].

Property	Symbol	Value
Martensitic thermal conductivity	k_M	$1.8W/mK$
Austenitic thermal conductivity	k_A	$18W/mK$
Volume specific heat capacity	ρc_p	$2.12(10^6)J/m^3K$
Latent energy of phase change	ρH	$0.148(10^9)J/m^3$

Table 5.2: Solid Material Properties

Values of the reference parameters used for length, velocity and temperature mentioned in Section 3.6 must be prescribed. The axial length of the smart material is $1mm$ [32], this is the reference length L. The freestream velocity of the fluid is $0.1m/s$ [33], this is the reference velocity U_∞. The reference temperature is the initial temperature of the solid, $T_{(initial)}^{(solid)} = 273K$.

The values from Tables 5.1 and 5.2 along with the reference quantities can be substituted into the equations for the dimensionless groups, Eqn.'s (3.81) and (3.87). Following in Table 5.3 are the values of the dimensionless groups for this work.

5.1.1 Freestream Fluid Velocity

Isothermal test cases resulted in vortices being shed from the solid at a frequency of approximately 50Hz. Blood flow cycles at frequencies of approximately of 1Hz [21]. Clinical experience has shown the phase transformation of the smart material IVCF to occur very quickly, being described as "*instan-*

Dimensionless Group	Symbol	Value
Reynolds number	Re	50
Prantl number	Pr	25 [37]
Grashof number	Gr	245
Peclet number	Pe	118

Table 5.3: Dimensionless Groups

taneous" [31]. Therefore it is expected that the smart material will change phase in a period of time which is less than one complete heartbeat. For the time lengths that will be simulated the shedding vortices will be of greater influence to the flow field than the oscillatory nature of the freestream velocity. Therefore all of the test cases presented have a constant free stream velocity in the fluid region.

5.2 Numerical Domain

Shown in Figure 5.1 is the supplied numerical grid used in the fluid region of the domain. The domain in the fluid region consists 128 x 32 cells with 48 cells over the solid region. Since the formulation is viscous, the grid is packed towards the leading and trailing edges and over the surface of the solid. Figure 5.2 is the developed numerical grid used in the solid portion of the domain. The domain in the solid region consists of 48 x 24 cells.

Due to the blunt leading and trailing edges present in the geometry there is a grid discontinuity around the leading and trailing edges. This skewing of the grid alters the truncation error in these localized regions. If large

gradients in the flow variables occur in these regions, it is possible that large truncation errors could develop and influence other regions of the domain. A temperature limiter has been applied to prevent these truncation errors from affecting the solution in other areas of the domain. This is similar in concept to the flux limiter applied in the UNO2 convection scheme.

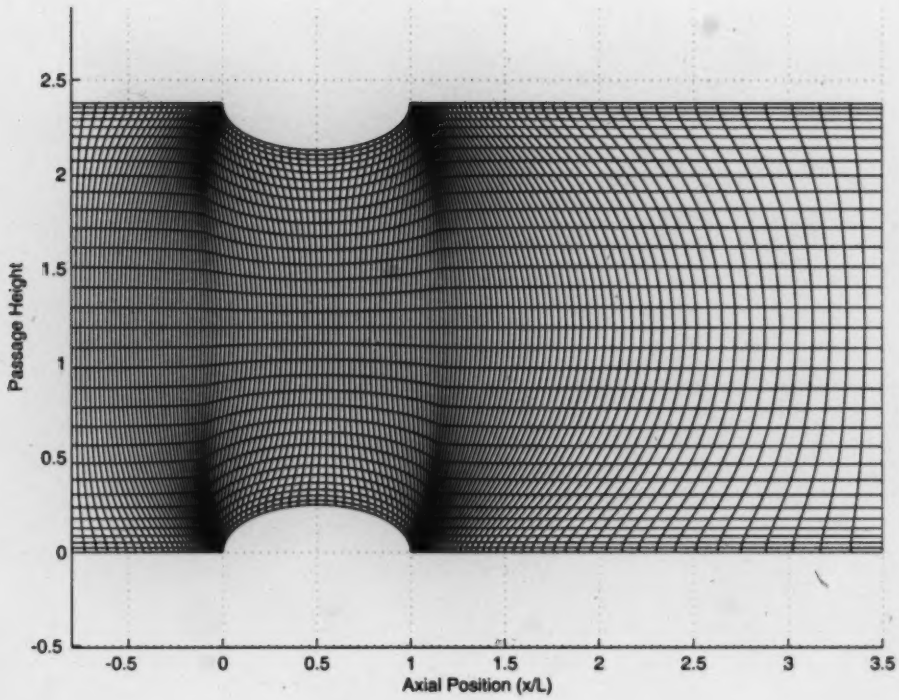

Figure 5.1: Supplied Grid in Fluid Portion of the Domain

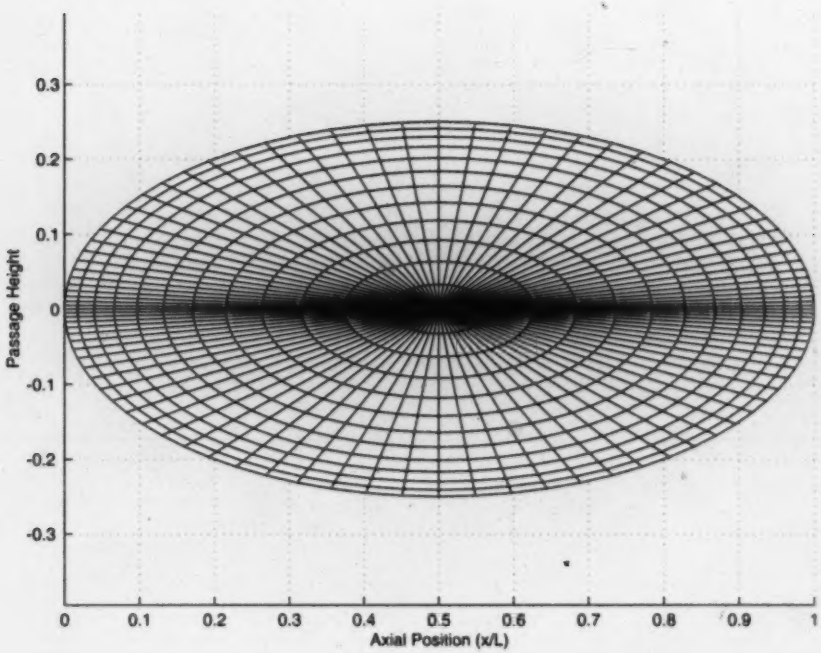

Figure 5.2: Developed Grid in Solid Portion of the Domain

5.3 Development of Flow Field Periodic Solution

The initial condition used for the flow field is an impulsive acceleration. The solution which eventually develops in the flow field is the periodic shedding of vortices from the ellipse. It takes time for the periodic solution to develop as the effects from the impulsive start must convect out of the domain. Periodic shedding of vortices begins after a time equivalent to approximately four shedding cycles. An additional three vortex shedding cycles were then computed to ensure that any transients occurring during startup were no longer present, and the flow was fully periodic. Vorticity contours through one full cycle of vortex shedding are shown in Figures 5.3(a) - 5.3(e).

Figure 5.4 is the average vorticity in the fluid over approximately fifteen shedding cycles. This is for an isothermal simulation. The presence of temperature gradients in the flow field does not alter the vorticity an appreciable amount. Differences between the flow field kinetic energy from isothermal and nonisothermal test cases are less than 0.1%, relative to the isothermal amount. This is due to the weighting value used for the term which generates vorticity as a result of temperature gradients. A value of 0.1 has been used for the generation term, relative to the convective term weighting of 1.

Text resumes on page 93

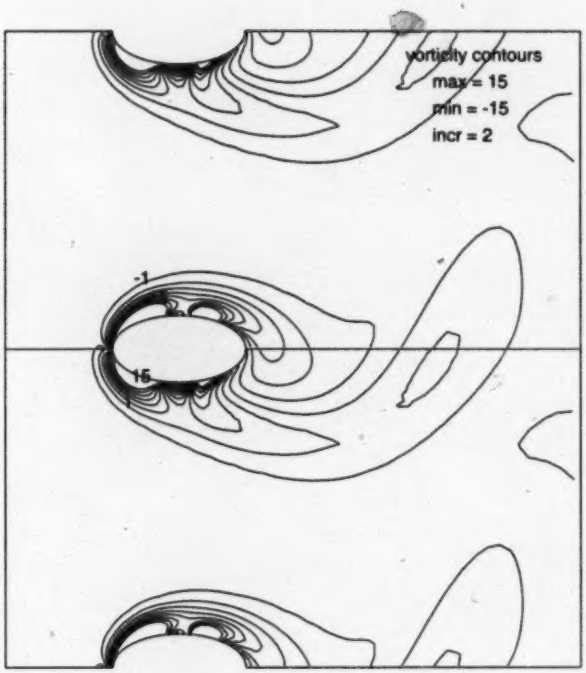

Figure 5.3(a): Vorticity Contours in Fluid Region, t = 0.004

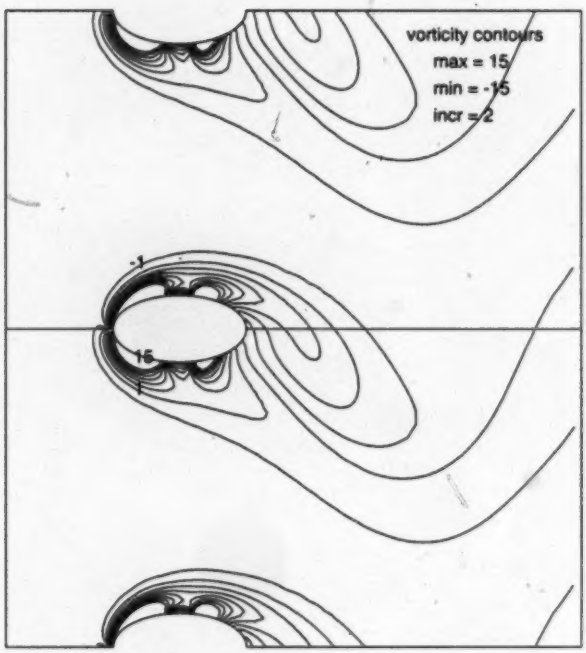

Figure 5.3(b): Vorticity Contours in Fluid Region, t = 0.008

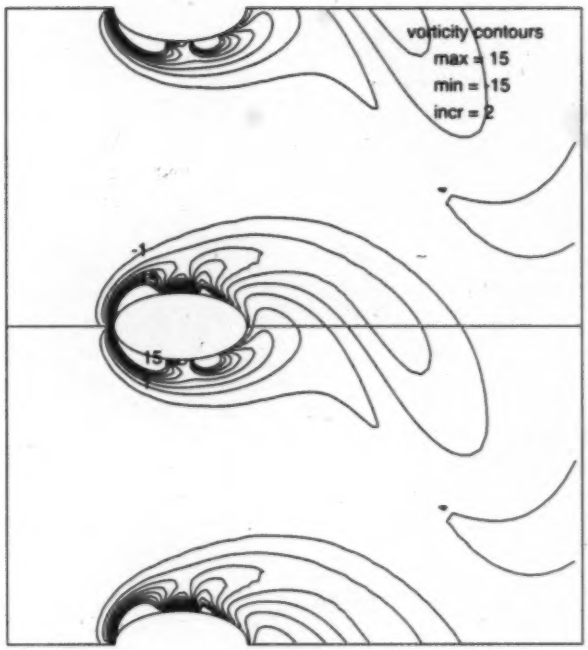

Figure 5.3(c): Vorticity Contours in Fluid Region, t = 0.012

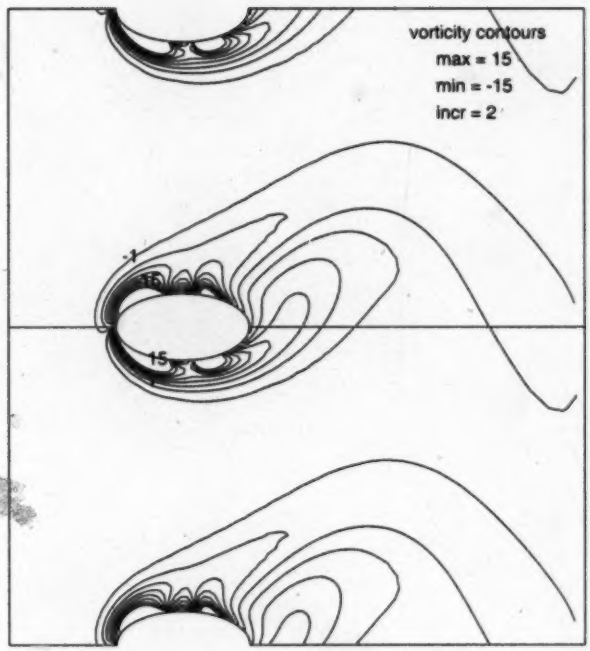

Figure 5.3(d): Vorticity Contours in Fluid Region, t = 0.016

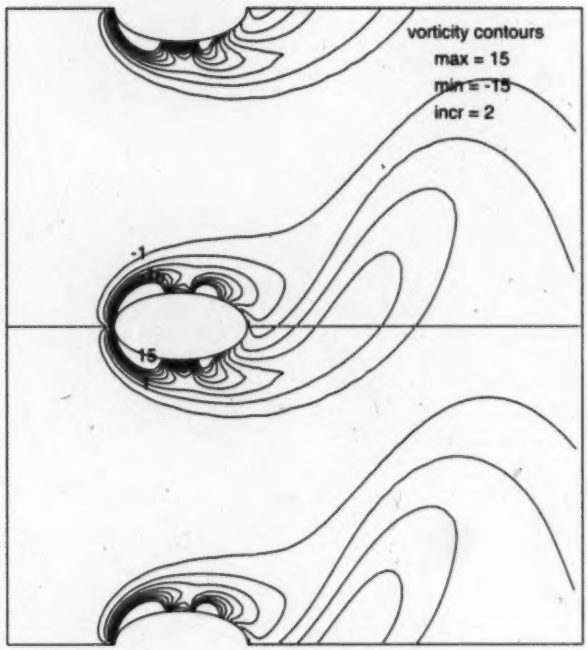

Figure 5.3(e): Vorticity Contours in Fluid Region, t = 0.020

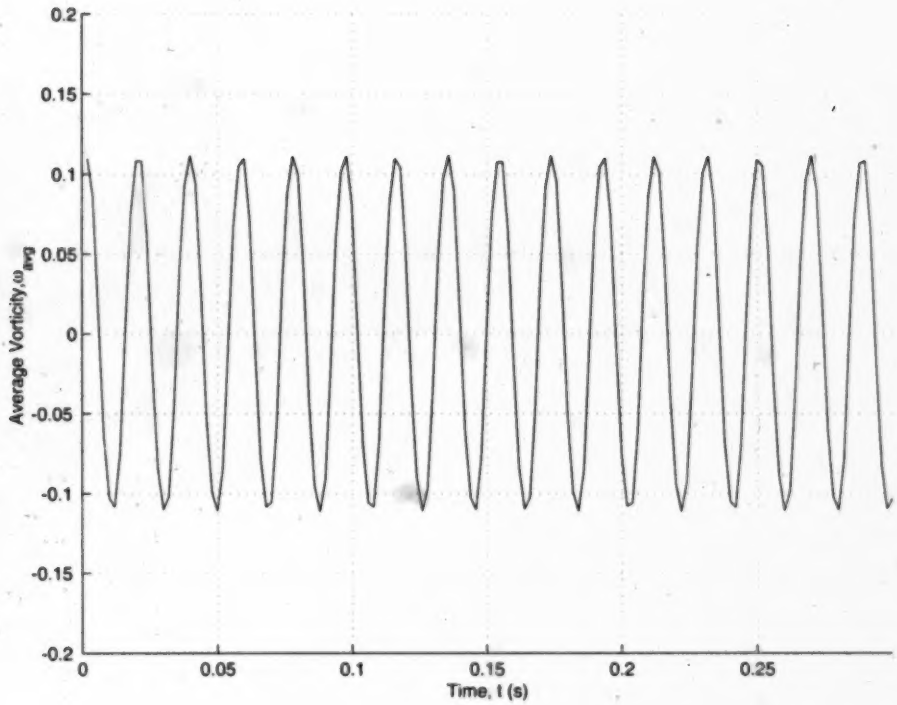

Figure 5.4: Average Vorticity History for Isothermal Simulation

5.4 Constant Material Properties in Solid Region

5.4.1 Results from Two Dimensional Simulation

The first test case to be presented is a solid material with constant properties at an initial temperature of $273K$, surrounded by fluid flow with a freestream temperature of $310K$. The flow field initial condition used for this case is the periodic solution from the isothermal simulation. The values of the dimensionless parameters used are listed in Table 5.3.

As the simulation advances in time the average temperature of the solid is expected to asymptotically approach the freestream temperature of the fluid. Figure 5.5 is the average temperature of the solid with time.

From the temperature distributions in the fluid and the solid it is possible to compute the average heat transfer coefficient on the surface of the solid. A plot of the heat transfer coefficient time history is shown in Figure 5.6.

The average heat transfer coefficient on the surface is determined from:

$$\overline{h} = \frac{\overline{k_f \left.\frac{\partial T}{\partial n}\right|_f}}{(T_\infty - T_{surface})} \tag{5.1}$$

where the overline refers to quantities averaged over the surface.

The average temperature in the solid is making a slow asymptotic approach to the freestream temperature. This is explained by the oscillation around a near zero value for the average surface heat transfer coefficient. As the surface temperature of the solid nears the freestream temperature of the fluid, the rate of heat transfer into the solid is decreasing.

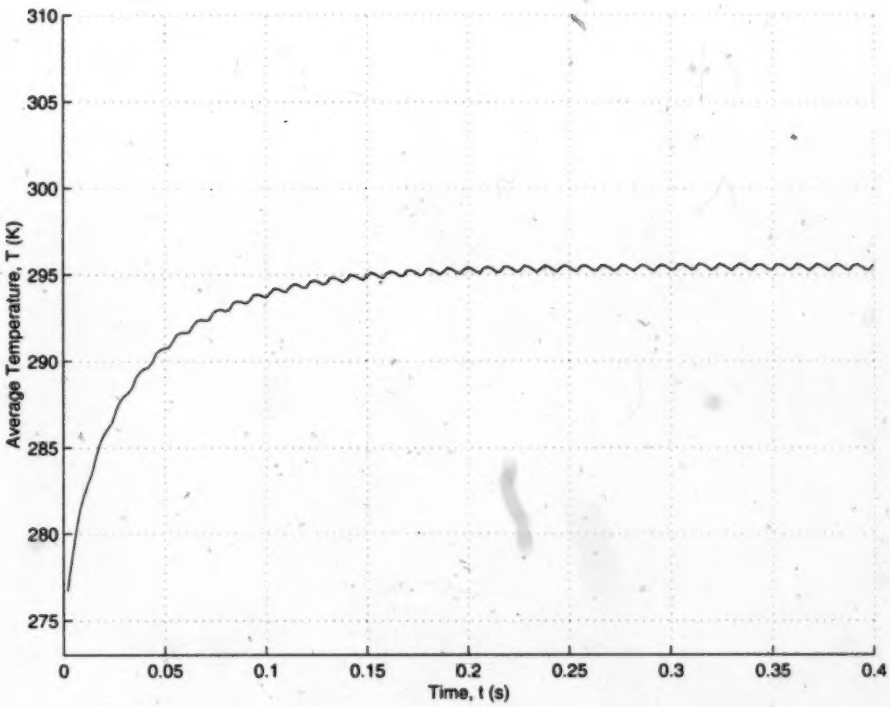

Figure 5.5: Average Temperature History for Material with Constant Properties

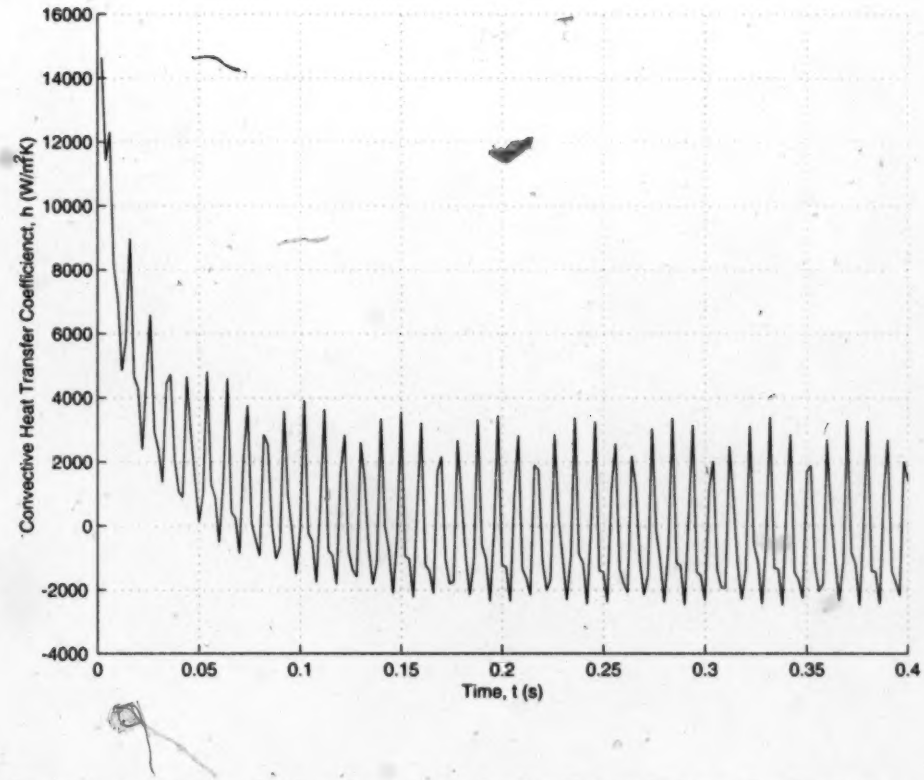

Figure 5.6: Average Surface Heat Transfer Coefficient History for Constant Property Material

5.4.2 Comparison to One Dimensional Analysis

A one dimensional analysis can be used to approximate the heat transfer between an object and a fluid [1]. The assumptions of a one dimensional analysis are that the temperature of the object is uniform over the cross section, and that the heat transfer rate is constant with time. A measure of whether or not a one dimensional analysis is valid is the Biot number:

$$\mathrm{Bi} = \frac{hL}{k_s} \tag{5.2}$$

where h is the convective heat transfer coefficient, L is a characteristic length of the solid, and k_s is the thermal conductivity of the solid. The Biot number is the ratio of the internal thermal resistance of the solid to the boundary layer thermal resistance. A one dimensional analysis is expected to give acceptable results for $|\mathrm{Bi}| \leq 0.1$.

The one dimensional analysis uses the following expression:

$$-V\rho c_p \frac{dT}{dt} = hA_s(T - T_\infty) \tag{5.3}$$

where V is the volume of the solid, A_s is the surface area of the solid, T is the average temperature of the solid, T_∞ is the freestream temperature of the fluid and h is the convective heat transfer coefficient.

The difficulty in using Eqn.(5.3) is the selection of a suitable value for h. As can be seen in Figure 5.6, the convective heat transfer coefficient changes with time. For comparison with the results from the two dimensional analysis, three different values of h have been selected: the average, a value towards the lower end of the range of h's calculated, and a value towards the higher end of the range of h's calculated. Figure 5.7 shows the

average temperature history from both the 2D and 1D analyses. As this plot indicates, it is difficult to select a single value of h which can reproduce the results of the 2D simulation in a 1D analysis.

One reason for this is the variation of the heat transfer coefficient with time in the two dimensional analysis. An additional reason is the range of Biot numbers that occur during the simulation. Shown in Figure 5.8 is the calculated Biot number from the two dimensional analysis. The Biot number is rarely below the required level for an accurate one dimensional analysis. Therefore a one dimensional analysis is not expected to give accurate results for this application. There is little which designers could do to improve this situation, since for a specific material and application the Biot number is a set quantity.

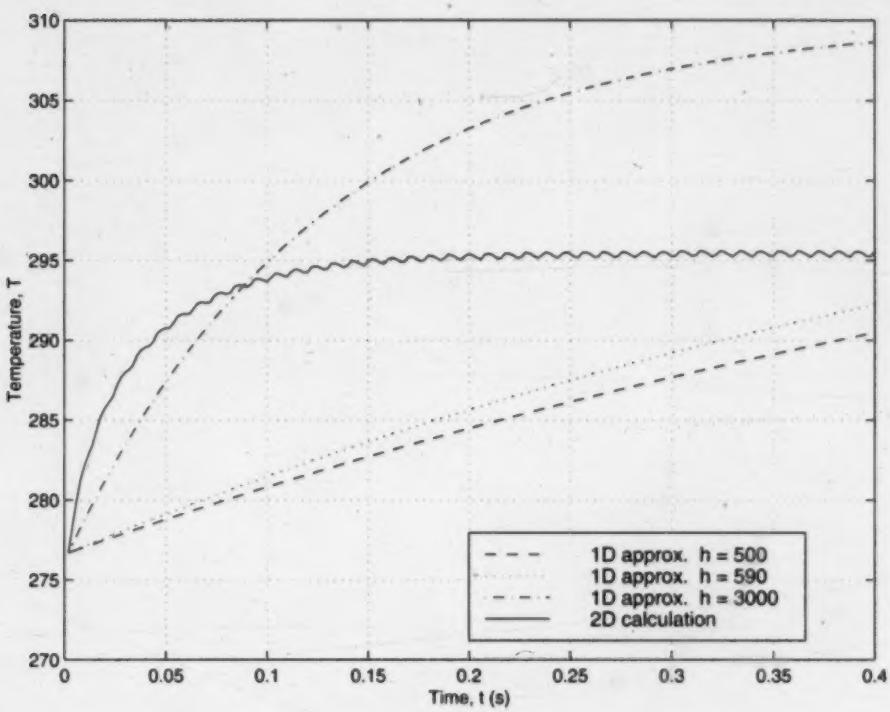

Figure 5.7: Comparison Between 1D and 2D Temperature Histories

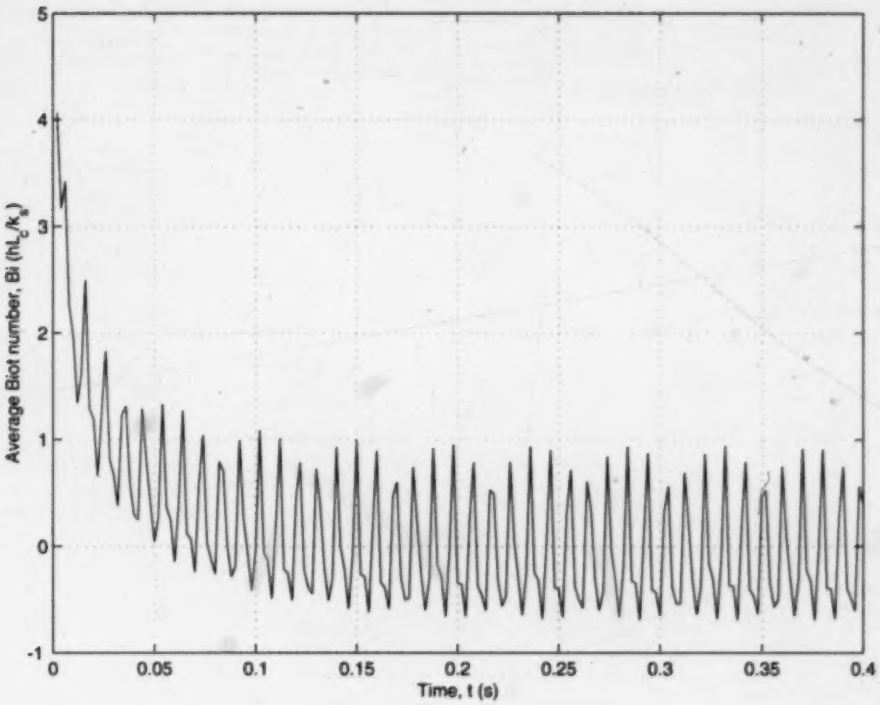

Figure 5.8: Time History of Biot Number for Constant Property Material

5.5 Comparison between Smart Material and Constant Property Material

5.5.1 Results from Two Dimensional Simulation

The next test case to be presented is a smart material with variable material properties at an initial temperature of $273K$, surrounded by a fluid with a freestream temperature of $310K$. The flow field initial condition used for this case is again the periodic solution from the isothermal test case. The values of the dimensionless parameters used are the same ones in Table 5.3. The smart material will initially be martensite. The temperature at which the austenite transformation will start is $275K$, and the transition finish temperature is $285K$. As the simulation proceeds in time the material is expected to change phase to austenite as the average solid temperature approaches the freestream fluid temperature.

Figure 5.5 shows the change in average temperature of the solid with time, for both the constant property test case and the smart material test case. The reduced rate of temperature increase for the smart material during the first tenth of a second is due to the increased energy requirements during the phase change. This is supported by Figure 5.10, which shows the time history of the average internal energy for both the constant property material and the smart material. Although the average temperature of the smart material is lower than that of the constant property material, its' internal energy is greater due to the phase change. Once the phase change is completed the smart material temperature increases at a greater rate due to the higher thermal conductivity of the austenitic phase. The martensitic material properties

were used for the constant property test case.

Convective heat transfer coefficients on the surface were calculated using Eqn.(5.3). The time history of the convective heat transfer coefficient for the smart material is shown in Figure 5.11. Again the convective heat transfer coefficient varies greatly with time. The heat transfer coefficient for the smart material is different from the values obtained for the constant property material. This is shown in Figure 5.12, which is the heat transfer coefficients for these test cases averaged over the vortex shedding cycles.

The average temperature of the smart material is again making a slow asymptotic approach to the eventual steady state value. This is a result of the average surface heat transfer coefficient oscillating around a near zero value. The heat transfer across the surface of the solid reduces as the surface temperature approaches the freestream temperature.

Text resumes on page 106

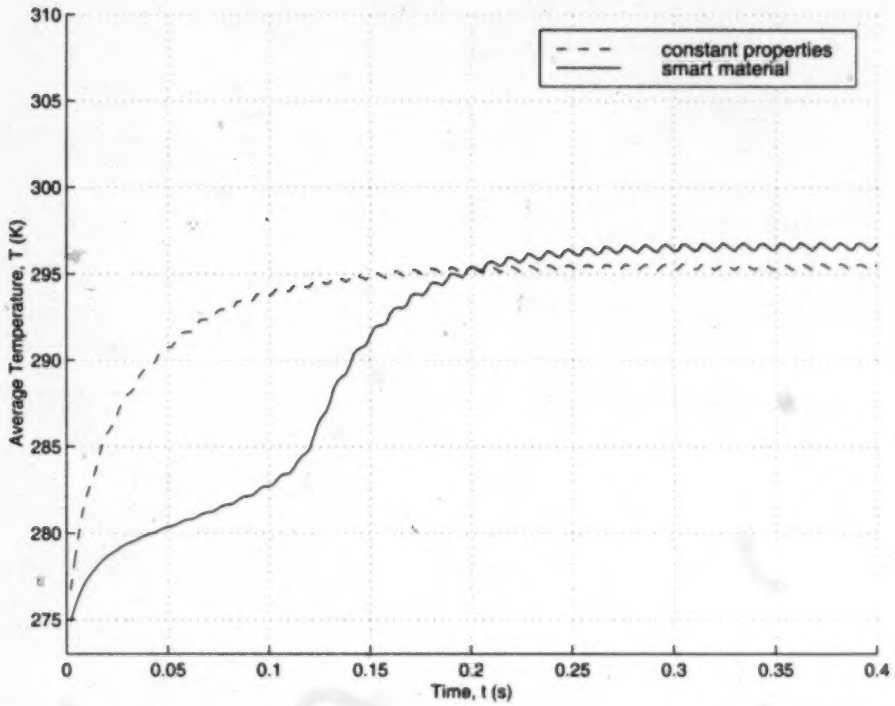

Figure 5.9: Average Temperature History for Smart Material and Constant Property Material

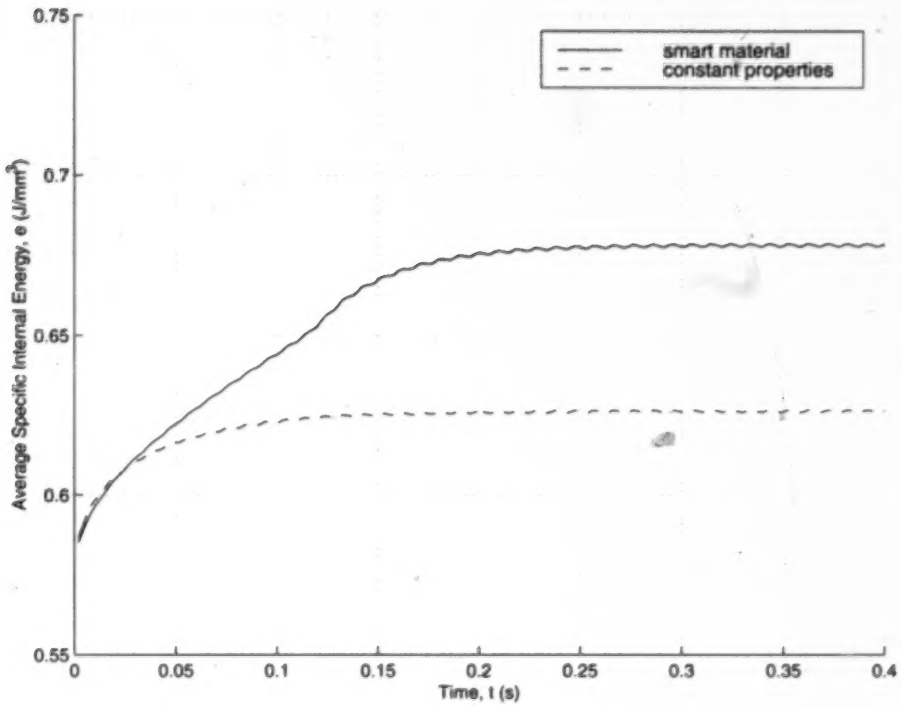

Figure 5.10: Average Internal Energy History for Smart Material and Constant Property Material

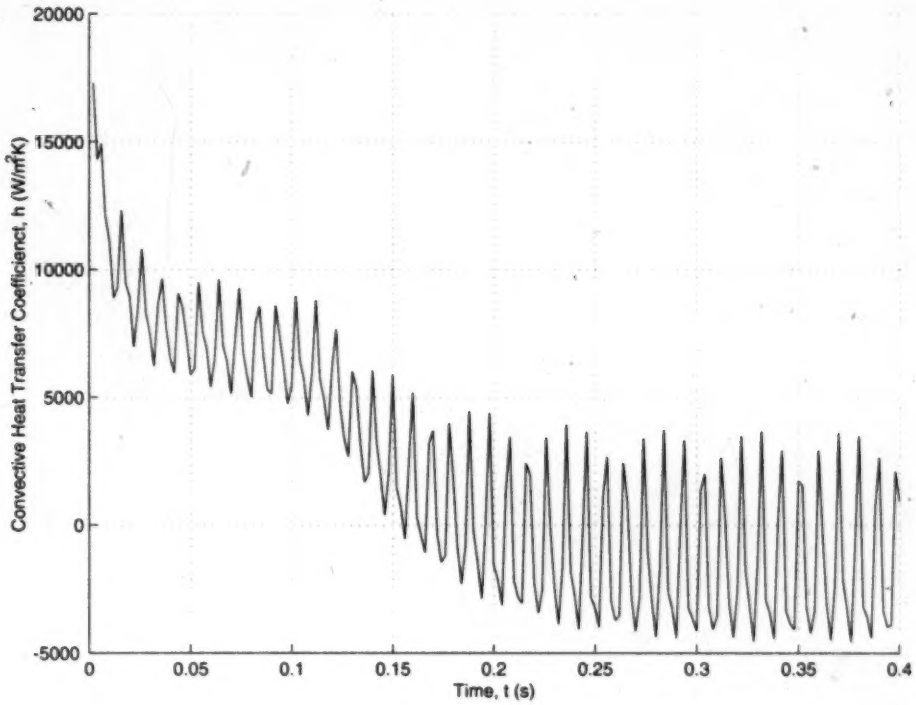

Figure 5.11: Average Surface Heat Transfer Coefficient for Smart Material

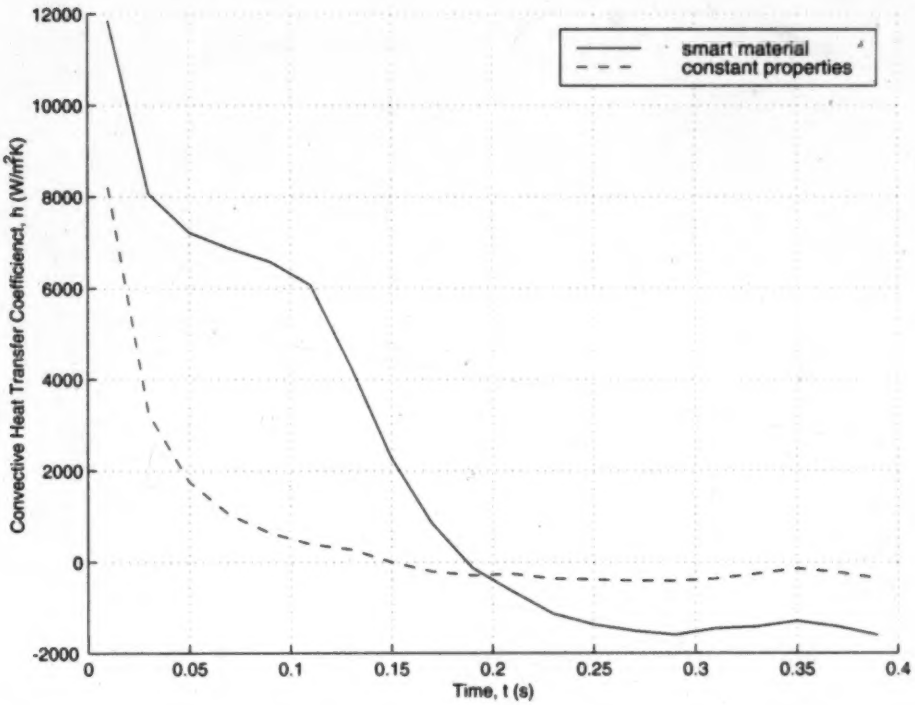

Figure 5.12: Cycle Averaged Surface Heat Transfer Coefficients

5.5.2 Comparison to One Dimensional Analysis

The results of the simulation for the temperature of the smart material may again be compared to a one dimensional analysis. In addition, it is possible to calculate the average phase of the smart material over the cross section using the one dimensional analysis.

The difficulty of selecting a suitable value for the convective heat transfer coefficient is encountered again. For the purpose of comparison three choices are used: the average, a value towards the low end of the range of h's calculated, and a value towards the high end of the range of h's calculated.

Figure 5.13 shows the average temperature time history for both the 1D and 2D analyses. Figure 5.14 shows the average smart material phase time history for the 1D and 2D analyses. The result is the same as the constant property test case, it is difficult to reproduce the average results of the 2D analysis using a 1D assumption. This is true for both the average temperature history and the average phase history.

For this test case the Biot number is closer to the limiting value of 0.1, as shown in Figure 5.15. However the results from the one dimensional analysis are still not comparable to the two dimensional averages. The difference is most likely due to the decaying with time of the average heat transfer coefficient in the two dimensional analysis. A single heat transfer coefficient cannot mimic the effects of a large initial heat transfer rate which then decreases over the course of the simulation.

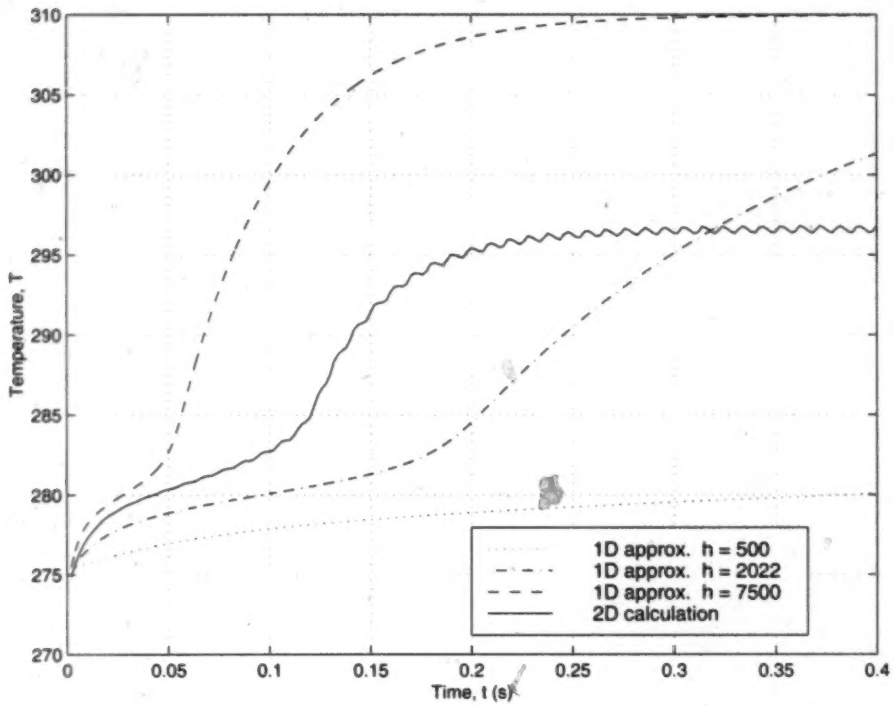

Figure 5.13: Comparison Between 1D and 2D Temperature History, Smart Material

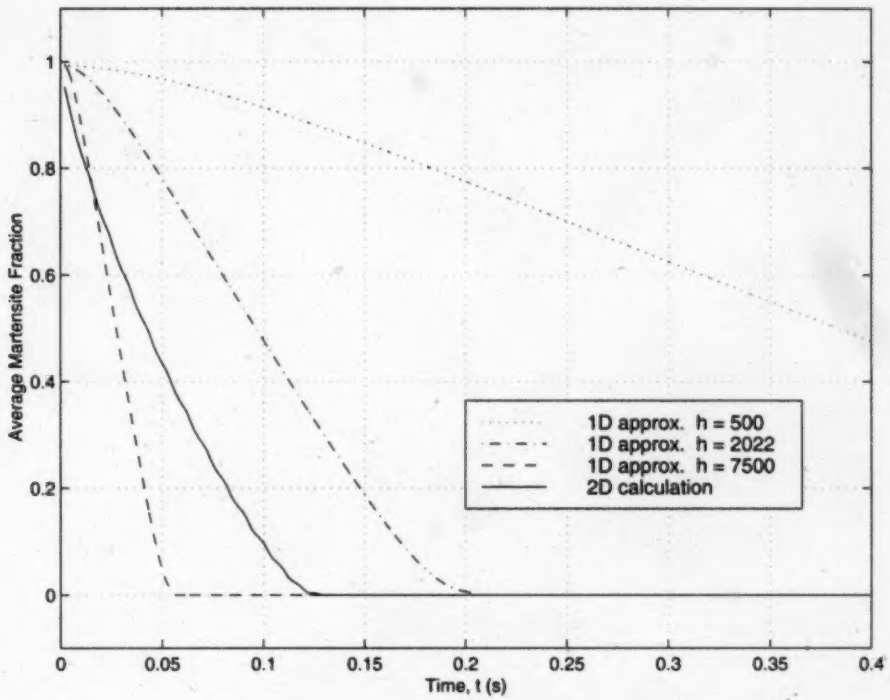

Figure 5.14: Comparison Between 1D and 2D Phase History

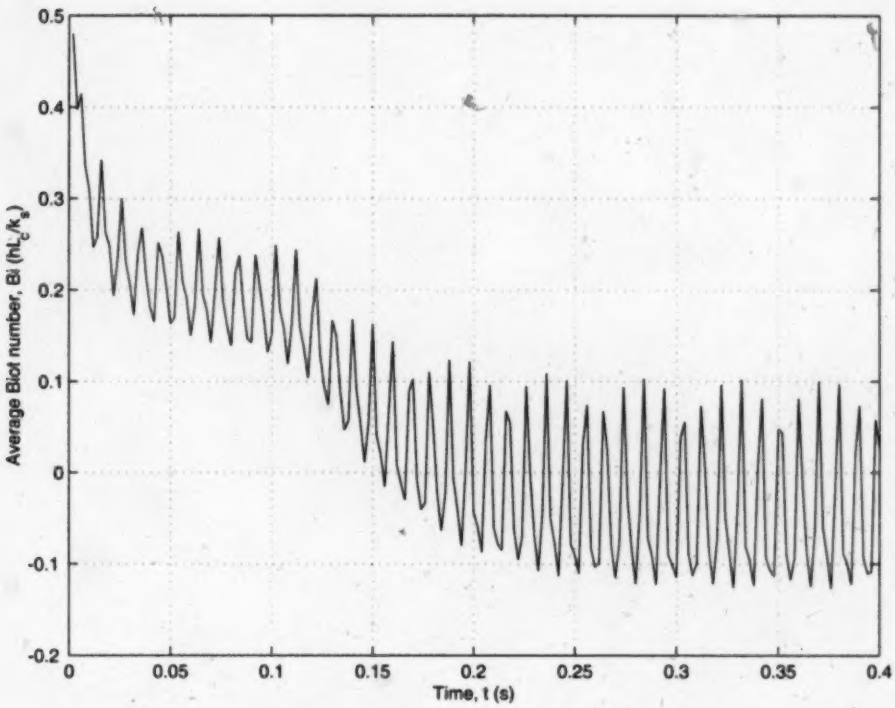

Figure 5.15: Time History of Biot Number for Smart Material

5.6 Comparison of Smart Materials with Different Material Properties

The selected example problem is an inferior vena cava filter comprised of a smart material. For this application there is a temperature difference of $37K$ between the initial temperature of the smart material and the eventual steady state temperature. This means there is a range of $37K$ in which the material may change phase from martensite to austenite. From the literature the temperature at which smart materials change phase is dependent upon the composition of the material [31]. Therefore this is a characteristic which designers have some control over.

Shown in Figure 5.16 is the average phase history for three smart materials with different phase transition temperatures. The austenite transformation start temperatures of these test cases are $275K$, $288K$ and $299K$. The corresponding transformation finish temperatures are $285K$, $298K$ and $309K$ respectively. It is apparent from Figure 5.16 that is is beneficial to have the transformation start temperature as far as possible from the external temperature which is driving the phase change.

The other material property of the smart material which affects the rate of phase change is the latent energy of transformation. This is the energy needed to complete the phase change from martensite to austenite, as well as the reverse. Shown in Figure 5.17 is the phase time history for two test cases both having the same transition temperatures, however one case has a latent energy of transformation which is one third the value of the other case. The test case having the smaller latent energy of transformation completes

the phase change to austenite quickest. This is also evident in the average temperature history for these two cases shown in Figure 5.18. The test case with the larger latent energy of transformation experiences a reduced rate of temperature increase due to the increased energy requirements of the phase change.

The influence of the transition temperatures and latent energy of transformation combine to effect the rate at which a smart material device will change phase. A combination of the two which leads to incomplete or slow phase change could result in improper actuation or failure of a device.

Consider Figures 5.19(a) - 5.19(e), a sequence of phase contour plots through one cycle of vortex shedding. These are for smart material 'A', which has a transformation start temperature of $288K$; the average phase time history is shown in Figure 5.16. This material is slowly changing phase and is experiencing a decreasing rate of transformation. As a result there is a region near the trailing edge of the ellipse which is oscillating through the middle region of the phase change. Given the suspect fatigue life of some smart materials [5], the situation illustrated in Figures 5.19(a) - 5.19(e) is one best avoided.

Alternatively, Figures 5.20(a) - 5.20(e) show the phase contours over a vortex shedding cycle for a more desirable outcome. This smart material, 'B', has a lower transition start temperature of $275K$ (further from the driving temperature). It also has a lower latent energy of transformation of $H = 0.0493J/mm^3$, compared to $H = 0.148J/mm^3$ for the previous case. The phase time history for this simulation is shown in Figure 5.17. This smart material transitions quickly through the phase change. No regions of the

ellipse are going through large oscillations in phase as a result of the vortex shedding influence.

Text resumes on page 126

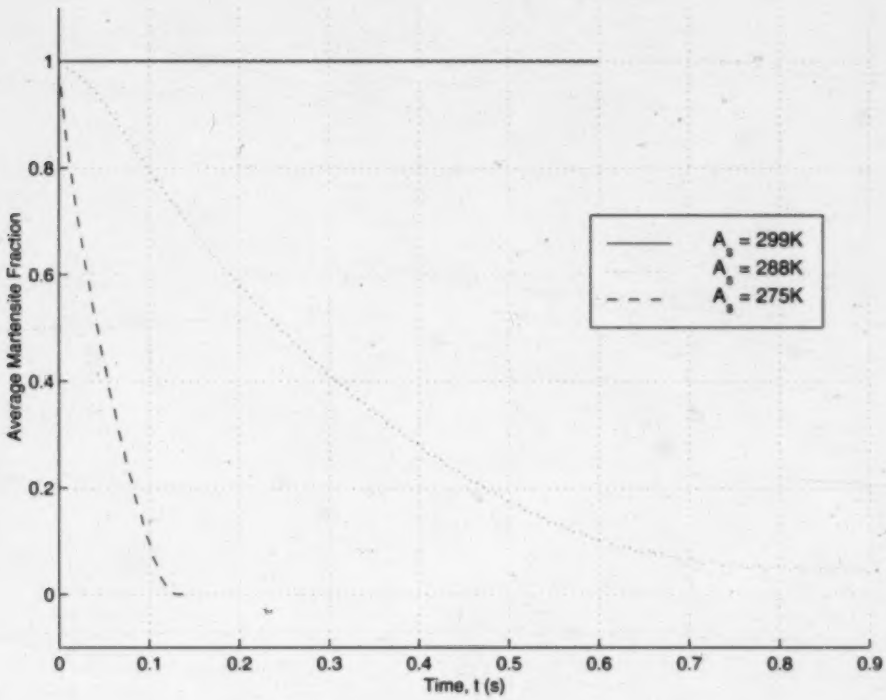

Figure 5.16: Phase History for Smart Materials with Different Transition Temperatures

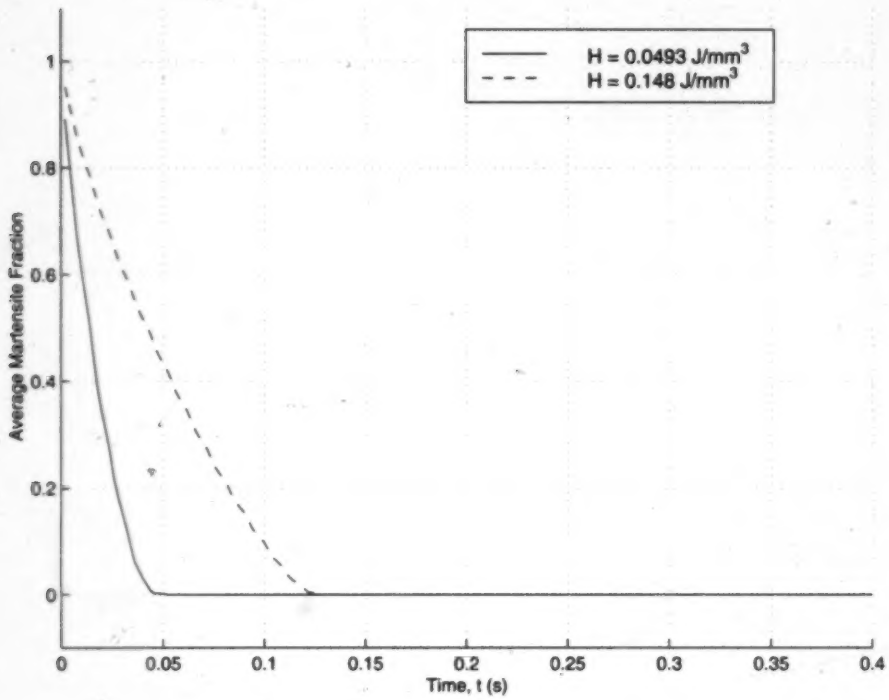

Figure 5.17: Phase History for Smart Materials with Different Latent Transformation Energy Amounts

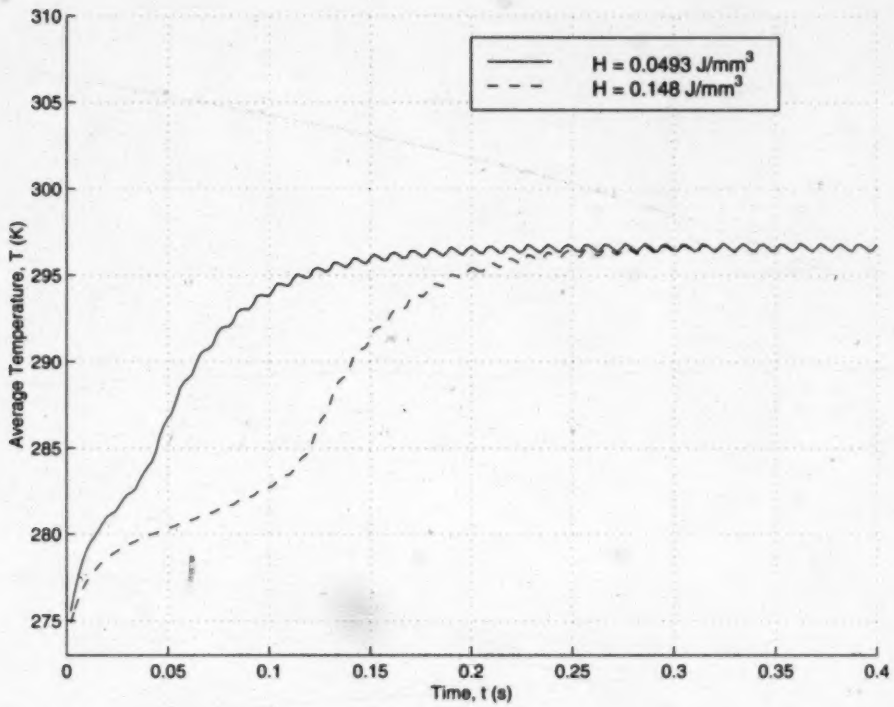

Figure 5.18: Temperature History for Smart Materials with Different Latent Transformation Energy Amounts

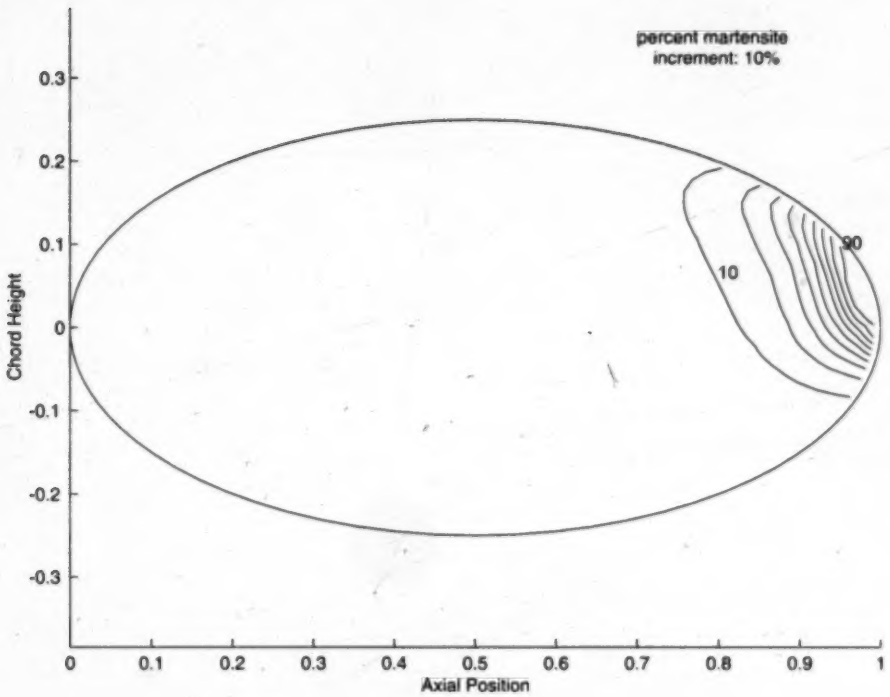

Figure 5.19(a): Phase Contours in Smart Material 'A' for one Period of Vortex Shedding, t = 0.800

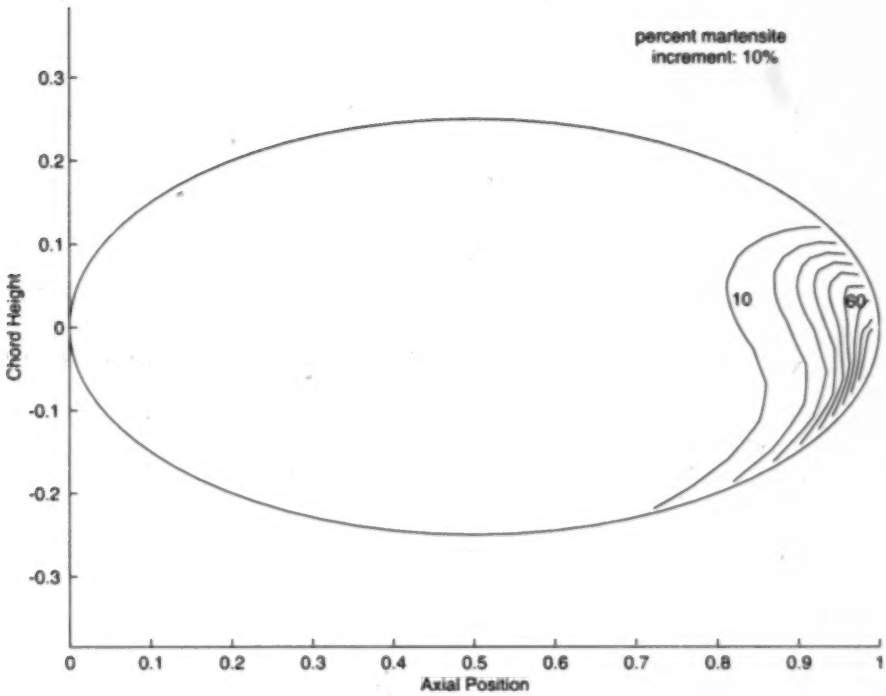

Figure 5.19(b): Phase Contours in Smart Material 'A' for one Period of Vortex Shedding, t = 0.804

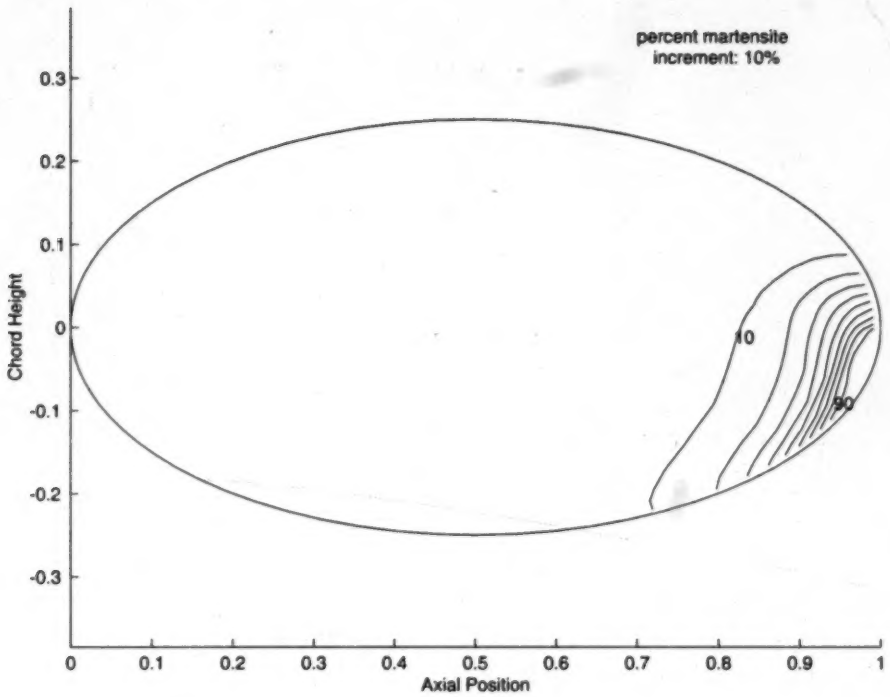

Figure 5.19(c): Phase Contours in Smart Material 'A' for one Period of Vortex Shedding, t = 0.808

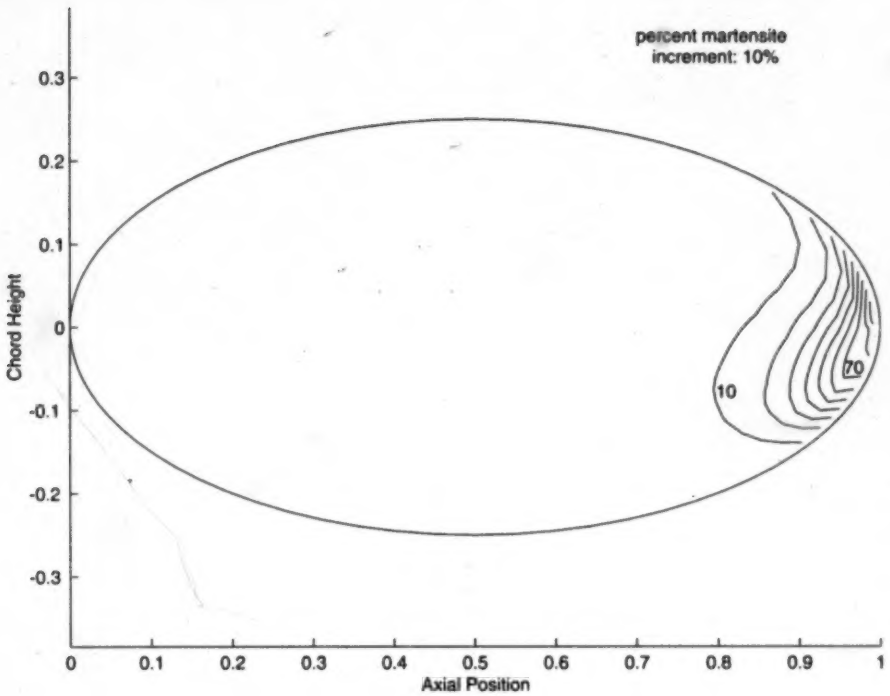

Figure 5.19(d): Phase Contours in Smart Material 'A' for one Period of Vortex Shedding, t = 0.812

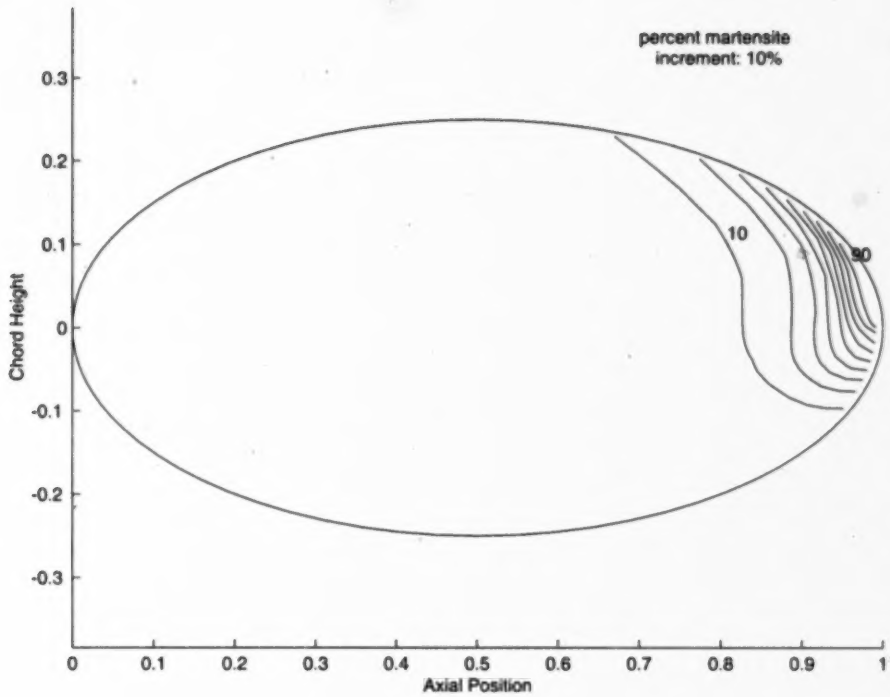

Figure 5.19(e): Phase Contours in Smart Material 'A' for one Period of Vortex Shedding, t = 0.816

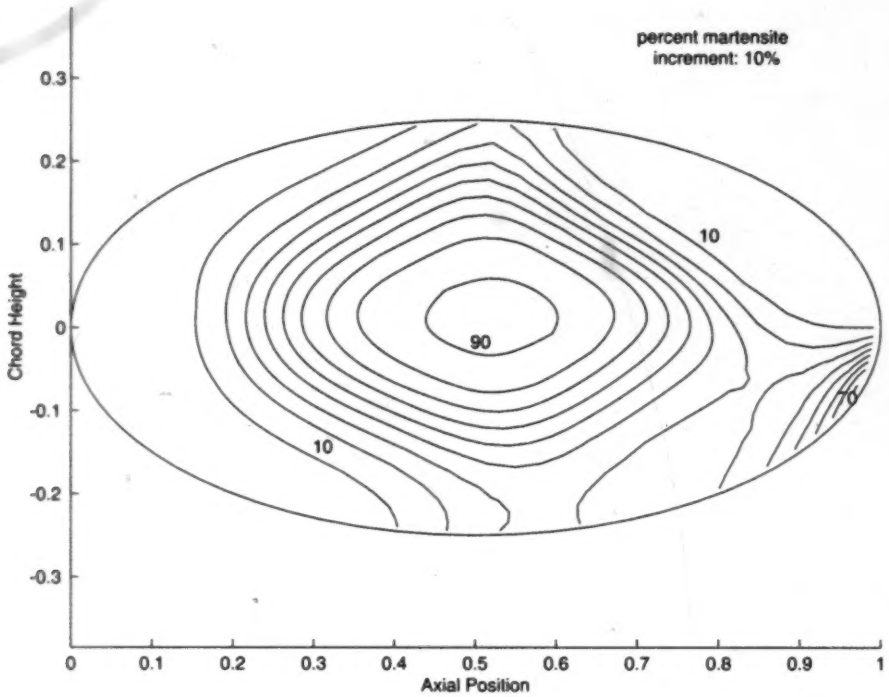

Figure 5.20(a): Phase Contours in Smart Material 'B' for one Period of Vortex Shedding, t = 0.020

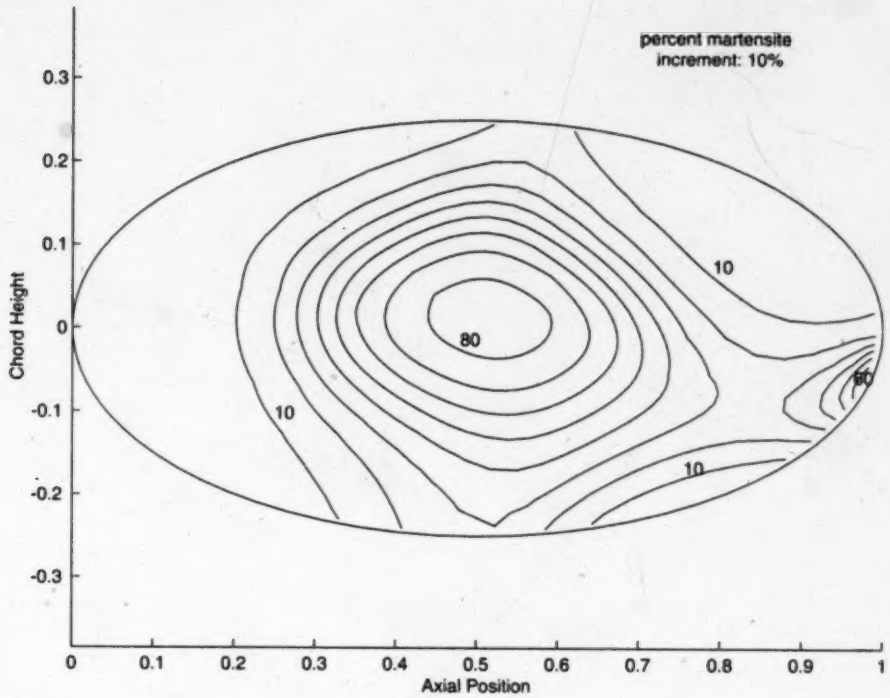

Figure 5.20(b): Phase Contours in Smart Material 'B' for one Period of Vortex Shedding, t = 0.024

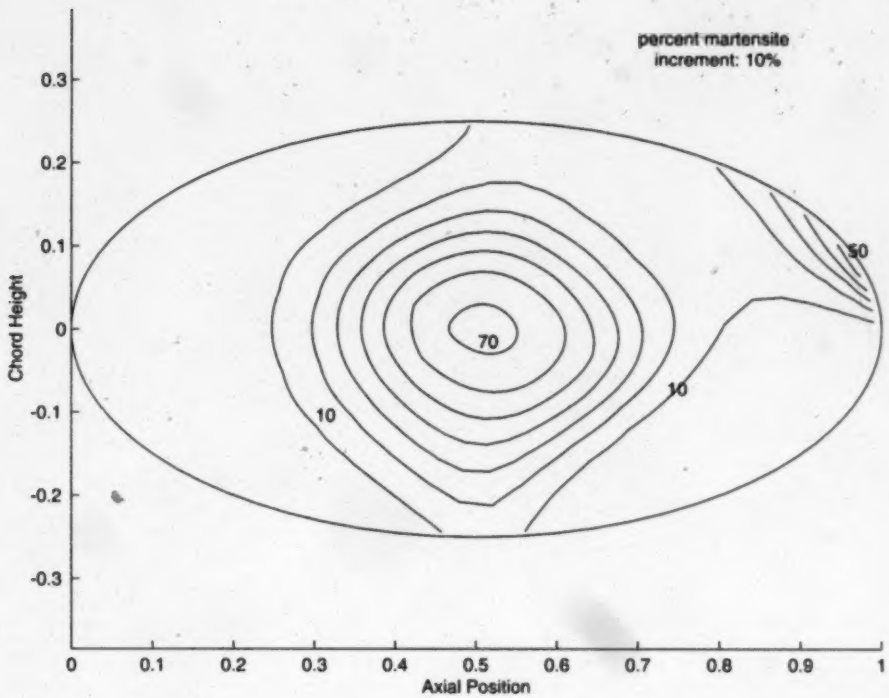

Figure 5.20(c): Phase Contours in Smart Material 'B' for one Period of Vortex Shedding, t = 0.028

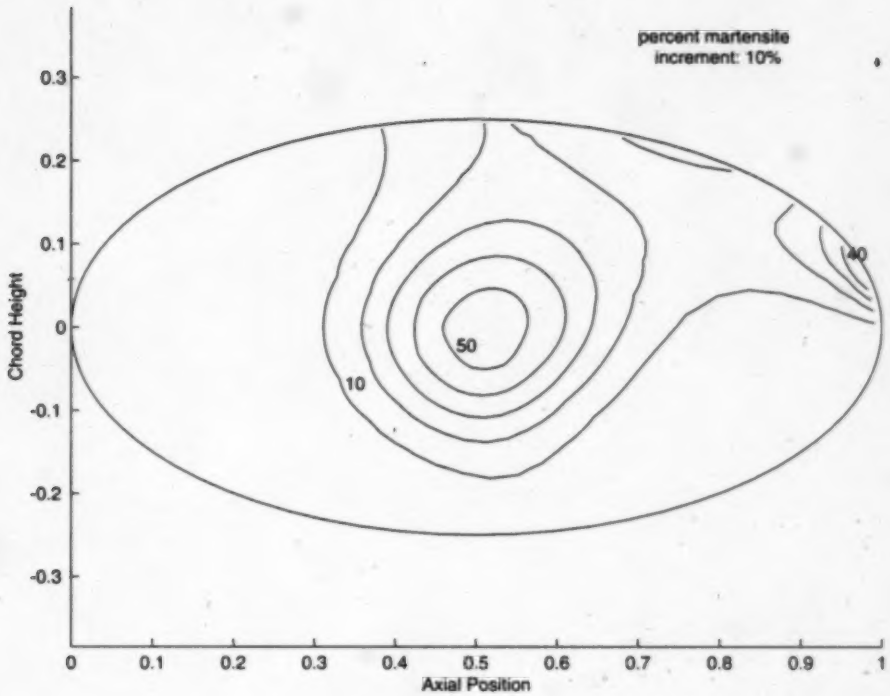

Figure 5.20(d): Phase Contours in Smart Material 'B' for one Period of Vortex Shedding, t = 0.032

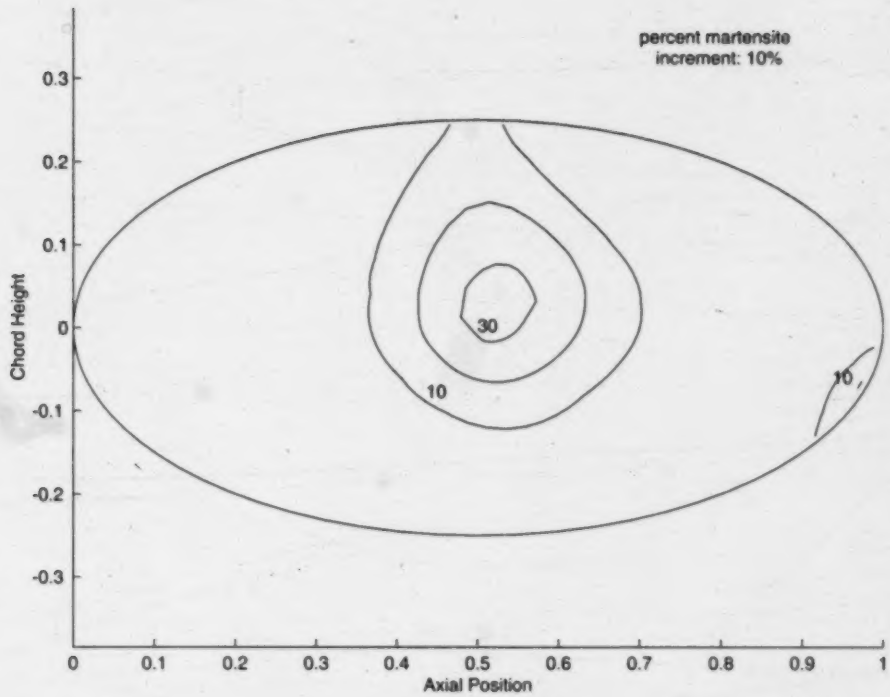

Figure 5.20(e): Phase Contours in Smart Material 'B' for one Period of Vortex Shedding, t = 0.036

CHAPTER 6

CONCLUSIONS

A numerical scheme has been developed to model the thermal interaction of a solid object with variable material properties in low Reynolds number crossflow. The variable material properties of the solid model the property changes of a smart material as it undergoes a solid state change in phase. The change in phase of the smart material occurs as a result of the temperature change of the material.

The temperature change which results in phase change can be facilitated by heat gain or loss through the surface of the material. A boundary condition has been developed to model the physics of the thermal boundary between the solid and a surrounding fluid. This boundary condition does not require a surface temperature or surface heat flux amount to be prescribed. Instead the heat flux between the fluid and solid is calculated based on the temperatures near the surface, and this is used as the boundary condition. This is beneficial since setting either a surface temperature or heat flux would govern the thermal interaction at the surface. The heat flux across the interface is an important component of this work as the phase change of

the material is dependent upon this convective heat gain.

The state of a smart material is expressed as a function of the temperature and stress, if any is present. An approximate function was fitted to the state function of the smart material to facilitate the solution of the material phase of the solid. The supplied state function has no analytical solution and so a numerical approximation was developed. Use of an approximate function decreased computation times through direction solution of the phase given a temperature value. Alternatives to an approximate function would have been either numerical integration or sorting tabulated values with interpolation.

Five test cases were presented to demonstrate the effects of varying material properties, different phase transformation start temperatures, and different latent energies of transformation.

The first conclusion to be drawn is regarding the effects of variable material properties during phase change on the temperature history of the smart material. This was illustrated by a comparison between a constant material property simulation and a smart material simulation. Differences between these two indicate that the variable material properties of the smart material have a substantial effect on the average temperature history of the solid. Therefore, when modeling the thermal behavior of a smart material, it is necessary to incorporate the changing material properties.

The second conclusion to be drawn is that the transition temperatures of the smart material have a noticeable effect on the rate of phase change of the material. This was illustrated by comparison of the phase history of three smart materials with different transition temperatures. The further the transition start temperature is from the external temperature driving the

phase change, the faster the phase change will occur.

Decreasing the latent energy of transformation was shown to be an additional method of accelerating the rate at which the phase change occurs. Two test cases with the same transition temperatures were compared, one test case had one third the latent energy of transformation of the other test case. The test case with the lower latent energy of transformation changed phase at a quicker rate.

The possibly detrimental effects of incorrectly chosen transition temperatures and latent energy of transformation were demonstrated with a worst case scenario. A test case was presented in which the smart material had a slow rate of phase change and required a substantial amount of time for the phase transition. A region of the solid was shown to undergo large changes in phase composition as a result of the vortex shedding influence of the fluid. In comparison, a test case was presented in which the material quickly changes phase and no large oscillations in phase composition occurred.

Two thermal test cases were compared with results from a one dimensional analysis. It was shown that a one dimensional assumption would result in poor estimations of the average temperature history in the solid. This was true for both the smart material and the constant property material. However it was demonstrated that the one dimensional analysis is not expected to give accurate results for this application. This is due to the large magnitudes of the Biot number calculated from the two dimensional analysis. In addition, the 1D analysis assumes constant heat transfer between the fluid and solid for all time. The time dependent nature of the heat transfer between the solid and fluid demonstrated in the 2D model is not incorporated in a

1D model. A one dimensional analysis applied to the problem studied in this work would result in an incorrect estimation of the transformation time of the smart material. In addition, the small scale effects of the vortex shedding in the two dimensional model are not present in the one dimensional model.

A possibility for future work would be to incorporate the shape change of the smart material during the phase change. The current work assumes constant geometry, however a useful change in shape during the phase change is the main benefit of smart materials. Variable geometry would require addition of a grid generator which could redevelop the numerical grid as the shape of the smart material changed with time. This would also affect the coordinate transformation as (x, y) become functions of time as well as the computational coordinates (ξ, η).

An additional consideration for future work is the incorporation of resistive heating of the smart material into the model. Resistive heating is the technique most commonly used to initiate the phase change of a smart material device. This would require addition of a heat source term to the energy equation in the solid, and possibly a model for variation of the electrical resistance with phase.

BIBLIOGRAPHY

[1] Amalraj, J., Bhattacharyya, A., Faulkner, M.G. "Finite Element Modeling of Phase Transformation in Shape Memory Alloy Wires with Variable Material Properties," *Smart Materials and Structures* (accepted), 1999.

[2] Banks, H.T., Ito, K., Wang, Y., "Computational Methods for Identification and Feedback Control in Structures with Piezoceramic Actuators and Sensors," *Journal of Intelligent Material Systems and Structures*, vol.4, pp.469-476, 1997.

[3] Barrett, R., Farokhi, S., "Subsonic Aerodynamics and Performance of a Smart Vortex Generator System," *Journal of Aircraft*, vol.33, no.2, pp.393-398, 1996.

[4] Bhattacharyya, A., Lagoudas, D.C., "A Stochastic Thermodynamic Model for the Gradual Thermal Transformation of SMA Polycrystals," *Journal of Smart Materials and Structures*, vol.6, pp.235-250, 1997.

[5] Birman, V., "Review of Mechanisms of Shape Memory Alloy Structures," *Applied Mechanics Reviews*, vol.50, no.11, pt.1, pp.629-645, 1997.

[6] Boyd, J.G., Lagoudas, D.C., "A Thermodynamical Constitutive Model for Shape Memory Materials. Part I. The Monolithic Shape Memory Alloy," *International Journal of Plasticity*, vol.12, no.6, pp.805-841, 1996.

[7] Buehler, W.J., Gilfrich, J.V., Wiley, R.C., "Effect of Low-Temperature Phase Changes on the Mechanical Properties of Alloys near Composition TiNi," *Journal of Applied Physics*, vol.34, no. 5, pp.1475-1477, 1963.

[8] Chandrasekhar, S. *Hydrodynamic and Hydromagnetic Stability*. Oxford University Press, London, 1961.

[9] Chang, K.S., Sa, J.Y., "The Effect of Buoyancy on Vortex Shedding in the Near Wake of a Circular Cylinder," *Journal of Fluid Mechanics*, vol.220, pp.253-266, 1990.

[10] Dorney, D.J., Davis, R.L., "Navier-Stokes Analysis of Turbine Blade Heat Transfer and Performance," *Journal of Turbomachinery, Transactions of the ASME*, vol.114, pp.795-806, 1992.

[11] Duerig, T.W., Stöckel, D., Keeley, A., "Actuator and Work Production Devices," *Engineering Aspects of Shape Memory Alloys*, Duerig, T.W., Melton, K.N., Stöckel, D., Wayman, C.M. (eds), Butterworth - Heinemann, London, England, 1990.

[12] Eckert, E.R.G., Soehngen, E. "Distribution of Heat-Transfer Coefficients Around Circular Cylinders in Crossflow at Reynolds Numbers From 20 to 500," *Transactions of the ASME*, vol.74, pp.343-347, 1952.

[13] Harten, A., Osher, S., "Uniformly Higher-Order Accurate Nonoscillatory Schemes I," *SIAM Journal of Numerical Analysis*, vol.24, pp.279-309, 1987.

[14] Hayes, J.L. "A Robust Numerical Method for Latent Heat Release During Phase Change," *ASME Heat Transfer Division*, vol.62, pp.63-69.

[15] Hirsch, C., *Numerical Computation of Internal and External Flows, Vol.1*. John Wiley & Sons, Chichester, Great Britain, 1988.

[16] Jain, P.C., Goel, B.S., "A Numerical Study of Unsteady Laminar Forced Convection From a Circular Cylinder," *Transactions of the ASME, Journal of Heat Transfer*, vol.98, pp.303-307, 1976.

[17] Karanth, D., Rankin, G.W., Sridhar, K., "A Finite Difference Calculation of Forced Convective Heat Transfer from an Oscillating Cylinder," *International Journal of Heat and Mass Transfer*, vol.37, no.11, pp.1619-1630, 1994.

[18] Khattacharyya, K., Kohn, R.V., "Symmetry, Texture and the Recoverable Strain of Shape-Memory Polycrystals," *Acta materialia*, vol.44, no.2, pp.529-542, 1996.

[19] Lagoudas, D.C., Bhattacharyya, A., "Modelling of Thin Layer Extensional Thermoelectric SMA Actuators," *International Journal of Solids and Structures*, vol.35, pp.331-362, 1997.

[20] Melton, K.N., "Ni-Ti Based Shape Memory Alloys," *Engineering Aspects of Shape Memory Alloys*, Duerig, T.W., Melton, K.N., Stöckel,

D., Wayman, C.M. (eds), Butterworth - Heinemann, London, England, 1990.

[21] Mohiaddin, R.H., Wann, S.L., Underwood, R., Firmin, D.N., Rees, S., Longmore, D.B., "Venal Caval Flow: Assessment with Cine MR Velocity Mapping," *Radiology*, vol.177, pp.537-541, 1990.

[22] Monreal, M., Ruiz, J., Olazabal, A., Arias, A., Roca, J., "Deep Venous Thrombosis and the Risk of Pulmonary Embolism," *Chest*, vol.102, no.3, pp.677-681, 1992.

[23] Nishimura, T., Kahamura, Y., "Numerical Errors of the Galerkin Finite-Element Method for Natural Convection of a Fluid Layer or a Fluid-Saturated Porous Layer," *Numerical Heat Transfer, Part A*, vol.22, pp.241-2515, 1992.

[24] Nguyen, H.D., Paik, S., Douglass, R.W., "Unsteady Mixed Convection about a Rotating Circular Cylinder with Small Fluctuations in the Free-Stream Velocity," *International Journal of Heat and Mass Transfer*, vol.39, no.3, pp.511-525, 1996.

[25] Panton, R. *Incompressible Flow*. John Wiley & Sons Inc, New York, New York, 1996.

[26] Perkins, J., Hodgson, D., "The Two-Way Shape Memory Effect," *Engineering Aspects of Shape Memory Alloys*, Duerig, T.W., Melton, K.N., Stöckel, D., Wayman, C.M. (eds), Butterworth - Heinemann, London, England, 1990.

[27] Purdy, G.R., Parr, J.G. "A Study of the Titanium-Nickel System Between Ti_2Ni and TiNi," *Transactions of the Metallurgical Society of AIME*, vol.22, pp.636-639, 1961.

[28] Schneider, G.E., LeDain, B.L. "Fully Developed Laminar Heat Transfer in Triangular Passages," *Journal of Energy*, vol.5, no.1, pp.15-21, 1981.

[29] Shahin, A.R., Meckl, P.H., Jones, J.D., "Enhanced Cooling of Shape Memory Alloy Wires Using Semiconductor "Heat Pump" Modules," *Journal of Intelligent Material Systems and Structures*, vol.5, pp.95-104, 1994.

[30] Shang, T., Epstein, A.H. "Analysis of Hot Streak Effects on Turbine Rotor Heat Load," *Journal of Turbomachinery, Transactions of the ASME*, vol.119, pp.544-553, 1997.

[31] Simon, M., Athanasoulis, C.A., Ducksoo, K., Steinberg, F.L., Porter, D.H., Byse, B.H., Kleshniski, S., Geller, S., Orron, D.E., Waltman, A.C., "Simon Nitinol Inferior Vena Cava Filter: Initial Clinical Experience," *Radiology*, vol.172, pp.99-103, 1977.

[32] Simon, M., Kaplow, R., Salzman, E., Freiman, D., "A Vena Cava Filter Using Thermal Memory Alloy," *Radiology*, vol.125, pp.89-94, 1977.

[33] Simon, M., Rabkin, D.J., Kleshiniski, S., Kim, D., Ransil,B.J., "Comparative Evaluation of Clinically Available Inferior Vena Cava Filters with an in Vitro Physiologically Simulation of the Vena Cava," *Radiology*, vol.189, pp.769-774, 1993.

[34] Stewart, J. *Calculus*. Brooks/Cole Publishing Company, Pacific Grove, California, 1991.

[35] Thompson J.F., Warsi, Z.U.A, Mastin, C.W., *Numerical Grid Generation, Foundations and Applications*. Elsevier Science Publishing Co. Inc., New York, New York, 1985.

[36] van Leer, B. "Towards the Ultimate Conservative Difference Scheme II, Monoticity and Conservation Combined in a Second Order Scheme," *Journal of Computational Physics*, vol.14, pp.361-370, 1974.

[37] Victor, S.A., Shah, V.L. "Steady State Heat Transfer to Blood Flowing in the Entrance Region of a Tube," *International Journal of Heat and Mass Transfer*, vol.19, pp.777-783, 1975.

[38] Wang, F.E., Buehler, W.J., Pickart, S.J., "Crystal Structure and a Unique "Martensitic" Transition of TiNi," *Journal of Applied Physics*, vol.36, no.19, pp.3232-3239, 1965.

[39] Wang, P., Kahawita, R., Nguyen, T.H., "Numerical Computation of the Natural Convection Flow About a Horizontal Cylinder using Splines," *Numerical Heat Transfer, Part A*, vol.17, pp.191-215, 1990.

[40] Wayman, C.M., Duerig, T.W., "An Introduction to Martensite and Shape Memory," *Engineering Aspects of Shape Memory Alloys*, Duerig, T.W., Melton, K.N., Stöckel, D., Wayman, C.M. (eds), Butterworth - Heinemann, London, England, 1990.

[41] Yokota, J.W. "An L-U Implicit Multigrid Algorithm to Solve the Euler Equations for Transonic Flow in Rotating Turbomachinery Passages," Ph.D. Thesis, Cornell University, 1987.

[42] Yokota, J.W. "Vorticity Dynamics of Inviscid Shear Layers," *AIAA Journal*, vol.31, no.8, pp.1430-1439, 1993.

[43] Yokota, J.W. "Unsteady Blade-Row Vortex Interaction," *Canadian Aeronautics and Space Journal*, vol.44, no.1, pp.25-32, 1998.

[44] Yokota, J.W. "A Kinematic Velocity Decomposition of Stratified Flow," *International Journal of Computational Fluid Dynamics*, vol.9, pp.122-135, 1998.

[45] http://smart.tamu.edu, *Sept.24, 1999*

[46] http://www.nitinolmed.com, *Sept.24, 1999*